Multiscale Analysis

of Reinforced Concrete Structures

Arturo Moyeda Morales

Submitted in partial fulfillment of the

requirements for the degree of

Doctor of Engineering Science

in the Fu Foundation

School of Engineering and Applied Science

Columbia University

2018

This page intentionally left blank.

This page intentionally left blank.

Abstract

Multiscale Analysis of Reinforced Concrete Structures

Arturo Moyeda Morales

A multiscale approach, coined as the High Order Computational Continua (HC^2), has been developed for efficient and accurate analysis and design of reinforced concrete structures. Unlike existing homogenization-like methods, the proposed multiscale approach is capable of handling large representative volume elements (RVE), i.e., the classical assumption of infinitesimally is no longer required, while possessing accuracy of direct numerical simulation (DNS) and the computational efficiency of classical homogenization methods.

The multiscale beam and plate elements formulated using the proposed HC^2 methodology can be easily incorporated into the existing reinforced concrete design practices. The salient features of the proposed formulation are: (i) the ability to consider large representative volume elements (RVE) characteristic to nonsolid beams,waffle and hollowcore slabs, (ii) versatility stemming from the ease of handling damage, prestressing, creep and shrinkage, and (iii) computational efficiency resulting from model reduction, combined with the damage law rescaling methods that yield simulation results nearly mesh-size independent.

The multiscale formulation has been validated against experimental data for rectangular beams, I beams, pretensioned beams, continuous posttension beams, solid slabs, prestressed hollowcore slabs and waffle slabs.

Contents

i

This page intentionally left blank.

List of Tables

This page intentionally left blank.

List of Figures

This page intentionally left blank.

Acknowledgements

I would like to extend my deepest gratitude to my advisor Prof. Jacob Fish, for taking a chance on me, an unconventional student who knocked on his door, and gave me the privileged opportunity to work with him. The knowledge he shared was invaluable to my research, but it has proven more valuable in my everyday life. I thank him for his patience, advice, guidance, but most of all for his friendship. Thank you Professor Fish, for being a true mentor.

I am grateful to my dissertation defense committee Professor Raimondo Betti, Professor I. Cevdet Noyan, Professor Haim Waisman and Dr. Badri Hiriyur for their time served on my committee; your comments and reviews were greatly appreciated.

My sincere gratitude to the Department of Civil Engineering and Engineering Mechanics at Columbia University, especially Prof. George Deodatis for his advice, and Scott Kelly for all his help during this eight year journey. To my friends David Tal, Zifeng Yuan, Yang Jiao, and Dimitrios Fafalis, although I was not at school every day, you were always there when I needed help.

To my wife Mónica, for your unconditional love…

To my children Arturo and Federico, may you always pursue your dreams…

This page intentionally left blank.

Chapter 1

Introduction

With an annual production of more than 23 billion tons of concrete - the most used material in construction worldwide [1] - efficient design of reinforced concrete structures is of the utmost importance to the society. Since environmental impact of concrete is considerable due to CO_2 emissions, water consumption, impact on the landscape for aggregate mining, just to name a few, analysis and design of concrete structures should be more reliable and better optimized.

Since the early 1900's, there have been considerable research efforts aimed at developing theories and methods to predict its behavior. The first code published in North America with specific recommendations for the analysis and design of reinforced concrete was published in 1910 by the American Concrete Institute (ACI), which now publishes the Building Code Requirements for Structural Concrete with its latest edition published in 2014 [2].

Practitioners have long realized that stiffness and strength of concrete structures must reflect among other things cracking, plasticity, creep and shrinkage; this has been done in the form

of semi empirical reduction factors and recommendations that are still used in codes today [2, 3].

Concrete frame-type structures have been analyzed for decades using beam-column elements along with code guidelines. Emery et al. [4], described the current state-of-the-practice and why engineering community should move towards more rigorous analysis and simulation approaches for reinforced concrete structures. Research efforts aimed at detailed numerical analysis of concrete structures span more than 40 years. From computational point of view, these efforts can be divided into two main categories:

a) Two-dimensional (2D) and three-dimensional (3D) finite element analysis using continuum elements with constitutive models, such as damage, plasticity, and a combination of the two or more specialized models, such as the microplane model [5] or lattice model [6]; and

b) Fiber beam-column elements [7] that discretize the cross-section into fibers in combination with uniaxial material models and more recently 3D material models [8].

Development of material models for three-dimensional analysis of concrete span more than half a century. Willam and Warnke [9] developed an elaborate plasticity model where elastic-

perfectly plastic behavior is assumed in compression while in tension, an elastic perfectly brittle behavior with softening plasticity branch is assumed. An excellent review of continuum damage models for concrete including isotropic and anisotropic models and their utilization in practice was given by Mazars and Pijaudier-Cabot [10]. A hybrid plasticity-damage model for cyclic loading of concrete structures proposed by Lee and Fenves [11] was adopted in various commercial codes and is widely used in practice. Material models developed in recent years, employ a combination of damage mechanics and plasticity, such as CDMP2 developed by Grassl et al. [12], the hybrid fracture-plasticity model proposed by Cervenka and Cervenka [13] and a recently developed triaxial constitutive model for concrete under cyclic loading by Moharrami and Koutromanos [14].

In the previous century (prior to year 2000) the literature on multiscale methods for the analysis of concrete has been rather limited, but interest in multiscale methods accelerated over the past two decades as can be seen from Figure 1. Maekawa et al. [15] presented a multiscale approach for the life-span simulation of concrete subjected to hydration, carbonation, corrosion and damage. Oliver et al. [16] developed a multiscale approach for concrete-like structures, but its utilization in practice has been very limited due to significant computational cost involved. This is because a direct computational homogenization employed requires repeated solution of sizeable unit cell (UC) or representative volume element (RVE) problems for nonlinear applications. Caballero et al. [17] considered multiscale analysis at the scale of the aggregate and the cement paste.

Zhang et al. [18] explicitly modeled at the scale of fibers and concrete to predict elastic properties and strength of the fiber-reinforced concrete. Meschke and Rumanus [19] employed Mori-Tanaka approach [20] to analyze reinforced concrete shell structures where the RVE consisted of the concrete matrix and the reinforcing steel in two directions. Wu et al. [21] presented a two-phase multiscale approach for the analysis of plain concrete using reduced order homogenization. For details on various micromechanical approaches see [22].
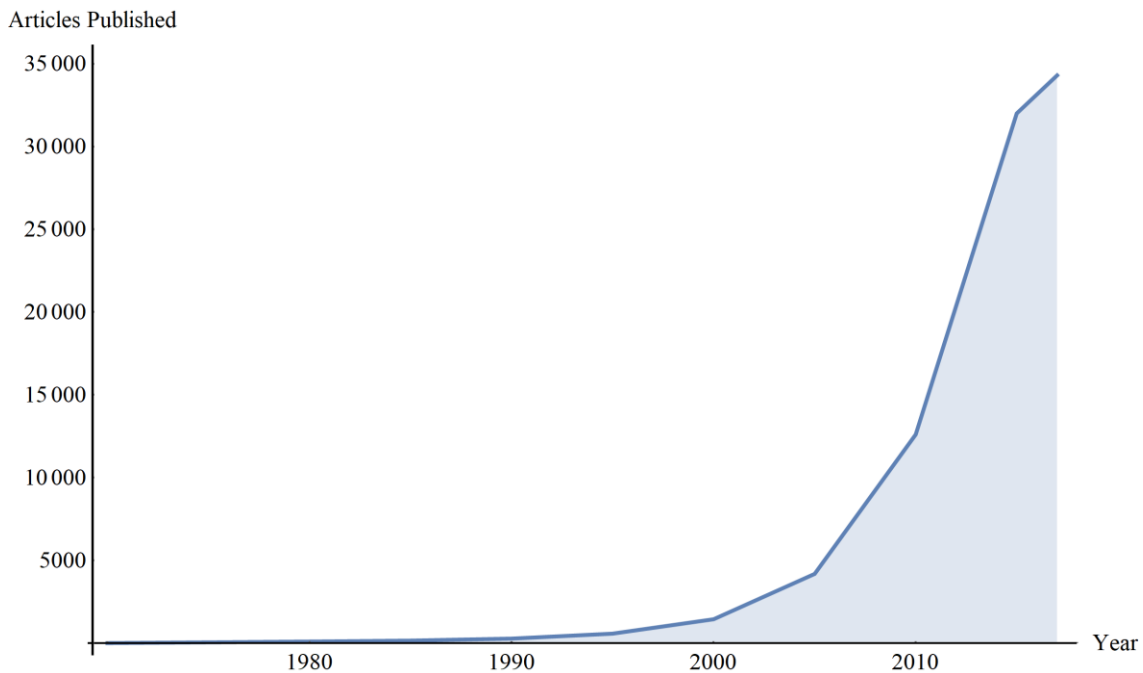
Fig. 1. Number of articles published with the phrase "Multiscale Concrete" in the text per Google Scholar (2018).

In large scale applications, modelling each beam, column or slab with multiple continuum elements is computationally not feasible. Furthermore, resolving three-dimensional

4

microstructural features of reinforced concrete for nonlinear problems where a discretized RVE problem has to be repeatedly solved is not computationally feasible either. Thus the primary goal of the multiscale framework developed in this thesis is to address the two aforementioned issues that preclude effective utilization of multiscale technologies in reinforced concrete structures. This will be accomplished by the following three main contributions:

1. Development of a multiscale approach for structural (beam/column) elements with considerable material-structural scale mixing. The main challenge here is that unlike in the classical homogenization framework, in concrete beams the size of RVE is finite, and consequently, the coarse-scale (macroscopic) fields may no longer be uniform within the RVE domain. Typically, the RVE in reinforced concrete beams or columns extends the entire depth and width of the beam/column cross-section. Furthermore, in the case of short beams or considerable refinement in the axial beam direction, the unit cell size even in the axial direction may "see" considerable macroscopic gradients, and thus introducing so-called scale coupling phenomenon. This scale coupling between the material scale and the structural elements will be addressed using the higher order computational continua formulation (HC^2), an extension of the computational continua framework [23].

2. Development of the multiscale plate element for the analysis of solid, waffle and hollowcore reinforced concrete slabs based on the higher order computational continua

5

(HC^2) formulation. The salient features of the proposed formulation are: (i) the ability to consider large representative volume elements (RVE) characteristic to waffle and hollowcore slabs, (ii) versatility due to ease of handling damage, prestressing, creep and shrinkage, and (iii) computational efficiency resulting from model reduction, combined with classical damage law rescaling methods that yield simulation results nearly mesh-size independent.

3. Development of a customized reduced order homogenization (ROH) for structural elements. The reduced order homogenization [24-30] is aimed at reducing the computational cost of solving complex inelastic RVE problems by constructing deformation modes which a priori satisfy equilibrium equations within RVE.

Chapter 2

The High Order Computational Continua (HC²)

2.1 Governing Equations

Consider a heterogeneous body of reinforced concrete formed by either periodic repetition of steel reinforcement or periodic concrete structure or both in an open, bounded *composite domain* $\Omega^\zeta \subset \mathbb{R}^3$. The representative volume element (RVE) denoted by $\Theta \subset \mathbb{R}^3$ is assumed to be finite, i.e. unlike in the homogenization theory it is not insignificant compared to the coarse-scale domain features.

The following governing equations in the indicial notation on the composite $\mathbf{x} \in \Omega^\zeta$ are stated at the fine-scale of interest:

$$\sigma_{ij,j}^\zeta(\mathbf{x}) + b_i^\zeta(\mathbf{x}) = 0 \ \text{on} \ \Omega^\zeta \tag{1}$$

$$\sigma_{ij}^{\zeta}(\mathbf{x}) = L_{ijkl}^{\zeta}(\mathbf{x})\left(\varepsilon_{kl}^{\zeta}(\mathbf{x}) - \mu_{kl}^{\zeta}(\mathbf{x})\right) \text{ on } \Omega^{\zeta} \tag{2}$$

$$\varepsilon_{ij}^{\zeta}(\mathbf{x}) = u_{(i,j)}^{\zeta}(\mathbf{x}) \equiv \frac{1}{2}\left(u_{i,j}^{\zeta} + u_{j,i}^{\zeta}\right) \text{ on } \Omega^{\zeta} \tag{3}$$

$$u_i^{\zeta}(\mathbf{x}) = \bar{u}_i^{\zeta}(\mathbf{x}) \text{ on } \partial\Omega^{u\zeta} \tag{4}$$

$$\sigma_{ij}^{\zeta}(\mathbf{x})n_j^{\zeta}(\mathbf{x}) = \bar{t}_i^{\zeta}(\mathbf{x}) \text{ on } \partial\Omega^{t\zeta} \tag{5}$$

where the superscript ζ denotes existence of fine-scale features, $\boldsymbol{\sigma}^{\zeta}$ is the Cauchy stress, $\boldsymbol{b}^{\zeta}$ the body force, $\boldsymbol{L}^{\zeta}$ is the fourth order material tensor; $\boldsymbol{u}^{\zeta}$ denotes the displacements with $\bar{\boldsymbol{u}}^{\zeta}$ being prescribed displacements on the essential boundary $\partial\Omega^{u\zeta}$; $\bar{\boldsymbol{t}}^{\zeta}$ is the traction acting on the natural boundary $\partial\Omega^{t\zeta}$. The essential and natural boundary conditions satisfy $\partial\Omega^{\zeta} = \partial\Omega^{u\zeta} \bigcup \partial\Omega^{t\zeta}$ and $\partial\Omega^{u\zeta} \bigcap \partial\Omega^{t\zeta} = \varnothing$; $\boldsymbol{\varepsilon}^{\zeta}$ is the total strain, $\boldsymbol{\mu}^{\zeta}$ the total eigenstrain that can be additively decomposed into mechanical $_{mech}\boldsymbol{\mu}$ and initial $_0\boldsymbol{\mu}$ eigenstrains, the latter describing the initial effects of prestressing, creep, shrinkage and/or temperature, such that $\boldsymbol{\mu}^{\zeta} = {}_{mech}\boldsymbol{\mu} + {}_0\boldsymbol{\mu}$. The term eigenstrain is used for all inelastic strains such as plastic, damage, creep, shrinkage, thermal or initial strains. Einstein summation convention is employed throughout the manuscript and the use of commas denotes the spatial derivatives with parenthesis around the subscripts denoting symmetric derivative. Bold letters are reserved for tensors (italic) and matrices (non-italic).

2.2 Non-local Quadrature

To construct a weak form of (1)-(5) (with the test function space $\mathcal{W}^\zeta$ to be later defined) it

is necessary to compute integrals over the composite domain Ω^ζ

$$\int_{\Omega^\zeta} \underbrace{w_i^\zeta \left(\sigma_{ij,j}^\zeta + b_i^\zeta \right) d\Omega}_{\Psi^\zeta} = 0 \quad \forall \mathbf{w}^\zeta \in \mathcal{W}^\zeta \tag{6}$$

In the classical homogenization theory, multiple scales (and coordinates) are introduced

$\Psi^\zeta = \Psi(\mathbf{x}, \mathbf{y})$ where $\mathbf{x} \in \Omega$ is the coarse-scale coordinate and $\mathbf{y} \in \Theta$ the RVE coordinate.

Furthermore, due to the assumption of the infinitesimality of the RVE ($\zeta \to 0$), the

integration in the composite domain (6) can be computed as a sum of integrals over

infinitesimal RVE domains

$$\lim_{\zeta \to 0^+} \int_{\Omega^\zeta} \Psi^\zeta \, d\Omega = \lim_{\zeta \to 0^+} \int_\Omega \left(\frac{1}{|\Theta|} \int_\Theta \Psi(\mathbf{x}, \mathbf{y}) d\Theta \right) d\Omega \tag{7}$$

The computational continua formulation considers the case where the RVE is finite and

possibly comparable to the coarse-scale domain features. By this approach [23,24,25,31], the

9

integration over the composite domain Ω^ς is replaced by the integration over the so-called

computational continua domain Ω^C, consisting of a *disjoint union* (sometimes called the

direct sum or free union) of *computational RVE* (or simply RVE, hereafter) domains $\Theta_{\hat{x}_I}$

denoted as

$$\Omega^C = \coprod_{I=1}^{\hat{N}} \Theta_{\hat{X}_I} \tag{8}$$

where $\hat{X}_I$ denotes the position of the so-called nonlocal quadrature point and $\hat{N}$ the number

of integration points. The nonlocal quadrature scheme for a function Ψ^ς over the composite

domain is defined as

$$\int_{\Omega^\varsigma} \Psi^\varsigma d\Omega = \sum_{I=1}^{\hat{N}} W_I J_I \frac{1}{\left|\Theta_{\hat{x}_I}\right|} \int_{\Theta_{\hat{x}_I}} \Psi^\varsigma(\hat{X}_I, \chi) d\Theta \tag{9}$$

where W_I denotes the nonlocal quadrature weight; $\left|\Theta_{\hat{x}_I}\right|$ the volume of the RVE domain $\Theta_{\hat{x}_I}$

; J_I the Jacobian computed at the RVE centroid mapping the coarse-scale element into a bi-

unit cube (square, interval); χ the local Cartesian coordinate system with an origin placed

at the RVE centroid. W_I and $\hat{X}_I$ are chosen to exactly evaluate integrals (9) on the composite

10

domain with integrand Ψ^ζ approximated by a polynomial of the order *m*. The pair $(W_I, \hat{X}_I)$ depends on the RVE size relative to the coarse-scale finite element size. For the cuboidal element shapes [23,24,25,31] the nonlocal quadrature is obtained by a tensor product of one-dimensional nonlocal quadrature. For instance, the two-point nonlocal quadrature rule is defined by

$$\hat{X}_{1,2} = \pm\sqrt{\frac{1}{3} - \frac{\Theta'^2}{12}} \; ; \quad W_{1,2} = 1 \tag{10}$$

For recent work on computational continua for non-cuboidal element shapes see [32].

2.3 The RVE Problem.

Following the variational multiscale method [33] and the s-version of the finite element method [34], the strains are decomposed into a coarse-scale solution and a fine-scale perturbation as follows:

$$\varepsilon_{ij}^\zeta(\hat{\boldsymbol{X}}_I, \boldsymbol{\chi}) = \varepsilon_{ij}^c(\hat{\boldsymbol{X}}_I, \boldsymbol{\chi}) + \varepsilon_{ij}^1(\hat{\boldsymbol{X}}_I, \boldsymbol{\chi}) \tag{11}$$

11

where the superscripts c and 1 denote the coarse-scale solution and fine-scale perturbation, respectively, with the fine-scale perturbation ε_{ij}^1 given by :

$$\varepsilon_{kl}^1(\hat{X}_I,\chi) = H_{(k,l)}^{mn}(\chi)\varepsilon_{mn}^c(\hat{X}_I,\chi) + \int_\Theta \tilde{h}_{(k,l)}^{mn}(\chi)\mu_{mn}^\zeta(\hat{X}_I,\chi)d\tilde{\Theta} \qquad (12)$$

where the interface discontinuity has been ignored for simplicity. In (12), H and $\tilde{h}$ are the influence functions for the coarse-scale strain and the fine-scale eigenstrain, respectively. The influence functions are computed from the reduced order equilibrium equations as described below.

The resulting fine-scale strain ε_{kl}^ζ and stress σ_{ij}^ζ are given by

$$\varepsilon_{kl}^\zeta = \left(I_{klmn} + H_{(k,l)}^{mn}(\chi)\right)\varepsilon_{mn}^c(\hat{X}_I,\chi) + \int_\Theta \tilde{h}_{(k,l)}^{mn}(\chi)\mu_{mn}^\zeta(\hat{X}_I,\chi)d\tilde{\Theta} \qquad (13)$$

$$\sigma_{ij}^\zeta = L_{ijkl}^\zeta(\chi)\left(\left(I_{klmn} + H_{(k,l)}^{mn}(\chi)\right)\varepsilon_{mn}^c(\hat{X}_I,\chi) + \int_\Theta \tilde{h}_{(k,l)}^{mn}(\chi)\mu_{mn}^\zeta(\hat{X}_I,\chi)d\tilde{\Theta} - \mu_{kl}^\zeta(\hat{X}_I,\chi)\right)$$

$$(14)$$

Model reduction necessary for computational efficiency is accomplished by a piece-wise constant discretization of eigenstrains over RVE partitions. Figure 2 depicts the RVE for a reinforced concrete beams where colors show different partitions in concrete and reinforcement over which the eigenstrains are assumed to be constant. For computational efficiency, steel reinforcements may be modeled as one-dimensional bar elements. The piece-wise constant discretization of eigenstrains in $\tilde{M}$ (concrete and steel) partitions is given by

$$\mu_{ij}^{\zeta}(\hat{X}_I, \chi) = \sum_{\Phi=1}^{\tilde{M}} \tilde{N}^{(\Phi)}(\chi)\mu_{ij}^{(\Phi)}(\hat{X}_I) \tag{15}$$

where

$$\tilde{N}^{(\Phi)}(\chi) = \begin{cases} 1 & \chi \in \Theta^{(\Phi)} \\ 0 & \chi \notin \Theta^{(\Phi)} \end{cases} \tag{16}$$
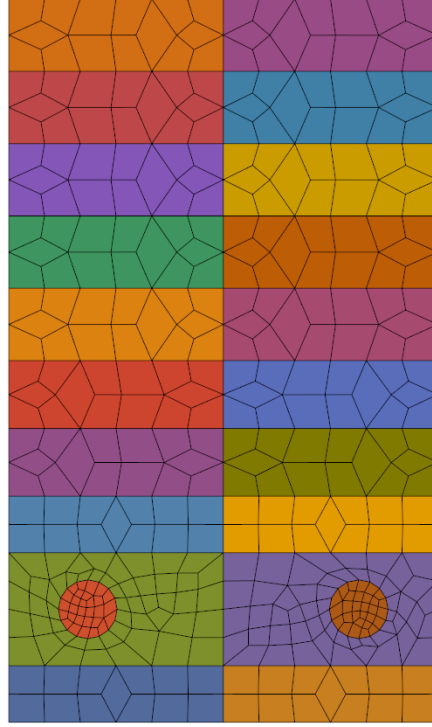
Fig. 2. Piecewise constant discretization of eigenstrains in a two-dimensional RVE. Colors denote various partitions over which eigenstrains are assumed to be constant.

Inserting the eigenstrain discretization (15) into (13) and (14) yields an approximation of fine-scale strains and stresses stress

$$\varepsilon_{kl}^{\zeta}(\hat{\boldsymbol{X}}_I, \boldsymbol{\chi}) = E_{klmn}(\boldsymbol{\chi})\varepsilon_{mn}^c(\hat{\boldsymbol{X}}_I, \boldsymbol{\chi}) + \sum_{\Phi=1}^{\tilde{M}} P_{kl}^{mn(\Phi)}(\boldsymbol{\chi})\mu_{mn}^{(\Phi)}(\hat{\boldsymbol{X}}_I) \qquad (17)$$

$$\sigma_{ij}^{\zeta}(\hat{\boldsymbol{X}}_I, \boldsymbol{\chi}) = \Sigma_{ijmn}(\boldsymbol{\chi})\varepsilon_{mn}^c(\hat{\boldsymbol{X}}_I, \boldsymbol{\chi}) + \sum_{\Phi=1}^{\tilde{M}} \Lambda_{ij}^{mn(\Phi)}(\boldsymbol{\chi})\mu_{mn}^{(\Phi)}(\hat{\boldsymbol{X}}_I) \qquad (18)$$

14

where

$$\Lambda_{ij}^{mn(\Phi)}(\chi) = L_{ijkl}^{\zeta}(\chi)\left(P_{kl}^{mn(\Phi)}(\chi) - I_{klmn}^{(\Phi)}\right) \tag{19}$$

$$P_{kl}^{mn(\Phi)} \equiv h_{(k,l)}^{mn(\Phi)} \tag{20}$$

$$E_{klmn}(\chi) = I_{klmn} + H_{(k,l)}^{mn}(\chi) \tag{21}$$

$$\Sigma_{ijmn}(\chi) = L_{ijkl}^{\zeta}(\chi)E_{klmn}(\chi) \tag{22}$$

Since the RVE equilibrium equation, $\sigma_{ij,j}^{\zeta} = 0$, should hold for arbitrary values of $\varepsilon_{mn}^{c}, \nabla\varepsilon_{mn}^{c}$

and $\mu_{mn}^{(\Phi)}$, yields the boundary value problems for the influence functions H_i^{mn} and $P_{kl}^{mn(\Phi)}$

$$\left[L_{ijkl}^{\zeta}(\chi)\left(I_{klmn} + H_{(k,l)}^{mn}(\chi)\right)\right]_{,j} = 0 \quad \text{on} \quad \Theta \tag{23}$$

$$\left[L_{ijkl}^{\zeta}(\chi)\left(P_{kl}^{mn(\Phi)}(\chi) - I_{klmn}^{(\Phi)}\right)\right]_{,j} = 0 \quad \text{on} \quad \Theta \quad \forall\Phi \tag{24}$$

where

15

$$I_{klmn}^{(\Phi)}(\chi) = \begin{cases} I_{klmn} & \chi \in \Theta^{(\Phi)} \\ 0 & \chi \notin \Theta^{(\Phi)} \end{cases} \tag{25}$$

Subjected to periodicity and homogeneous constraints on the average influence functions on each RVE bounding surface

$$\int_{\partial\Theta_I} H_k^{mn}(\chi) d\gamma = 0 \tag{26}$$

$$\int_{\partial\Theta_I} h_k^{mn(\Phi)}(\chi) d\gamma = 0 \tag{27}$$

A discrete solution of (23)-(27) for H_i^{mn} and $P_{kl}^{mn(\Phi)}$ can be obtained by using finite element method. For details see [23,24,25,31].

The reduced order computational RVE problem at each nonlocal quadrature point is constructed as follows. First, an average of $\varepsilon_{kl}^{(\Psi)}, \sigma_{ij}^{(\Psi)}$ in each concrete and steel partition is computed as

$$\varepsilon_{kl}^{(\Psi)}(\hat{X}_I) = E_{klmn}^{(\Psi)} \varepsilon_{mn}^c(\hat{X}_I) + \sum_{\Phi=1}^{\bar{M}} P_{kl}^{mn(\Psi\Phi)} \mu_{mn}^{(\Phi)}(\hat{X}_I) \tag{28}$$

16

$$\sigma_{ij}^{(\Psi)}(\hat{\boldsymbol{X}}_I) = \Sigma_{ijmn}^{(\Psi)}\varepsilon_{mn}^c(\hat{\boldsymbol{X}}_I) + \sum_{\Phi=1}^{\tilde{M}} \Lambda_{ij}^{mn(\Psi\Phi)}\mu_{mn}^{(\Phi)}(\hat{\boldsymbol{X}}_I) \qquad (29)$$

Where

$$E_{klmn}^{(\Psi)} = \frac{1}{\left|\Theta^{(\Psi)}\right|} \int\limits_{\Theta^{(\Psi)}} E_{klmn}(\boldsymbol{\chi})d\Theta \qquad (30)$$

$$\Sigma_{ijmn}^{(\Psi)} = \frac{1}{\left|\Theta^{(\Psi)}\right|} \int\limits_{\Theta^{(\Psi)}} \Sigma_{ijmn}(\boldsymbol{\chi})d\Theta \qquad (31)$$

$$P_{kl}^{mn(\Psi\Phi)} = \frac{1}{\left|\Theta^{(\Psi)}\right|} \int\limits_{\Theta^{(\Psi)}} P_{kl}^{mn(\Phi)}(\boldsymbol{\chi})d\Theta \qquad (32)$$

$$\Lambda_{ij}^{mn(\Psi\Phi)} = \frac{1}{\left|\Theta^{(\Psi)}\right|} \int\limits_{\Theta^{(\Psi)}} \Lambda_{ij}^{mn(\Phi)}(\boldsymbol{\chi})d\Theta \qquad (33)$$

Since partition eigenstrain $\boldsymbol{\mu}^{(\Phi)}$ is a function of partition strain $\boldsymbol{\varepsilon}^{(\Phi)}$ via constitutive equation of that partition, equations (28) comprises a set of $6 \times \tilde{M}$ nonlinear equations with the same number of unknowns that are solved using the Newton method for each nonlocal quadrature point, for every iteration of the macroscopic solution. For details see [23,24,25,31].

2.4 The Coarse-Scale Problem

The weak form of the coarse-scale problem is constructed by choosing the test functions in (6) from the coarse-scale space $w^c \in \mathcal{W}^c$

$$\int_{\Omega^\varsigma} w_i^c \left(\sigma_{ij,j}^\varsigma + b_i^\varsigma \right) d\Omega = 0 \quad \forall w^c \in \mathcal{W}^c \tag{34}$$

where w^c is the C^0 continuous test function on Ω, satisfying homogeneous boundary conditions on $\partial \Omega^u$

$$\mathcal{W}^c = \left\{ w^c \text{defined in } \Omega, C^0\left(\Omega\right), w^c = 0 \text{ on } \partial\Omega^u \right\} \tag{35}$$

The space $\mathcal{W}^c$ will be defined in Chapter 3 for beams and Chapter 4 for plates. Integrating by parts the divergence term, inserting the expression of stress in equation (18) and applying the nonlocal quadrature scheme yields

$$\sum_{I=1}^{\hat{N}} W_I J_I \frac{1}{\left|\Theta_{\hat{X}_I}\right|} \int_{\Theta_{\hat{X}_I}} w_{(i,j)}^c \left(\Sigma_{ijmn} \varepsilon_{mn}^c + \sum_{\Phi=1}^{\tilde{M}} \Lambda_{ij}^{mn\ \Phi}\ _{mech}\mu_{mn}^{(\Phi)} \right) d\Theta = f \qquad \forall \boldsymbol{w}^c \in \mathcal{W}^c \qquad (36)$$

$$f = \int_{\partial\Omega^t} w_i^c\ t_i^\zeta d\Gamma + \int_\Omega w_i^c\ b_i^\zeta d\Omega - {}_0 c \sum_{I=1}^{\hat{N}} W_I J_I \frac{1}{\left|\Theta_{\hat{X}_I}\right|} \int_{\Theta_{\hat{X}_I}} w_{(i,j)}^c \sum_{\Phi=1}^{\tilde{M}} \Lambda_{ij}^{mn\ \Phi}\ _0\mu_{mn}^{(\Phi)} d\Theta \qquad (37)$$

Where the partition eigenstrain $\boldsymbol{\mu}^{(\Phi)}$ has been decomposed into the known initial eigenstrain

$_0\boldsymbol{\mu}^{(\Phi)}$ and the unknown mechanical eigenstrain $_{mech}\boldsymbol{\mu}^{(\Phi)}$. Variable $_0c$ is equal to 1 for creep

and shrinkage eigenstrains and -1 for prestress and temperature.

2.5 Expansion of Coarse Scale Strain

In general the coarse-scale strain-displacement matrix is denoted by

19

$$\mathbf{B}^c = \nabla_s \mathbf{N}^c = \begin{bmatrix} \dfrac{\partial \mathbf{N}_x^c}{\partial x} \\[2ex] \dfrac{\partial \mathbf{N}_y^c}{\partial y} \\[2ex] \dfrac{\partial \mathbf{N}_z^c}{\partial z} \\[2ex] \dfrac{\partial \mathbf{N}_x^c}{\partial y} + \dfrac{\partial \mathbf{N}_y^c}{\partial x} \\[2ex] \dfrac{\partial \mathbf{N}_y^c}{\partial z} + \dfrac{\partial \mathbf{N}_z^c}{\partial y} \\[2ex] \dfrac{\partial \mathbf{N}_x^c}{\partial z} + \dfrac{\partial \mathbf{N}_z^c}{\partial x} \end{bmatrix} \tag{38}$$

where the coarse-scale shape functions $\mathbf{N}^c$ are described in Chapters 3 and 4 for beams and plates respectively, and ∇_s denoting symmetric gradient. Note that a reduced form of equation (38) is used for beams and plates as will be explained in Chapters 3 and 4.

To construct the higher order computational continua formalism, the strain-displacement matrix is expanded as

$$\mathbf{B}^c(\hat{X}_I, \chi) = \mathbf{g}(\chi)\bar{\mathbf{B}}(\hat{X}_I) \tag{39}$$

where

$$\overline{\mathbf{B}}(\hat{\boldsymbol{X}}_I) = \left[\left\langle \mathbf{B}^c \right\rangle_\Theta \quad \left\langle \partial_\alpha \mathbf{B}^c \right\rangle_\Theta \quad \left\langle \partial_{\alpha\beta} \mathbf{B}^c \right\rangle_\Theta \quad \left\langle \partial_{\alpha\beta\gamma} \mathbf{B}^c \right\rangle_\Theta \quad \left\langle \partial_{\alpha\beta\gamma\delta} \mathbf{B}^c \right\rangle_\Theta \quad \left\langle \partial_{\alpha\beta\gamma\delta\varepsilon} \mathbf{B}^c \right\rangle_\Theta \right]^T \quad (40)$$

$$\mathbf{g}(\boldsymbol{\chi}) = \left[1 \quad g_\alpha(\boldsymbol{\chi}) \quad g_{\alpha\beta}(\boldsymbol{\chi}) \quad g_{\alpha\beta\gamma}(\boldsymbol{\chi}) \quad g_{\alpha\beta\gamma\delta}(\boldsymbol{\chi}) \quad g_{\alpha\beta\gamma\delta\varepsilon}(\boldsymbol{\chi}) \right] \quad (41)$$

The differential operators $\partial_\alpha f$, $\partial_{\alpha\beta} f$, $\partial_{\alpha\beta\gamma} f$, $\partial_{\alpha\beta\gamma\delta} f$ and $\partial_{\alpha\beta\gamma\delta\varepsilon} f$ are defined as

$$\partial_{\alpha..\varepsilon} f = \frac{\partial^n f}{\partial \chi_\alpha ... \partial \chi_\varepsilon} \quad (42)$$

with the bracket operator $\left\langle f \right\rangle_\Theta$ denoting the average over Θ

$$\left\langle f \right\rangle_\Theta \equiv \overline{f} = \frac{1}{|\Theta|} \int_\Theta f(\boldsymbol{\chi}) d\Theta \quad (43)$$

In (39)-(41), summation convention over repeated subscripts $\alpha, \beta, \gamma, \delta$ and ε ranging from 1 to 3 is employed. $\mathbf{g}(\boldsymbol{\chi})$ depends on the choice of the coarse-scale element but is independent of its coordinates, which will prove very useful for computational efficiency. Various terms in $\mathbf{g}(\boldsymbol{\chi})$ are obtained by equating (38) and(39); their expressions will be detailed in Chapters 3 and 4.

2.6 Discrete Coarse Scale Equations.

The coarse-scale trial and test function approximation spaces are denoted as

$$\mathcal{W}^{ch} = \left\{ \mathbf{w}^{ch} \text{defined in } \Omega, w^{ch} = \mathbf{N}^c \mathbf{c}^c, \mathbf{w}^{ch} = \mathbf{0} \text{ on } \partial\Omega^u \right\} \qquad (44)$$

$$\mathcal{U}^{ch} = \left\{ \mathbf{u}^{ch} \text{defined in } \Omega, \mathbf{u}^{ch} = \mathbf{N}^c \mathbf{d}^c, \mathbf{u}^{ch} = \bar{\mathbf{u}} \text{ on } \partial\Omega^u \right\} \qquad (45)$$

Inserting the discretization of the test and trial functions (44) into the matrix form of (36) and requiring arbitrariness of the test function coefficients $\mathbf{c}^c$, yields the discrete coarse-scale equilibrium equations

$$\mathbf{r}^c = \mathbf{f}^c_{int} - \mathbf{f}^c_{ext} = \mathbf{0} \qquad (46)$$

where

$$\mathbf{f}_{int}^{c} = \sum_{I=1}^{\hat{N}} W_I J_I \frac{1}{\left|\Theta_{\hat{X}_I}\right|} \int_{\Theta_{\hat{X}_I}} \mathbf{B}^{cT} \left(\Sigma \mathbf{B}^c \mathbf{d}^c + \sum_{\Phi=1}^{\tilde{M}} \Lambda^{(\Phi)}_{\ mech} \boldsymbol{\mu}_I^{(\Phi)} \right) d\Theta \tag{47}$$

$$\mathbf{f}_{ext}^{c} = \int_{\partial\Omega} \mathbf{N}^{cT} \mathbf{t} d\Gamma + \int_{\Omega} \mathbf{N}^{cT} \mathbf{b} d\Omega - {}_0 c \sum_{I=1}^{\hat{N}} W_I J_I \frac{1}{\left|\Theta_{\hat{X}_I}\right|} \int_{\Theta_{\hat{X}_I}} \mathbf{B}^{cT} \sum_{\Phi=1}^{\tilde{M}} \Lambda^{(\Phi)}_{\ 0} \boldsymbol{\mu}_I^{(\Phi)} d\Theta \tag{48}$$

$\mathbf{f}_{int}^{c}$ and $\mathbf{f}_{ext}^{c}$ are the internal and external forces, respectively. Further inserting expansion of

the coarse-scale strain-displacement matrix (39) into (47) and (48) yields

$$\mathbf{f}_{int}^{c} = \sum_{I=1}^{\hat{N}} W_I J_I \frac{1}{\left|\Theta_{\hat{X}_I}\right|} \bar{\mathbf{B}}_I^T \left(\bar{\mathbf{L}} \bar{\mathbf{B}}_I \mathbf{d}^c + \sum_{\Phi=1}^{\tilde{M}} \bar{\mathbf{Z}}^{(\Phi)}_{\ mech} \boldsymbol{\mu}_I^{(\Phi)} \right) \tag{49}$$

$$\mathbf{f}_{ext}^{c} = \int_{\partial\Omega} \mathbf{N}^{cT} \mathbf{t} d\Gamma + \int_{\Omega} \mathbf{N}^{cT} \mathbf{b} d\Omega - {}_0 c \sum_{I=1}^{\hat{N}} W_I J_I \frac{1}{\left|\Theta_{\hat{X}_I}\right|} \bar{\mathbf{B}}_I^T \sum_{\Phi=1}^{\tilde{M}} \bar{\mathbf{Z}}^{(\Phi)}_{\ 0} \boldsymbol{\mu}_I^{(\Phi)} \tag{50}$$

where

$$\bar{\mathbf{L}} = \int_{\Theta_{\hat{X}_I}} \mathbf{g}^T(\boldsymbol{\chi}) \Sigma(\boldsymbol{\chi}) \mathbf{g}(\boldsymbol{\chi}) d\Theta \tag{51}$$

$$\bar{\mathbf{Z}}^{(\Phi)} = \int_{\Theta_{\hat{X}_I}} \mathbf{g}^T(\boldsymbol{\chi}) \Lambda^{(\Phi)}(\boldsymbol{\chi}) d\Theta \tag{52}$$

23

$$\bar{\mathbf{B}}_I = \bar{\mathbf{B}}\left(\hat{X}_I\right) \tag{53}$$

$$_{mech}\boldsymbol{\mu}_I^{(\Phi)} = {}_{mech}\boldsymbol{\mu}^{(\Phi)}\left(\hat{X}_I\right) \tag{54}$$

$$_0\boldsymbol{\mu}_I^{(\Phi)} = {}_0\boldsymbol{\mu}^{(\Phi)}\left(\hat{X}_I\right) \tag{55}$$

The tangent stiffness matrix is obtained by linearization

$$\mathbf{K}^c = \frac{\partial \mathbf{r}^c}{\partial \mathbf{d}^c} = \frac{\partial \mathbf{f}_{int}^c}{\partial \mathbf{d}^c} \tag{56}$$

which yields

$$\mathbf{K}^c = \sum_{I=1}^{\hat{N}} W_I J_I \frac{1}{\left|\Theta_{\hat{X}_I}\right|} \bar{\mathbf{B}}_I^T \left(\bar{\mathbf{L}}\bar{\mathbf{B}}_I + \sum_{\Phi=1}^{\tilde{M}} \bar{\mathbf{Z}}^{(\Phi)} \frac{\partial_{mech}\boldsymbol{\mu}_I^{(\Phi)}}{\partial \mathbf{d}_c} \right) \tag{57}$$

Differentiating $\dfrac{\partial_{mech}\boldsymbol{\mu}_I^{(\Phi)}}{\partial \mathbf{d}_c}$ using the chain rule

$$\frac{\partial_{mech}\boldsymbol{\mu}_I^{(\Phi)}}{\partial \mathbf{d}_c} = \frac{\partial_{mech}\boldsymbol{\mu}_I^{(\Phi)}}{\partial \boldsymbol{\varepsilon}_c} \frac{\partial \boldsymbol{\varepsilon}_c}{\partial \mathbf{d}_c} \tag{58}$$

24

The tangent stiffness $\mathbf{K}^c$ can be expressed as

$$\mathbf{K}^c = \sum_{I=1}^{\hat{N}} W_I J_I \frac{1}{\left|\Theta_{\hat{X}_I}\right|} \overline{\mathbf{B}}_I^T \left(\overline{\mathbf{L}} + \sum_{\Phi=1}^{\tilde{M}} \overline{\mathbf{A}}^{(\Phi)} \frac{\partial_{mech} \boldsymbol{\mu}_I^{(\Phi)}}{\partial \boldsymbol{\varepsilon}^c} \right) \overline{\mathbf{B}}_I \qquad (59)$$

where

$$\overline{\mathbf{A}}^{(\Phi)} = \int_{\Theta_{\hat{X}_I}} \mathbf{g}^T(\boldsymbol{\chi}) \boldsymbol{\Lambda}^{(\Phi)}(\boldsymbol{\chi}) \mathbf{g}(\boldsymbol{\chi}) d\Theta \qquad (60)$$

with $\overline{\mathbf{L}}$ and $\overline{\mathbf{A}}^{(\Phi)}$ being symmetric matrices and $\dfrac{\partial_{mech} \boldsymbol{\mu}^{(\Phi)}}{\partial \boldsymbol{\varepsilon}^c}$ in (59) depending on the choice

of the material model used for the microconstituents. One of the salient features of the

proposed HC^2 formulation is that a variety of materials models can be utilized depending on

the application without overall framework changes.

Remark 1: Observing equation (49) it follows that $\boldsymbol{\sigma}^{tr} = \overline{\mathbf{L}} \overline{\mathbf{B}}_I \mathbf{d}^c$ is a higher order trial stress

corresponding to the response of linear elastic solid, whereas $\boldsymbol{\eta} = \sum_{\Phi=1}^{\tilde{M}} \overline{\mathbf{Z}}^{(\Phi)}{}_m \boldsymbol{\mu}^{(\Phi)}$ is a higher

25

order eigenstress, which a correction in case the deformation process is inelastic. In the O(1) homogenization theory, the expansion (39) would include a single (constant) term, i.e. $g\left(\chi\right)$ =1, in which case $\overline{\mathbf{L}}$ in (51) reduces to overall (homogenized) elastic properties.

<u>Remark 2</u>: Note that tensors $\overline{\mathbf{L}}$, $\overline{\mathbf{Z}}^{(\Phi)}$ and $\overline{\mathbf{A}}^{(\Phi)}$, are independent of coarse scale coordinates therefore they only need to be precomputed once, and will be used for every coarse scale geometry and loading condition.

Chapter 3

The Multiscale Beam

3.1 Introduction to Concrete Beam Elements

The formulation of reinforced concrete structural elements (beams or columns) that incorporates non-linear behavior is typically based on so-called fiber beam-column formulation [7], with one-dimensional models for steel and confined concrete. Cuellar and Gallegos [35] presented a fiber beam-column element that incorporates an isotropic damage model. Recent developments in the fiber beam-column element formulation were detailed by Mohr et al. [8] where three-dimensional behavior was attained by enriching the displacement field with cross-sectional warping and distortion deformation modes and where the cross-section was modeled by planar elements rather than by uniaxial fiber elements.

Beam elements specific for prestressed concrete have been developed as well. Aalami [36] coupled the prestressing steel to the beam element using the tendon as a load resisting element which enables it to capture the prestressing losses. Ayoub and Filippou [37] used a fiber-beam element to model pretension concrete elements. Ayoub [38] extended the formulation

to post-tension beams by using a link element between the fiber-beam and tendon elements, but the shear stresses and prestress losses were not considered in the formulation.

The multiscale beam element for analysis of concrete proposed herein, maintains the simplicity characteristic to three-dimensional beam elements, while providing comparable accuracy of three-dimensional nonlinear continuum elements. The proposed multiscale beam element accurately predicts the creep and shrinkage strains, accounts for tendon losses and variable eccentricity, and captures both the shear and bending failures, all in the computational efficient manner. To ensure simulation results are insensitive to the beam element size, a unique constitutive law rescaling procedure that substantially differs from rescaling employed for continuum elements [39,40,41] is also developed.

3.2 Selection of the Coarse Scale Space for the Beam Element

One of the simplest beam elements is the Euler-Bernoulli beam. Due its simplicity, it lacks higher order terms and assumes no shear deformation. Filonova and Fish [42] developed computational continua formulation for linear elastic plates based on the Reissner-Mindlin kinematical assumption. Due to lack of higher order terms, the shear stresses were not resolved directly, but rather computed by post-processing.

In order to directly, i.e. not by postprocessing [42], resolve the transverse shear strain distribution, we adopt the general third order theory developed by Reddy [43]. In the following, we briefly summarize the kinematics employed in the third-order beam theory

$$u_1 = u_1^0 - x_3\theta_2 + f(x_3,h_3)\gamma_2 - x_2\theta_3 + f(x_2,h_2)\gamma_3 \tag{61}$$

$$u_2 = u_2^0 - x_3\theta_1 \tag{62}$$

$$u_3 = u_3^0 + x_2\theta_1 \tag{63}$$

where u^0, v^0 and w^0 are the mid-surface displacements of the plate in the x, y and z directions, u_i denotes the three-dimensional displacements; u_i^0 the displacement at the centerline of the beam; θ_1 the rotation around the x_1; $\theta_2 = \dfrac{\partial^c u_3^0}{\partial x_1}$ and $\theta_3 = \dfrac{\partial^c u_2^0}{\partial x_1}$; γ_2 and γ_3 are the generalized rotations for the beam around the x_2 and x_3 axis respectively.

Following [43], $f(x_2,h_2) = x_2\left[1 - \dfrac{4}{3}\left(\dfrac{x_2}{h_2}\right)^2\right]$ and $f(x_3,h_3) = x_3\left[1 - \dfrac{4}{3}\left(\dfrac{x_3}{h_3}\right)^2\right]$ where h_3 is the beam height parallel to x_3, and h_2 is the beam width parallel to x_2.

For the finite element discretization, we employ a three-node beam element, where u_2^0, u_3^0, θ_2 and θ_3, are approximated by cubic Hermitian interpolants; u_1^0 by linear interpolants; γ_2 and γ_3 by quadratic interpolants [44].

The beam has a total number of 18 degrees-of-freedom; the end nodes have 8 degrees-of-freedom each and the middle node has rotations γ_2 and γ_3. The degrees-of-freedom at the interior node can be condensed out so that a 16 by 16 element stiffness matrix is considered for the coarse-scale analysis.

The matrix form of the finite element discretization of coarse-scale displacements is given by

$$
\begin{Bmatrix} {}^c u_1 \\ {}^c u_2 \\ {}^c u_3 \end{Bmatrix} = \mathbf{N}^c \begin{Bmatrix} {}^c u_1^1 & {}^c u_2^1 & {}^c u_3^1 & \theta_1^1 & \theta_2^1 & \theta_3^1 & \gamma_2^1 & \gamma_3^1 & {}^c u_1^2 & {}^c u_2^2 & {}^c u_3^2 & \theta_1^2 & \theta_2^2 & \theta_3^2 & \gamma_2^2 & \gamma_3^2 & \gamma_2^3 & \gamma_3^3 \end{Bmatrix}^T \quad (64)
$$

For the beam three-dimensional plane stress conditions are assumed by which $\varepsilon_{22}, \varepsilon_{33}$ are obtained from the condition $\sigma_{22} = \sigma_{33} = 0$. The coarse-scale strain-displacement matrix $\mathbf{B}^c$ in equation (38) reduces to only four strain components defined as

$$
\mathbf{B}^c = \nabla \mathbf{N}^c = \begin{bmatrix} \dfrac{\partial \mathbf{N}_x^c}{\partial x} \\[2mm] \dfrac{\partial \mathbf{N}_x^c}{\partial y} + \dfrac{\partial \mathbf{N}_y^c}{\partial x} \\[2mm] \dfrac{\partial \mathbf{N}_y^c}{\partial z} + \dfrac{\partial \mathbf{N}_z^c}{\partial y} \\[2mm] \dfrac{\partial \mathbf{N}_x^c}{\partial z} + \dfrac{\partial \mathbf{N}_z^c}{\partial x} \end{bmatrix} \quad (65)
$$

The functions $\mathbf{g}(\chi)$ in equation (41) follow from substituting (65) into the left hand of (39) such that

$$
\begin{bmatrix} \dfrac{\partial \mathbf{N}^c_x}{\partial x} \\[2mm] \dfrac{\partial \mathbf{N}^c_x}{\partial y} + \dfrac{\partial \mathbf{N}^c_y}{\partial x} \\[2mm] \dfrac{\partial \mathbf{N}^c_y}{\partial z} + \dfrac{\partial \mathbf{N}^c_z}{\partial y} \\[2mm] \dfrac{\partial \mathbf{N}^c_x}{\partial z} + \dfrac{\partial \mathbf{N}^c_z}{\partial x} \end{bmatrix} = \begin{array}{l} \left\langle \mathbf{B}^c \right\rangle_\Theta + g_\alpha(\chi)\left\langle \partial_\alpha \mathbf{B}^c \right\rangle_\Theta + g_{\alpha\beta}(\chi)\left\langle \partial_{\alpha\beta}\mathbf{B}^c \right\rangle_\Theta + g_{\alpha\beta\gamma}(\chi)\left\langle \partial_{\alpha\beta\gamma}\mathbf{B}^c \right\rangle_\Theta \\[3mm] \qquad + g_{\alpha\beta\gamma\delta}(\chi)\left\langle \partial_{\alpha\beta\gamma\delta}\mathbf{B}^c \right\rangle_\Theta + g_{\alpha\beta\gamma\delta\varepsilon}(\chi)\left\langle \partial_{\alpha\beta\gamma\delta\varepsilon}\mathbf{B}^c \right\rangle_\Theta \end{array} \tag{66}
$$

The coarse scale shape functions $\mathbf{N}^c$ and the corresponding functions $\mathbf{g}(\chi)$ used for the Reddy beam [43] are presented in Section 3.7.

3.3 Representative Volume Element for Beams.

The RVE's for the multiscale beam must have transverse dimensions, equal to the cross section of the beam. For beams with no stirrups the RVE size in the axial direction can be infinitesimal. For three-dimensional RVE's with stirrups, the length in the axial direction must be equal to the stirrup spacing. A typical RVE for a beam with and without stirrups is shown in Figure 3.

|a) 2D unit cell | b) 3D unit cell |
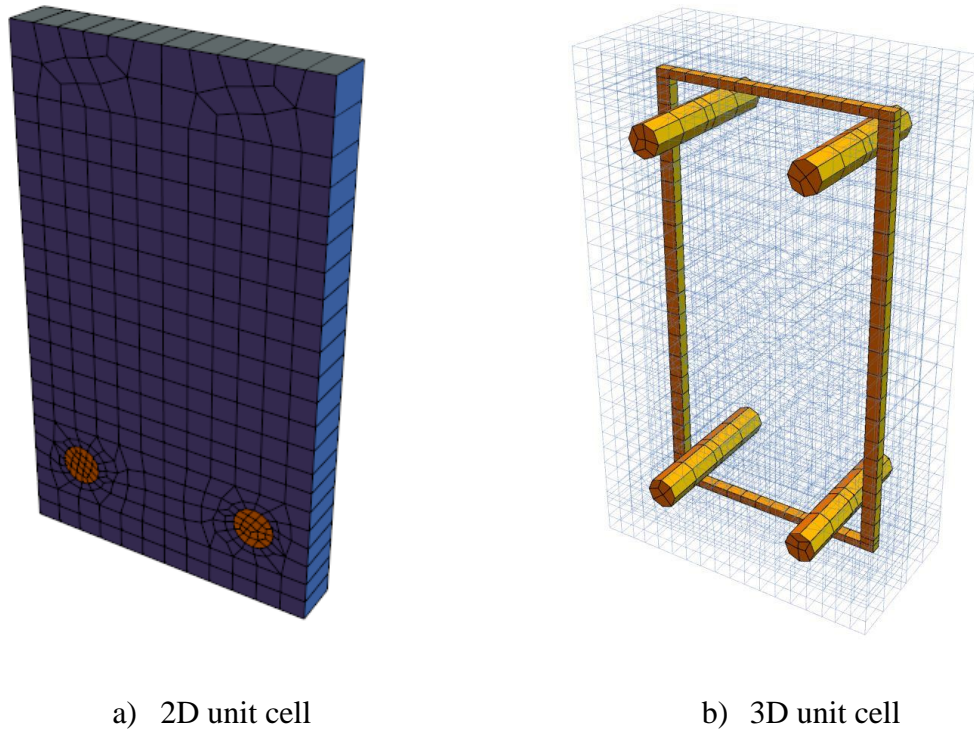
Fig. 3. Two-dimensional (2D) and three-dimensional (3D) RVEs showing different microstructures.

For the RVE depicted in Figure 3b, higher computationally efficiency can be achieved by degenerating the three-dimensional RVE into two-dimensions, as shown in Figure 4. In order to account for the presence of stirrups in the two-dimensional RVE, the constitutive properties of stirrups are modified from an isotropic material in 3D to an orthotropic material in 2D with vanishing axial modulus, $E_{11} = 0$, and the stirrups cross-sectional area in two-dimensions matching the three-dimensional model. This reflects the fact that in the three-dimensional model, stirrups are placed at discrete locations with prescribed spacing affecting only the shear behavior of the beam as opposed to continuous representation of stirrups in two-dimensional model.
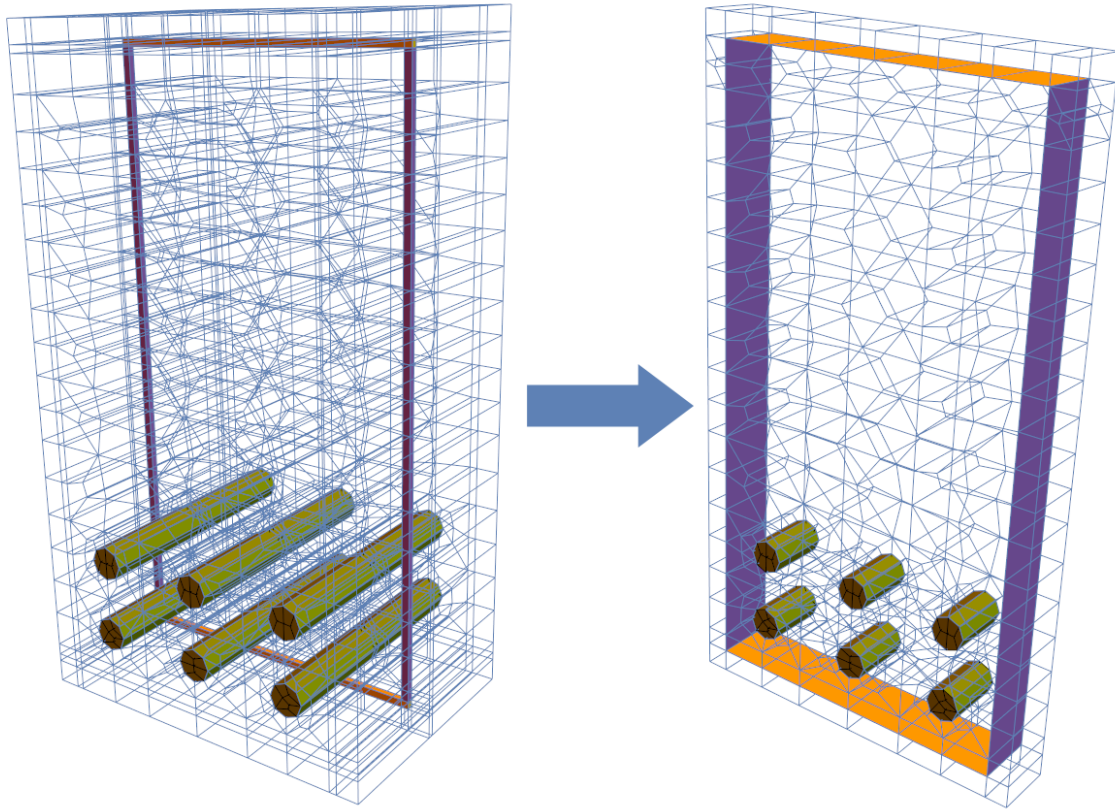
Fig. 4. Degeneration of the three-dimensional RVE to two dimensions.

The width for the stirrup b_{st} in a 2D RVE is given by:

$$\frac{b_{st}}{1} = \frac{A_{st}}{s_{st}^2}$$

(67)

where A_{st} is the area of the stirrup and s_{st} is the stirrup spacing.

3.4 Prestressing Tendon Eccentricity.

In the prestressed concrete beam, the position of the prestressing steel is changing along the beam so that the action of the prestressing balances out the effect of external load acting on the beam [45]. Due to varying position of prestressing, RVEs vary along the beam length. Figure 5 depicts a simply supported beam with a parabolic tendon profile, showing the corresponding RVEs, in meshes consisting of 1, 2 and 4 coarse-scale (beam) elements.
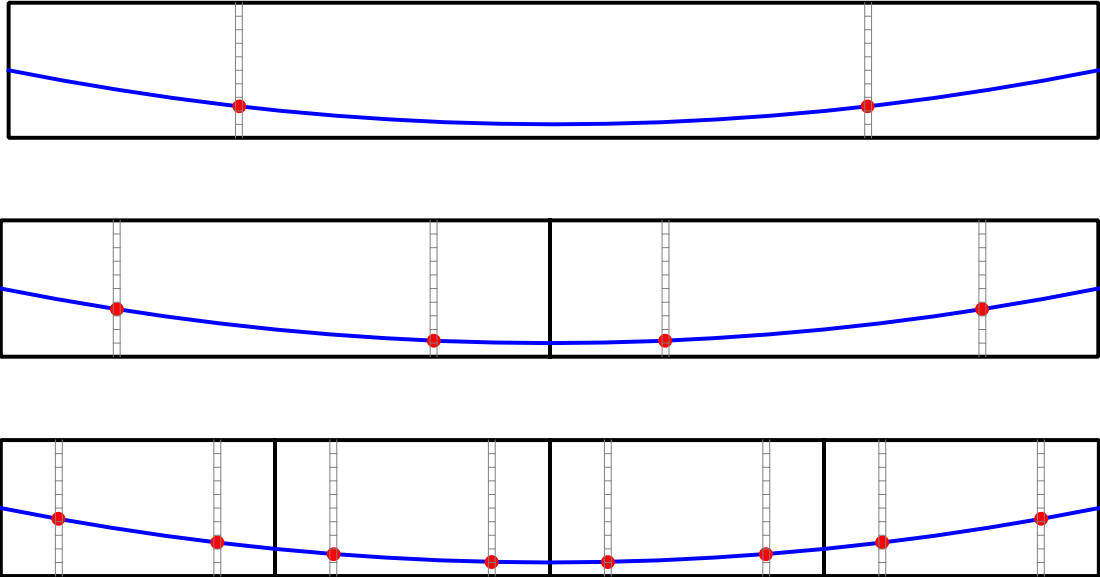
Fig. 5 Position of prestressing steel shown in circles, for a parabolic tendon profile in finite element meshes having 1, 2 and 4 beam elements.

For comparison, the equivalent load for a simply supported beam with a parabolic tendon profile is given by [45]:

$$w_{eq} = \frac{8Py}{S^2} \tag{68}$$

where P is equal to prestress load, S is the beam span, and y is the cable sag at a midpoint measured from a line passing through the cable end points. For a 10 m span beam the theoretical deflection is 6.98mm, while the results using two and four multiscale beam elements are 6.99 mm for an error of 0.13%.

3.5 Initial Strain in the Prestressing Steel.

For the posttension beam, instantaneous losses in the prestressing force [46] due to frictional forces and anchorage slip, must be taken into account. As shown in Figure 5 positions of RVEs depends on the number of coarse-scale elements. The prestressing force less the losses due to friction and anchorage slip, is evaluated at the position of RVEs along the span and the initial strain in the prestressing steel. The initial strain over the steel partitions is used in equation (50) to calculate the equivalent loads for the element.

3.6 Consideration for Creep and Shrinkage.

Creep and shrinkage has been recognized [47,48] as an intricate phenomenon in concrete structures. Modern design codes [3,49] provide estimates of creep and shrinkage strains. To

account for creep and shrinkage effects in the multiscale beam context, requires consideration of the appropriate strains in various partitions throughout the time history. The eigenstrains induced due to creep and shrinkage are calculated for every concrete partition, at every construction stage, and subsequently, time-varying equivalent force vector is computed based on equation (50) throughout the coarse-scale analysis.

3.7 Regularization of the Multiscale Beam Formulation.

Strain softening resulting from damage is known to give rise to mesh size dependency. Among the well-known regularization techniques that circumvent (at least partially) solution dependence on the mesh size are nonlocal methods, rescaling or smeared crack methods and viscous regularization methods (see [39,50] for details and additional references). From a practical point of view, smeared crack or rescaling approaches [39,40,41,51] are advantageous as they only require rescaling of constitutive equations based on the mesh size. The basic idea of these approaches is as follows. When the blunt crack is formed as a result of element removal (or reduction of stress to nearly zero value without element removal) the energy removed from the mesh divided by the new surface introduced should be invariant to the element size. It is a trivial exercise to show that for this to be true, the area under the effective stress-strain curve has to be rescaled by a factor inversely proportional to the characteristic size of the element. The rescaling by a factor proportional to characteristic

element size is a consequence of the fact that the volume of a continuum element removed divided by a new surface introduced is of the order of characteristic element size.

In this section we show that for concrete beams, the rescaling factor should be different than for continuum elements. Consider a beam of span S (Figure 6) subjected to a constant moment that is sufficiently large to induce cracking. In the computational beam model, cracks are formed at the beam element quadrature points. Thus, a new surface area introduced by cracking is equal to the product of the total number of quadrature points, the crack height and the beam width. The volume of the concrete (depicted by a shaded are in Figure 6) where the stress drops to zero (or nearly zero) can be approximated by a product of the distance between the two cracks oriented on the opposite side of the beam, the crack height and the beam width. Figure 6 depicts the ratio of volume and surface area for the beam discretized into 1, 2, 3, 4 and 5 elements of length L_e.

Number of Elements		Volume / Area
1		$\dfrac{\frac{\text{Span}}{\sqrt{3}}\,\text{h}_{\text{crack}}\,\text{W}}{2\times 1\,\text{h}_{\text{crack}}\,\text{W}} = 0.288675\,\text{Span}$
2		$\dfrac{\frac{1}{6}\left(3+\sqrt{3}\right)\text{Span}\,\text{h}_{\text{crack}}\,\text{W}}{2\times 2\,\text{h}_{\text{crack}}\,\text{W}} = 0.197169\,\text{Span}$
3		$\dfrac{\frac{1}{9}\left(6+\sqrt{3}\right)\text{Span}\,\text{h}_{\text{crack}}\,\text{W}}{2\times 3\,\text{h}_{\text{crack}}\,\text{W}} = 0.143186\,\text{Span}$
4		$\dfrac{\frac{1}{12}\left(9+\sqrt{3}\right)\text{Span}\,\text{h}_{\text{crack}}\,\text{W}}{2\times 4\,\text{h}_{\text{crack}}\,\text{W}} = 0.111792\,\text{Span}$
5		$\dfrac{\frac{1}{15}\left(12+\sqrt{3}\right)\text{Span}\,\text{h}_{\text{crack}}\,\text{W}}{2\times 5\,\text{h}_{\text{crack}}\,\text{W}} = 0.091547\,\text{Span}$
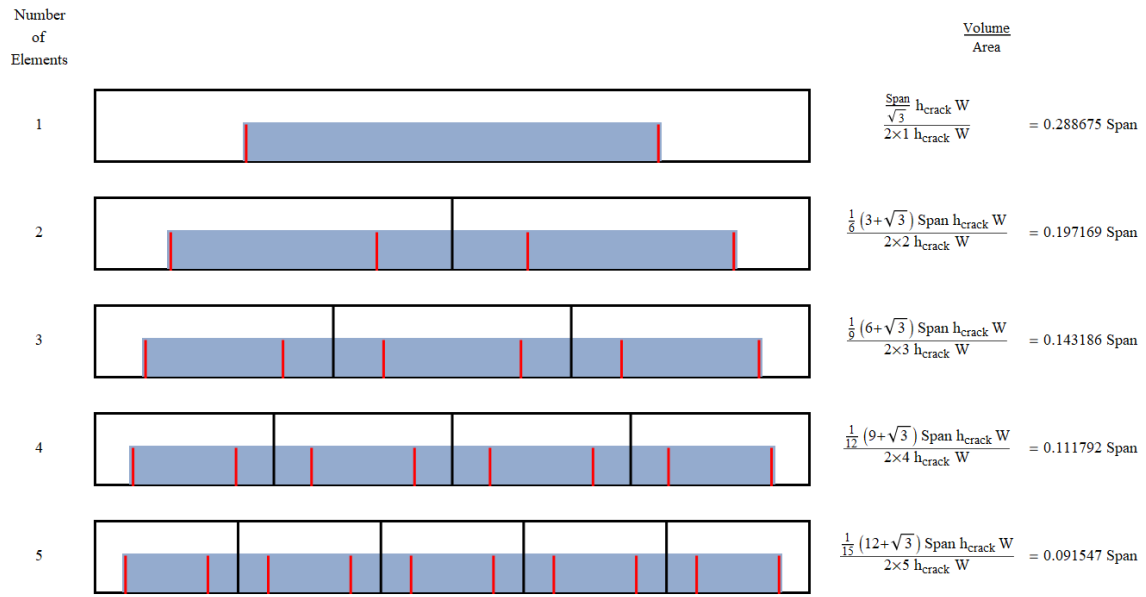
Fig. 6 Ratio of cracked volume to crack surface area for different element lengths

The beam of two elements is considered, $S = 2L_e$, as the baseline for which the constitutive equations were calibrated to fit experimental data. In case of span to element size ratio different than *2*, the material model needs to be rescaled as follows

$$R = \left(\frac{2L_e}{S}\right)^{-0.64} \tag{69}$$

to provide the best fit of the volume to surface area ratios depicted in Figure 3. In the next section we show that with the rescaling introduced in (69) the results are nearly independent of the beam element length.

3.8 Shape Functions for Multiscale Reddy Beam.

The shape functions that satisfy the displacement field described by equations (61) through (63) are defined as

$$
N^c = \begin{bmatrix}
1 - x_1/L & 0 & 0 \\[6pt]
\dfrac{6(L-x_1)x_1x_2}{L^3} & \dfrac{(L-x_1)^2(L+2x_1)}{L^3} & 0 \\[10pt]
\dfrac{6(L-x_1)x_1x_3}{L^3} & 0 & \dfrac{(L-x_1)^2(L+2x_1)}{L^3} \\[10pt]
0 & \left(-1+\dfrac{x_1}{L}\right)x_3 & \dfrac{(L-x_1)x_2}{L} \\[10pt]
\dfrac{(L-3x_1)(L-x_1)x_3}{L^2} & 0 & -\dfrac{(L-x_1)^2 x_1}{L^2} \\[10pt]
-\dfrac{(L-3x_1)(L-x_1)x_2}{L^2} & \dfrac{(L-x_1)^2 x_1}{L^2} & 0 \\[10pt]
\dfrac{(L-2x_1)(L-x_1)x_3\left(1-\dfrac{4x_3^2}{3h^2}\right)}{L^2} & 0 & 0 \\[14pt]
\dfrac{(L-2x_1)(L-x_1)x_2\left(1-\dfrac{4x_2^2}{3b^2}\right)}{L^2} & 0 & 0 \\[14pt]
x_1/L & 0 & 0 \\[6pt]
\dfrac{6x_1(-L+x_1)x_2}{L^3} & \dfrac{(3L-2x_1)x_1^2}{L^3} & 0 \\[10pt]
\dfrac{6x_1(-L+x_1)x_3}{L^3} & 0 & \dfrac{(3L-2x_1)x_1^2}{L^3} \\[10pt]
0 & -\dfrac{x_1x_3}{L} & \dfrac{x_1x_2}{L} \\[10pt]
\dfrac{x_1(-2L+3x_1)x_3}{L^2} & 0 & \dfrac{(L-x_1)x_1^2}{L^2} \\[10pt]
\dfrac{(2L-3x_1)x_1x_2}{L^2} & \dfrac{x_1^2(-L+x_1)}{L^2} & 0 \\[10pt]
-\dfrac{(L-2x_1)x_1x_3\left(1-\dfrac{4x_3^2}{3h^2}\right)}{L^2} & 0 & 0 \\[14pt]
-\dfrac{(L-2x_1)x_1x_2\left(1-\dfrac{4x_2^2}{3b^2}\right)}{L^2} & 0 & 0 \\[14pt]
\dfrac{4(L-x_1)x_1x_3\left(1-\dfrac{4x_3^2}{3h^2}\right)}{L^2} & 0 & 0 \\[14pt]
\dfrac{4(L-x_1)x_1x_2\left(1-\dfrac{4x_2^2}{3b^2}\right)}{L^2} & 0 & 0
\end{bmatrix}^T
\qquad (70)
$$

3.9 Determination of g(χ) Functions for Multiscale Reddy Beam.

The family of $\mathbf{g}(\chi)$ functions corresponding to the Reddy [43] beam formulation are obtained by substituting the known values of

$$\frac{\partial \mathbf{N}_x^c}{\partial x}, \frac{\partial \mathbf{N}_x^c}{\partial y} + \frac{\partial \mathbf{N}_y^c}{\partial x}, \frac{\partial \mathbf{N}_y^c}{\partial z} + \frac{\partial \mathbf{N}_z^c}{\partial y}, \frac{\partial \mathbf{N}_x^c}{\partial z} + \frac{\partial \mathbf{N}_z^c}{\partial x}, \left\langle \mathbf{B}^c \right\rangle_\Theta, \left\langle \partial_\alpha \mathbf{B}^c \right\rangle_\Theta, \left\langle \partial_{\alpha\beta} \mathbf{B}^c \right\rangle_\Theta, \left\langle \partial_{\alpha\beta\gamma} \mathbf{B}^c \right\rangle_\Theta, \left\langle \partial_{\alpha\beta\gamma\delta} \mathbf{B}^c \right\rangle_\Theta$$

and $\left\langle \partial_{\alpha\beta\gamma\delta\varepsilon} \mathbf{B}^c \right\rangle_\Theta$ in (66), and solving for the different values of $\mathbf{g}(\chi)$.

The corresponding nonzero $\mathbf{g}(\chi)$ functions in (39) expressed in RVE coordinates ($\chi_1 = x_1$, $\chi_2 = x_2$, $\chi_3 = x_3$) are given by:

$$g_2 = x_2 \tag{71}$$

$$g_3 = x_3 \tag{72}$$

$$g_{12} = x_1 x_2 \tag{73}$$

$$g_{13} = x_1 x_3 \tag{74}$$

$$g_{22} = -\frac{h_2^{\,2}}{24} + \frac{x_2^{\,2}}{2} \tag{75}$$

$$g_{33} = -\frac{h_3^{\,2}}{24} + \frac{x_3^{\,2}}{2} \tag{76}$$

$$g_{122} = -\frac{1}{8} x_1 \left(h_2^{\,2} - 4 x_2^{\,2} \right) \tag{77}$$

$$g_{133} = -\frac{1}{8} x_1 \left(h_3^{\,2} - 4 x_3^{\,2} \right) \tag{78}$$

$$g_{222} = -\frac{1}{24} x_2 \left(h_2^{\,2} - 4 x_2^{\,2} \right) \tag{79}$$

$$g_{333} = -\frac{1}{24} x_3 \left(h_3^{\,2} - 4 x_3^{\,2} \right) \tag{80}$$

$$g_{1122} = \frac{1}{192} \left(h_2^{\,2} - 4 x_2^{\,2} \right) \left(\left| \Theta \right|_1^2 - 12 x_1^{\,2} \right) \tag{81}$$

$$g_{1133} = \frac{1}{192} \left(h_3^{\,2} - 4 x_3^{\,2} \right) \left(\left| \Theta \right|_1^2 - 12 x_1^{\,2} \right) \tag{82}$$

$$g_{1222} = \frac{1}{24} x_2 \left(-h_2^{\,2} + 4 x_2^{\,2} \right) x_1 \tag{83}$$

$$g_{1333} = \frac{1}{24} x_3 \left(-h_3^{\,2} + 4 x_3^{\,2} \right) x_1 \tag{84}$$

where $\left|\theta\right|_1$ is equal to length of the RVE in the x direction.

For a three-dimensional RVE there are 14 non zero $\mathbf{g}(\chi)$ functions whereas, for a two-dimensional RVE only 6 $\mathbf{g}(\chi)$ functions are needed, to exactly reproduce the variation of coarse scale strain in the RVE.

Chapter 4

The Multiscale Plate Element

4.1 Review of Plate and Shell Elements for Concrete.

The present work builds on an impressive body of literature on plate and shell finite elements for concrete. A glimpse to some of the pertinent research works is given below. Hand et al [52] developed so-called layered approach for a solid concrete slab. Lackner and Mang studied various reinforced concrete models that account for the interaction between concrete and reinforcement [53]. Concrete solid and shell elements were developed in [54] and [55,56], respectively. Mesh-free approaches based on the reproducing kernel particle method have been shown to be very attractive for concrete slab perforation problems [57,58].

Multiscale approaches for shells and plates have recently attracted significant attention. Williams [59] developed a multiscale approach based on the superposition of global and local effects including delamination. Effective utilization of computational homogenization for

reinforced concrete, fiber-reinforced concrete and asphalt concrete can be found in [19,60,61,62,63,64]. Oskay and Pal [65] developed a reduced order homogenization approach for thin plates. A two-level multiscale enrichment approach for analysis of heterogeneous plates was developed in [66] using so-called multiscale enrichment based on the partition of unity (MEPU) approach [67]. A multiscale approach for laminate microstructures accounting for large strains were developed in [68] and later extended to consider dissolution precipitation creep [69]. Multiscale modeling of fiber-reinforced composites by means of proper orthogonal decomposition was studied in [70]; an extension incorporating delamination was given in [71]. Filonova and Fish [42] developed a computational continua formulation for linear elastic plates based on the Reissner-Mindlin kinematical assumption. Due to lack of higher order terms, the shear stresses were not resolved directly, but rather computed by post-processing. Moyeda and Fish [72,73] developed a multiscale beam element for the analysis of reinforced concrete beams with sizeable microstructure and with consideration of initial eigenstrains. For additional noteworthy contributions on the constitutive and multiscale modelling of concrete we refer to a recent book compilation [74].

The existing reinforced concrete plate and shell elements, however, have been mostly limited to analysis of solid reinforced concrete slabs. They are not well-suited to model large representative volume elements (RVEs) characteristic to hollow, ribbed or waffle slabs, commonly used in construction, due to lack of scale separation typical to non-solid slabs. The proposed multiscale approach for reinforced concrete plates is intended to accommodate

44

for non-solid slabs with sizeable periodic structure as well as for the effects of prestressing, creep, shrinkage and temperature. The manuscript presents a multiscale plate element based on the higher order computational continua (HC^2) formulation. The salient features of the proposed formulation are: (i) the ability to consider large representative volume elements (RVE) characteristic to waffle and hollowcore slabs, (ii) versatility stemming from the ease of handling damage, prestressing, creep and shrinkage, and (iii) computational efficiency resulting from model reduction, combined with the classical damage law rescaling method that yields simulation results nearly mesh-size independent.

4.2 Selection of the Discrete Coarse Scale Space Based on Third Order Shear Deformation Plate Element.

Kirchhoff plate elements, which neglect shear deformations, as well as the first order shear deformation elements like the Mindlin-type plate elements, are available in most commercial finite element codes. These types of elements are attractive due to their accuracy and ease of implementation. However, Kirchhoff or Mindlin type plate elements do not accurately capture shear dominated failures typical to concrete slabs. The generalized third-order shear deformation theory developed by Reddy [43] that accounts for a realistic shear distribution throughout the plate thickness is adopted herein for the coarse-scale space. There are several

45

variants of the third-order plate elements [75], of them conforming four-node plate element plate element is considered herein.

To define the spaces in (45), consider a four-node plate element with eight degrees-of-freedom per node, consisting of three displacements u, v, w, the derivatives of the transverse displacement $\dfrac{\partial w}{\partial x}, \dfrac{\partial w}{\partial y}, \dfrac{\partial^2 w}{\partial x \partial y}$ and the generalized rotations ϕ_x and ϕ_y [43] that account for the shear deformation.

The displacement field is expressed as

$$
\begin{aligned}
u &= u^0 - z\frac{\partial w}{\partial x} + z\left[1 - \frac{4}{3}\left(\frac{z}{h}\right)^2\right]\phi_x \\
v &= v^0 - z\frac{\partial w}{\partial y} + z\left[1 - \frac{4}{3}\left(\frac{z}{h}\right)^2\right]\phi_y \\
w &= w^0
\end{aligned}
\tag{85}
$$

where u^0, v^0 and w^0 are the mid-surface displacements of the plate in the x, y and z directions, respectively. The shape functions for u, v, ϕ_x and ϕ_y are the Lagrangian bilinear

interpolation functions, while for $w, \dfrac{\partial w}{\partial x}, \dfrac{\partial w}{\partial y}$ and $\dfrac{\partial^2 w}{\partial x \partial y}$ are the conforming cubic shape

functions [76].

The matrix form of the finite element discretization of coarse-scale displacements is given by

$$\begin{Bmatrix} {}^c u \\ {}^c v \\ {}^c w \end{Bmatrix} = \mathbf{N}^c \left\{ {}^c u^i \quad {}^c v^i \quad {}^c w^i \quad {}^c \frac{\partial w^i}{\partial x} \quad {}^c \frac{\partial w^i}{\partial y} \quad {}^c \frac{\partial^2 w^i}{\partial x \partial y} \quad {}^c \phi_x^i \quad {}^c \phi_y^i \right\}^T \quad for \quad i = 1,2,3,4 \quad (86)$$

For the plate a three-dimensional stress state with vanishing normal stress σ_z is assumed, therefore the coarse-scale strain-displacement matrix $\mathbf{B}^c$ in equation (38) reduces to only five strain components defined as:

$$\mathbf{B}^c = \nabla_s \mathbf{N}^c = \begin{bmatrix} \dfrac{\partial \mathbf{N}_x^c}{\partial x} \\[2mm] \dfrac{\partial \mathbf{N}_y^c}{\partial y} \\[2mm] \dfrac{\partial \mathbf{N}_x^c}{\partial y} + \dfrac{\partial \mathbf{N}_y^c}{\partial x} \\[2mm] \dfrac{\partial \mathbf{N}_y^c}{\partial z} + \dfrac{\partial \mathbf{N}_z^c}{\partial y} \\[2mm] \dfrac{\partial \mathbf{N}_x^c}{\partial z} + \dfrac{\partial \mathbf{N}_z^c}{\partial x} \end{bmatrix} \qquad (87)$$

The functions $\mathbf{g}(\chi)$ in equation (41) follow from substituting (87) into the left hand of (39) such that

$$
\begin{bmatrix}
\dfrac{\partial \mathbf{N}_x^c}{\partial x} \\[2mm]
\dfrac{\partial \mathbf{N}_y^c}{\partial y} \\[2mm]
\dfrac{\partial \mathbf{N}_x^c}{\partial y} + \dfrac{\partial \mathbf{N}_y^c}{\partial x} \\[2mm]
\dfrac{\partial \mathbf{N}_y^c}{\partial z} + \dfrac{\partial \mathbf{N}_z^c}{\partial y} \\[2mm]
\dfrac{\partial \mathbf{N}_x^c}{\partial z} + \dfrac{\partial \mathbf{N}_z^c}{\partial x}
\end{bmatrix}
=
\begin{aligned}
& \langle \mathbf{B}^c \rangle_\Theta + g_\alpha(\chi)\langle \partial_\alpha \mathbf{B}^c \rangle_\Theta + g_{\alpha\beta}(\chi)\langle \partial_{\alpha\beta} \mathbf{B}^c \rangle_\Theta + g_{\alpha\beta\gamma}(\chi)\langle \partial_{\alpha\beta\gamma} \mathbf{B}^c \rangle_\Theta \\
& \quad + g_{\alpha\beta\gamma\delta}(\chi)\langle \partial_{\alpha\beta\gamma\delta} \mathbf{B}^c \rangle_\Theta + g_{\alpha\beta\gamma\delta\varepsilon}(\chi)\langle \partial_{\alpha\beta\gamma\delta\varepsilon} \mathbf{B}^c \rangle_\Theta
\end{aligned}
\tag{88}
$$

The coarse scale shape functions $\mathbf{N}^c$ and its corresponding functions $\mathbf{g}(\chi)$ used for the Reddy plate [43] are presented in Sections 4.5 and 4.6 respectively.

4.3 Representative Volume Element for Plates.

In a similar manner to the beam, the RVE's for the multiscale plate must have depth equal to the slab depth, and its dimensions in x and y must be able to represent the periodicity in the geometry, the reinforcement or both. A typical RVE for a solid and waffle slabs with

48

reinforcement is shown in Figure 3. Note that for the plate all RVE's must be three-dimensional, even for the solid slab, due to the fact that the dimension of the RVE in x and y also represent the rebar spacing.
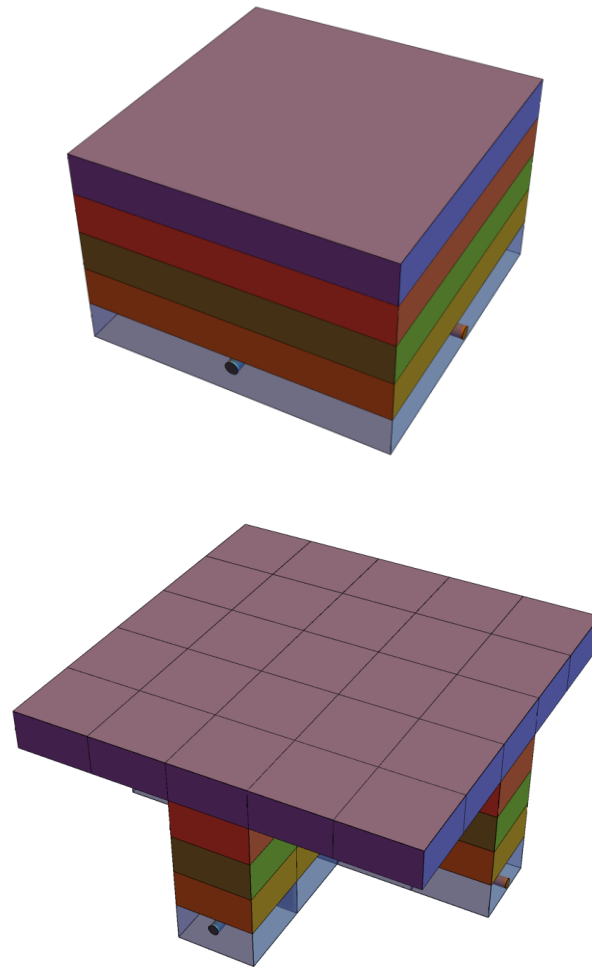
Fig. 7 The RVE of a solid reinforced concrete slab (top) and a waffle reinforced concrete slab (bottom). Each of the two RVEs consist of five concrete partitions and two steel partitions

4.4 Regularization of Plate Elements.

In order to address the mesh size dependency typical to damage models [39,40], a simple regularization approach proposed by Bazant and Oh [77] and Liu et. al. [41] is adopted by which the stress-strain curve is rescaled in proportion to the ratio of the characteristic size of the material h_c and the element size [41,77]. The characteristic size depends on the fracture energy of concrete G_f and the specific energy g_f as follows:

$$h_c = G_f / g_f \tag{89}$$

where

$$g_f = \int_0^\infty \sigma_{ij} d\varepsilon_{ij} \tag{90}$$

In (89), the fracture energy is a given material parameter that can be found in the fib CEB-FIP model code [49] among other places. For all numerical examples involving steel

reinforcement, the strain in the steel reinforcement is assumed to be identical to the strain in

the concrete partition where steel is positioned.

4.5 Shape Function for Plate Elements

The shape functions used for the Reddy plate [43], consistent with displacement field defined

in (85) are given by:

$$
\mathbf{N}^c[1:8] = \left\{ \begin{array}{ccc}
\dfrac{(a-x_1)(b-x_2)}{4ab} & 0 & 0 \\[2mm]
0 & \dfrac{(a-x_1)(b-x_2)}{4ab} & 0 \\[2mm]
\dfrac{3(a-x_1)(a+x_1)(b-x_2)^2(2b+x_2)x_3}{16a^3b^3} & \dfrac{3(a-x_1)^2(2a+x_1)(b-x_2)(b+x_2)x_3}{16a^3b^3} & \dfrac{(a-x_1)^2(2a+x_1)(b-x_2)^2(2b+x_2)}{16a^3b^3} \\[2mm]
\dfrac{(a-x_1)(a+3x_1)(b-x_2)^2(2b+x_2)x_3}{16a^3b^3} & \dfrac{3(a-x_1)^2(a+x_1)(b-x_2)(b+x_2)x_3}{16a^3b^3} & \dfrac{(a-x_1)^2(a+x_1)(b-x_2)^2(2b+x_2)}{16a^3b^3} \\[2mm]
\dfrac{3(a-x_1)(a+x_1)(b-x_2)^2(b+x_2)x_3}{16a^3b^3} & \dfrac{(a-x_1)^2(2a+x_1)(b-x_2)(b+3x_2)x_3}{16a^3b^3} & \dfrac{(a-x_1)^2(2a+x_1)(b-x_2)^2(b+x_2)}{16a^3b^3} \\[2mm]
\dfrac{(a-x_1)(a+3x_1)(b-x_2)^2(b+x_2)x_3}{16a^3b^3} & \dfrac{(a-x_1)^2(a+x_1)(b-x_2)(b+3x_2)x_3}{16a^3b^3} & \dfrac{(a-x_1)^2(a+x_1)(b-x_2)^2(b+x_2)}{16a^3b^3} \\[2mm]
0 & \dfrac{1}{4}\left(1-\dfrac{x_1}{a}\right)\left(1-\dfrac{x_2}{b}\right)x_3\left(1-\dfrac{4x_3^2}{3h^2}\right) & 0 \\[2mm]
\dfrac{1}{4}\left(1-\dfrac{x_1}{a}\right)\left(1-\dfrac{x_2}{b}\right)x_3\left(1-\dfrac{4x_3^2}{3h^2}\right) & 0 & 0
\end{array} \right\}^T
$$

(91)

$$\mathbf{N}^c[9:16] = \left\{ \begin{array}{ccc}
\dfrac{(a+x_1)(b-x_2)}{4ab} & 0 & 0 \\[2ex]
0 & \dfrac{(a+x_1)(b-x_2)}{4ab} & 0 \\[2ex]
-\dfrac{3(a-x_1)(a+x_1)(b-x_2)^2(2b+x_2)x_3}{16a^3b^3} & \dfrac{3(2a-x_1)(a+x_1)^2(b-x_2)(b+x_2)x_3}{16a^3b^3} & \dfrac{(2a-x_1)(a+x_1)^2(b-x_2)^2(2b+x_2)}{16a^3b^3} \\[2ex]
\dfrac{(a-3x_1)(a+x_1)(b-x_2)^2(2b+x_2)x_3}{16a^3b^3} & -\dfrac{3(a-x_1)(a+x_1)^2(b-x_2)(b+x_2)x_3}{16a^3b^3} & -\dfrac{(a-x_1)(a+x_1)^2(b-x_2)^2(2b+x_2)}{16a^3b^3} \\[2ex]
-\dfrac{3(a-x_1)(a+x_1)(b-x_2)^2(b+x_2)x_3}{16a^3b^3} & \dfrac{(2a-x_1)(a+x_1)^2(b-x_2)(b+3x_2)x_3}{16a^3b^3} & \dfrac{(2a-x_1)(a+x_1)^2(b-x_2)^2(b+x_2)}{16a^3b^3} \\[2ex]
\dfrac{(a-3x_1)(a+x_1)(b-x_2)^2(b+x_2)x_3}{16a^3b^3} & -\dfrac{(a-x_1)(a+x_1)^2(b-x_2)(b+3x_2)x_3}{16a^3b^3} & -\dfrac{(a-x_1)(a+x_1)^2(b-x_2)^2(b+x_2)}{16a^3b^3} \\[2ex]
0 & \dfrac{(a+x_1)\left(1-\dfrac{x_2}{b}\right)x_3\left(1-\dfrac{4x_3^2}{3h^2}\right)}{4a} & 0 \\[2ex]
\dfrac{(a+x_1)\left(1-\dfrac{x_2}{b}\right)x_3\left(1-\dfrac{4x_3^2}{3h^2}\right)}{4a} & 0 & 0
\end{array} \right\}^T$$

$$(92)$$

$$\mathbf{N}^c[17:24] = \left\{ \begin{array}{ccc}
\dfrac{(a+x_1)(b+x_2)}{4ab} & 0 & 0 \\[2ex]
0 & \dfrac{(a+x_1)(b+x_2)}{4ab} & 0 \\[2ex]
-\dfrac{3(a-x_1)(a+x_1)(2b-x_2)(b+x_2)^2 x_3}{16a^3b^3} & -\dfrac{3(2a-x_1)(a+x_1)^2(b-x_2)(b+x_2)x_3}{16a^3b^3} & \dfrac{(2a-x_1)(a+x_1)^2(2b-x_2)(b+x_2)^2}{16a^3b^3} \\[2ex]
\dfrac{(a-3x_1)(a+x_1)(2b-x_2)(b+x_2)^2 x_3}{16a^3b^3} & \dfrac{3(a-x_1)(a+x_1)^2(b-x_2)(b+x_2)x_3}{16a^3b^3} & -\dfrac{(a-x_1)(a+x_1)^2(2b-x_2)(b+x_2)^2}{16a^3b^3} \\[2ex]
\dfrac{3(a-x_1)(a+x_1)(b-x_2)(b+x_2)^2 x_3}{16a^3b^3} & \dfrac{(2a-x_1)(a+x_1)^2(b-3x_2)(b+x_2)x_3}{16a^3b^3} & -\dfrac{(2a-x_1)(a+x_1)^2(b-x_2)(b+x_2)^2}{16a^3b^3} \\[2ex]
-\dfrac{(a-3x_1)(a+x_1)(b-x_2)(b+x_2)^2 x_3}{16a^3b^3} & -\dfrac{(a-x_1)(a+x_1)^2(b-3x_2)(b+x_2)x_3}{16a^3b^3} & \dfrac{(a-x_1)(a+x_1)^2(b-x_2)(b+x_2)^2}{16a^3b^3} \\[2ex]
0 & \dfrac{(a+x_1)(b+x_2)x_3\left(1-\dfrac{4x_3^2}{3h^2}\right)}{4ab} & 0 \\[2ex]
\dfrac{(a+x_1)(b+x_2)x_3\left(1-\dfrac{4x_3^2}{3h^2}\right)}{4ab} & 0 & 0
\end{array} \right\}^T$$

$$(93)$$

52

$$
\mathbf{N}^c[25{:}32] = \left\{
\begin{array}{ccc}
\dfrac{(a-x_1)(b+x_2)}{4ab} & 0 & 0 \\[2ex]
0 & \dfrac{(a-x_1)(b+x_2)}{4ab} & 0 \\[2ex]
\dfrac{3(a-x_1)(a+x_1)(2b-x_2)(b+x_2)^2 x_3}{16a^3b^3} & -\dfrac{3(a-x_1)^2(2a+x_1)(b-x_2)(b+x_2)x_3}{16a^3b^3} & \dfrac{(a-x_1)^2(2a+x_1)(2b-x_2)(b+x_2)^2}{16a^3b^3} \\[2ex]
\dfrac{(a-x_1)(a+3x_1)(2b-x_2)(b+x_2)^2 x_3}{16a^3b^3} & -\dfrac{3(a-x_1)^2(a+x_1)(b-x_2)(b+x_2)x_3}{16a^3b^3} & \dfrac{(a-x_1)^2(a+x_1)(2b-x_2)(b+x_2)^2}{16a^3b^3} \\[2ex]
-\dfrac{3(a-x_1)(a+x_1)(b-x_2)(b+x_2)^2 x_3}{16a^3b^3} & \dfrac{(a-x_1)^2(2a+x_1)(b-3x_2)(b+x_2)x_3}{16a^3b^3} & -\dfrac{(a-x_1)^2(2a+x_1)(b-x_2)(b+x_2)^2}{16a^3b^3} \\[2ex]
-\dfrac{(a-x_1)(a+3x_1)(b-x_2)(b+x_2)^2 x_3}{16a^3b^3} & \dfrac{(a-x_1)^2(a+x_1)(b-3x_2)(b+x_2)x_3}{16a^3b^3} & -\dfrac{(a-x_1)^2(a+x_1)(b-x_2)(b+x_2)^2}{16a^3b^3} \\[2ex]
0 & \dfrac{\left(1-\frac{x_1}{a}\right)(b+x_2)x_3\left(1-\frac{4x_3^2}{3h^2}\right)}{4b} & 0 \\[2ex]
\dfrac{\left(1-\frac{x_1}{a}\right)(b+x_2)x_3\left(1-\frac{4x_3^2}{3h^2}\right)}{4b} & 0 & 0
\end{array}
\right\}^{T}
$$

(94)

where *a* and *b* are equal to half the length of the plate in the *x* and *y* directions respectively and *h* is equal to the thickness of the plate.

4.6 Derivation of g(χ) Function for the Multiscale Reddy Plate.

The **g(χ)** functions for the Reddy Plate [XX] formulation are obtained by substituting the

known values of $\dfrac{\partial \mathbf{N}_x^c}{\partial x}, \dfrac{\partial \mathbf{N}_y^c}{\partial y}, \dfrac{\partial \mathbf{N}_x^c}{\partial y} + \dfrac{\partial \mathbf{N}_y^c}{\partial x}, \dfrac{\partial \mathbf{N}_y^c}{\partial z} + \dfrac{\partial \mathbf{N}_z^c}{\partial y}, \dfrac{\partial \mathbf{N}_x^c}{\partial z} + \dfrac{\partial \mathbf{N}_z^c}{\partial x},$

$\left\langle \mathbf{B}^c \right\rangle_\Theta, \left\langle \partial_\alpha \mathbf{B}^c \right\rangle_\Theta, \left\langle \partial_{\alpha\beta} \mathbf{B}^c \right\rangle_\Theta, \left\langle \partial_{\alpha\beta\gamma} \mathbf{B}^c \right\rangle_\Theta, \left\langle \partial_{\alpha\beta\gamma\delta} \mathbf{B}^c \right\rangle_\Theta$ and $\left\langle \partial_{\alpha\beta\gamma\delta\varepsilon} \mathbf{B}^c \right\rangle_\Theta$ in (88), and solving

for the different values of $\mathbf{g}(\chi)$.

The corresponding nonzero $\mathbf{g}(\chi)$ functions in (39) expressed in RVE coordinates ($\chi_1 = x$,

$\chi_2 = y$, $\chi_3 = z$) are given by:

$$g_1 = x \tag{95}$$

$$g_2 = y \tag{96}$$

$$g_3 = z \tag{97}$$

$$g_{13} = xz \tag{98}$$

$$g_{23} = yz \tag{99}$$

$$g_{33} = \frac{z^2}{2} - \frac{h^2}{24} \tag{100}$$

$$g_{113} = \frac{1}{24} z \left(12x^2 - |\theta|_x^2 \right) \tag{101}$$

$$g_{123} = xyz \tag{102}$$

$$g_{133} = -\frac{1}{24} x \left(h^2 - 12z^2 \right) \tag{103}$$

$$g_{223} = \frac{1}{24} z \left(12y^2 - |\theta|_y^2 \right) \tag{104}$$

$$g_{233} = -\frac{1}{24} y \left(h^2 - 12z^2 \right) \tag{105}$$

$$g_{333} = -\frac{1}{24} z \left(h^2 - 4z^2 \right) \tag{106}$$

$$g_{1113} = \frac{1}{24} xz \left(4x^2 - \left| \theta \right|_x^2 \right) \tag{107}$$

$$g_{1123} = \frac{1}{24} yz \left(12x^2 - \left| \theta \right|_x^2 \right) \tag{108}$$

$$g_{1223} = \frac{1}{24} xz \left(12y^2 - \left| \theta \right|_y^2 \right) \tag{109}$$

$$g_{1233} = -\frac{1}{8} xy \left(h^2 - 4z^2 \right) \tag{110}$$

$$g_{1333} = \frac{1}{24} xz \left(-h^2 + 4z^2 \right) \tag{111}$$

$$g_{2223} = \frac{1}{24} yz \left(4y^2 - \left| \theta \right|_y^2 \right) \tag{112}$$

$$g_{2333} = \frac{1}{24} yz \left(-h^2 + 4z^2 \right) \tag{113}$$

$$g_{11123} = \frac{1}{24} xyz \left(4x^2 - \left| \theta \right|_x^2 \right) \tag{114}$$

$$g_{11223} = \frac{1}{576} z \left(12x^2 - \left| \theta \right|_x^2 \right) \left(12y^2 - \left| \theta \right|_y^2 \right) \tag{115}$$

$$g_{12223} = \frac{1}{24} xyz \left(4y^2 - \left| \theta \right|_y^2 \right) \tag{116}$$

where $\left| \theta \right|_x$ and $\left| \theta \right|_x$ are the dimensions of the RVE in the *x* and *y* directions respectively.

For a plate RVE there are 22 non zero $\mathbf{g}(\chi)$ functions to exactly reproduce the variation of

coarse scale strain in the RVE.

Chapter 5

Numerical Examples

5.1 Verification for the Elastic Layered Beam

A layered cantilever beam with a rectangular cross-section is considered herein. All dimensions are normalized. The beam depth is 2.0 units; its width is 1.0; the top and bottom layers are 0.5 in depth with a Young's Modulus $E_1 = 100$ and Poisson's ratio of 0.0; the middle layer is softer with thickness of 1.0 and Young's Modulus $E_2=10$ and Poisson's ratio of 0.0. The length of the beam is equal to 16.0; a load of 0.04 units is applied at the tip of the cantilever as shown in Figure 8. The RVE is shown in Figure 9. Note that the RVE size in the axial direction can be arbitrary. One may consider it to be very small in comparison to the beam length, in which case the RVEs are positioned in the Gauss quadrature points. Otherwise, RVE centroids have to be positioned based on their relative size to the beam span as described by the nonlocal quadrature points. One of the salient features of the HC^2 formulation is that the *final results are invariant to the RVE size in the axial direction*.
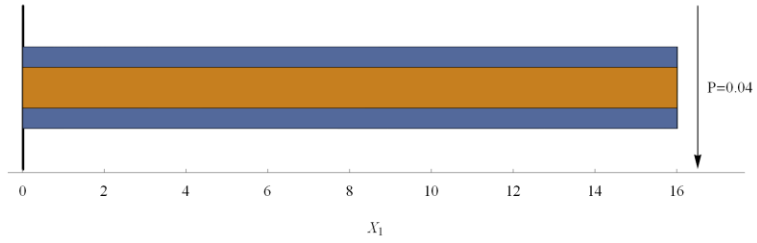
Fig. 8. Beam Elevation
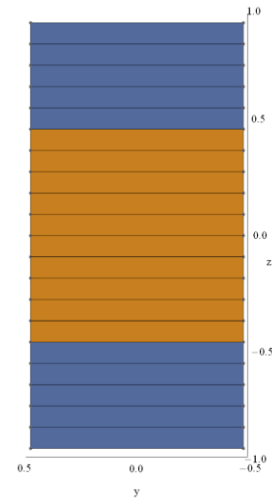
Fig. 9. RVE mesh

The HC^2 simulation results of the cantilever bending are compared to the direct numerical simulation (DNS) where the finite element mesh consists of 6,144 eight-node hexahedral elements. The results as obtained by the HC^2 and DNS simulations are summarized in Table 1.

a) σ_{11} b) σ_{13}
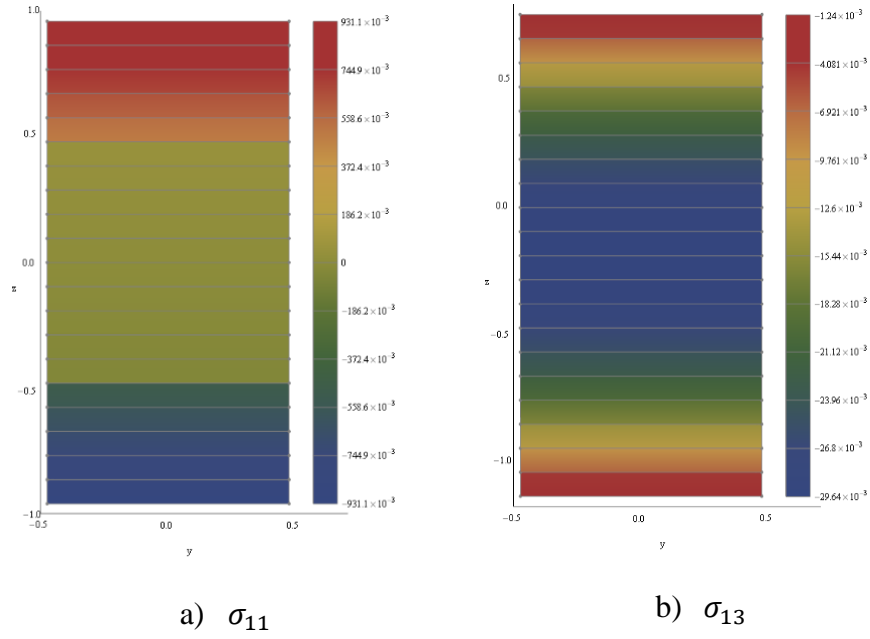
Fig. 10. Normal and shear stresses computed in a cross-section at $x = 2$.

Table 1. Comparison of the HC^2 and DNS simulations for the elastic layered beam.

Analysis Type	Number of Coarse-Scale Elements	Tip Deflection	Error	Maximum Normal Stress @ x=2.0	Error	Maximum Shear Stress	Error
DNS	6144	-0.9731	0.0%	0.933	0.0%	N.A.	N.A.
HC^2	1	-0.9647	-0.9%	0.927	-0.6%	0.0291	
HC^2	2	-0.9647	-0.9%	0.931	-0.2%	0.0282	
HC^2	4	-0.9646	-0.9%	0.937	0.4%	0.0270	
HC^2	8	-0.9646	-0.9%	0.919	-1.6%	0.0268	

The accuracy of the layered beam problem was compared for different RVE's sizes, using conventional Gauss integration and nonlocal quadrature points used in HC^2 formulation. The error in the tip displacement is plotted in Figure 11. It can be seen that the use of the nonlocal quadrature scheme is necessary to maintain accuracy as the size of the RVE increases.
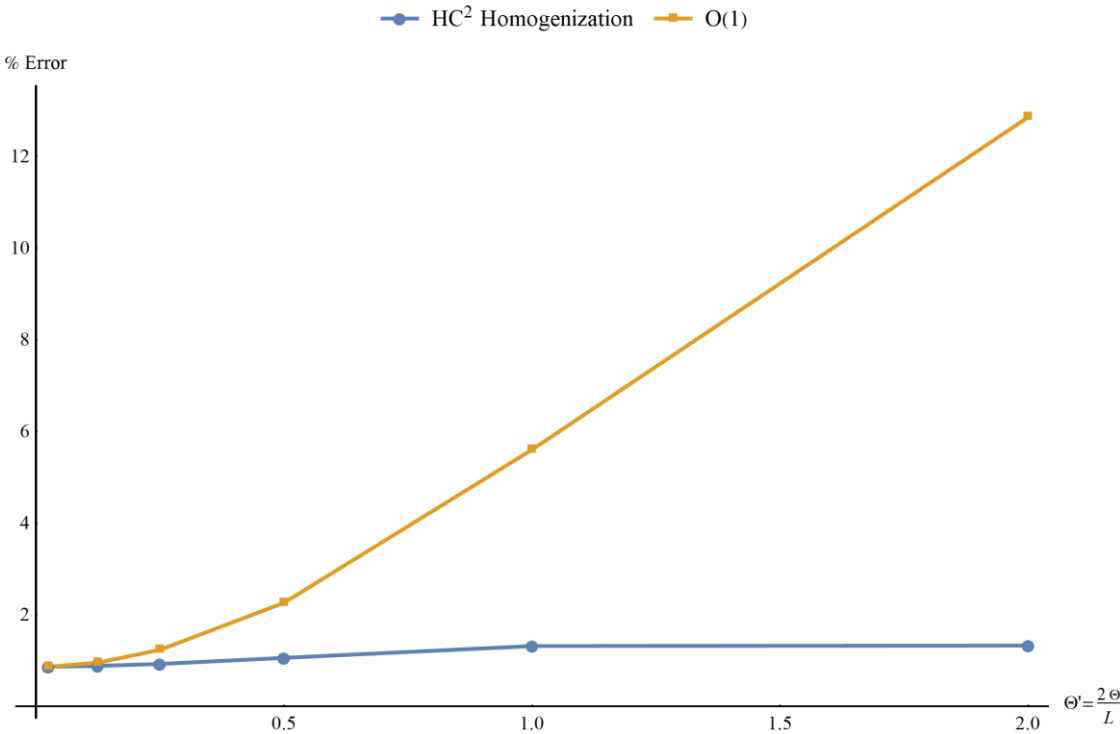
Fig. 11. Comparison of error in the tip displacement for the layered beam versus RVE size using HC^2 and O(1) homogenization approaches

5.2 In Plane Bending of a Plate with Soft Filling.

A cantilever plate with soft filling is studied using HC^2 and compared to the DNS. The geometry of the plate is shown in Figure 12. Various RVEs used in the analysis are depicted in Figure 13. Since the plate properties vary in two directions x_1 and x_3, it is necessary to consider three-dimensional unit cell.

The plate has a depth of 2.0 units and a width of 0.2; the soft filling inclusions have a depth of 1.6 units and axial length of 1.8. The cantilever length is 8.0 and the load at the tip is 0.001 units. The plate has a modulus of elasticity $E_1 = 100$ and a Poisson's ratio $v_1 = 0$; the soft inclusion filling has a modulus of elasticity $E_2 = 10$ and a Poisson's ratio $v_2 = 0$.
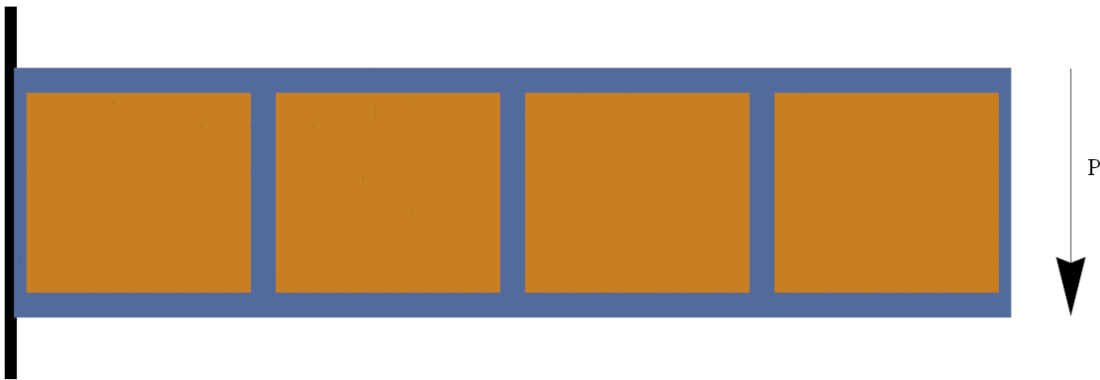
Fig. 12. Bending of a cantilever plate with a soft filling.
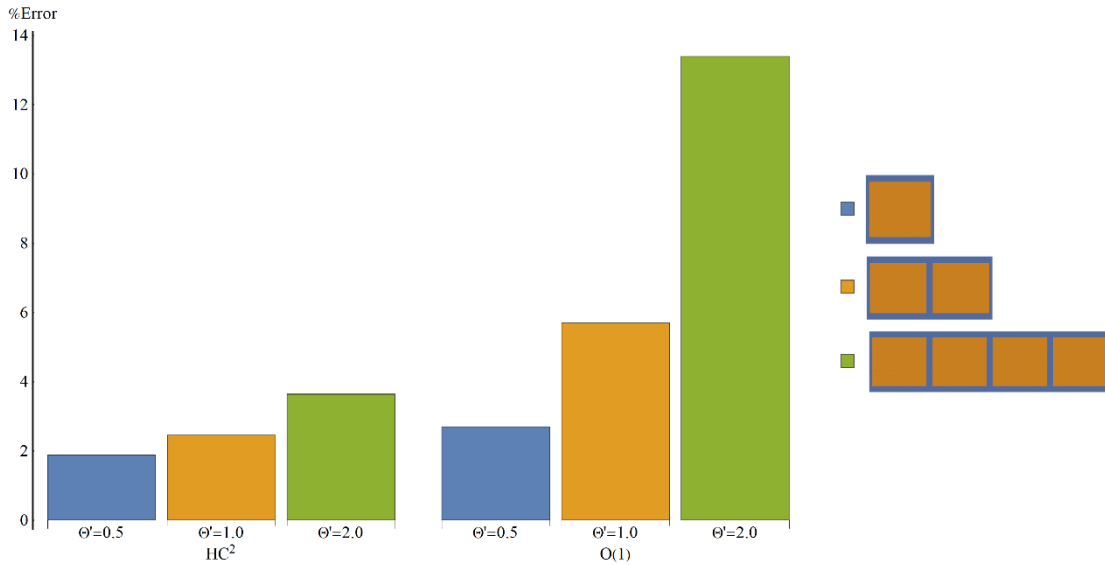
Fig. 13. Comparison of error in tip displacement of the cantilever plate versus RVE size using HC^2 and the O(1) homogenization.

Table 2. Comparison of the HC^2 and O(1) approaches for the cantilever plate.

Analysis Type	Number of Coarse-Scale Elements	Size of RVE	Θ'	Tip Deflection HC^2	Error	Tip Deflection Order 1	Error
DNS	3200	N.A.	N.A.	0.0270	0.0%	0.0270	0.0%
HC^2	1	2	0.5	0.0265	-1.9%	0.0262	-3.0%
HC^2	1	4	1	0.0263	-2.6%	0.0254	-5.9%
HC^2	1	8	2	0.0260	-3.7%	0.0234	-13.3%

With the classical O(1) homogenization the error increases with increase in the size of the RVE, whereas using HC^2 formulation the error remains constant and is independent of the RVE size. This invariance is due to the fact that positions of the quadrature points in the HC^2 formulation are a function of the RVE size. The results obtained by HC^2 and O(1) homogenization are summarized in Figure 13.

5.3 Validation for the Leonhardt Inelastic Shear Beam.

We consider a simply supported reinforced concrete beam subjected to a pair of loads applied near the center of the beam as shown in Figure 14. This problem known as the "Stuttgart shear test", has been experimentally studied by Leonhardt and Walther [78].
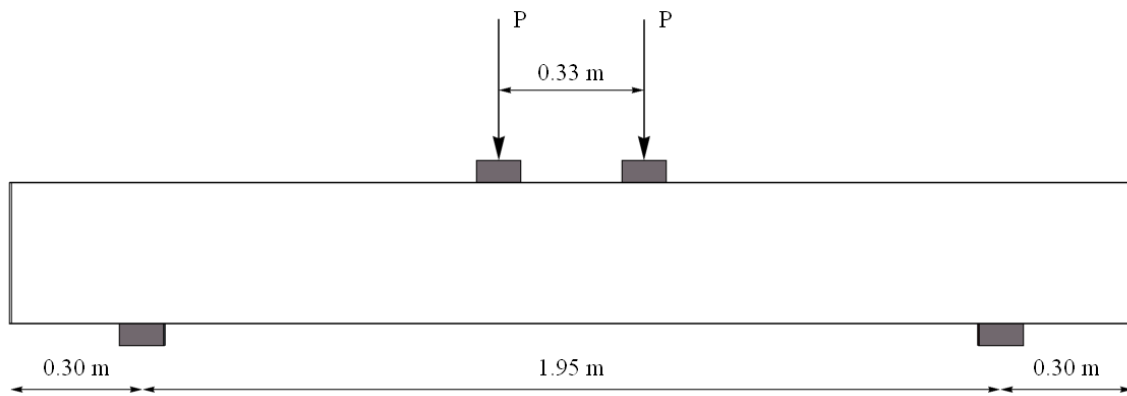
Fig. 14 Leonhardt shear beam test setup [78].

The beam of depth of 0.32 m and width of 0.19 m, is reinforced with 1060 mm^2 steel positioned at 0.05 m from the bottom of the beam. The beam has no stirrups. The steel has a

yield stress of 560 MPa, a modulus of elasticity of 208 GPa, and a Poisson's ratio of 0.3. The steel is modeled as an elastic – perfectly plastic material.

Throughout the thesis, for the constitutive modeling of concrete, we assume an isotropic damage model proposed by Pijaudier-Cabot and Mazars [10] with damage parameters At, Bt, Ac and Bc obtained using the following two-step procedure. We first reconstruct the stress-strain curves (in tension and compression) based on the guidelines suggested in [49] for the specified concrete grade. Secondly, we employ inverse optimization procedures to identify damage model parameters that provide the best fit to the reconstructed stress-strain curves in step one. The concrete was assumed to have the properties presented in Table A.1.

A vertical displacement at the location of point loads in the amount of 5 mm was prescribed over 200 equal load increments. The plot of the displacement at the center of the beam versus the reaction force at one of the supports is shown in Figure 15. Simulation results were compared to the experimental results reported in [78].
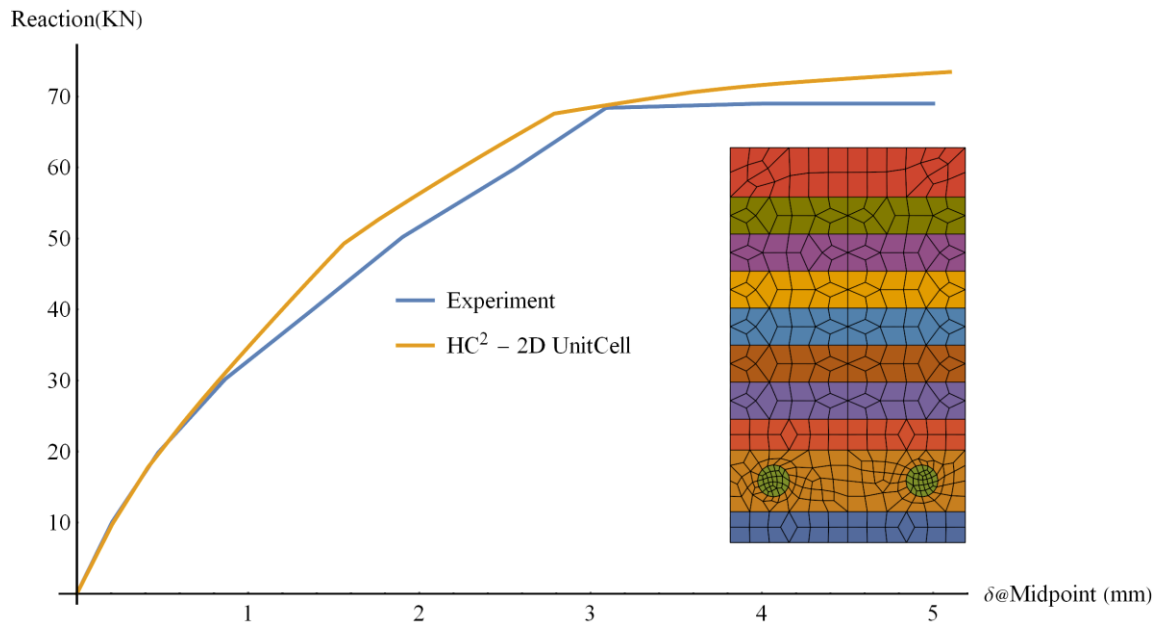
Fig. 15 Leonhardt shear beam: Deflection at a midspan. HC^2 simulations versus experiments [78].

Using the direction of the maximum principal strain obtained from equation (11) and the value of the damage parameter in each RVE positioned at the macroscopic quadrature points, a qualitative plot of the cracking pattern is obtained and compared to the experimental cracking reported in [78]. Cracks are drawn perpendicular to the maximum principal strain in all RVE partitions where damage parameter reaches the value of 1.0. In the present example, the RVE in the axial direction is assumed to be sufficiently small so that the nonlocal quadrature points coincide with the Gauss quadrature points in the axial direction. The results for the cracking pattern are shown in Fig. 16.

Fig. 16. Cracking pattern in the RVEs positioned at the coarse-scale Gauss quadrature

points compared with the experimental cracks [78].

5.4 Numerical Simulation of a Beam with Stirrups.

We consider a simply supported beam, which was tested at the University of California at Berkeley by Bresler and Scorderlis [79]. A diagram showing the test setup for the specimen A-3 is shown in Figure 17. The test results were compared to the results obtained using the HC^2 formulation.
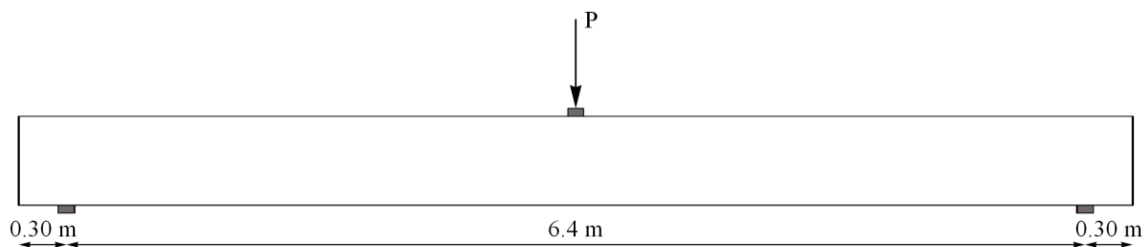
Fig. 17 Simply supported beam setup. The specimen A-3 [79].

The beam of depth and width of 0.56 m and 0.31 m, respectively, is reinforced with 3948 mm^2 steel bars positioned at 0.095 m from the bottom of the beam. The stirrups are No. 2 bars with an area of 32 mm^2 spaced @ 0.21 m. The yield stress of the steel is 552 MPa for the longitudinal bars and 325 MPa for the stirrups. The Young's modulus is 200 GPa, and the Poisson's ratio is 0.3. The steel is modeled as an elastic – perfectly plastic material.

The isotropic damage model of Mazars [10] was again employed for the concrete. The materials parameters considered for the concrete are listed in Table A.1.

The analysis was conducted by prescribing the vertical displacement in the amount of 0.35 mm at the midspan over 200 equal increments. The plot of the displacement at the center of the beam versus the reaction force in one of the supports is shown in Figure 18. The HC^2 simulation results were compared with the experimental results reported in [79]. Figure 3 shows the two-dimensional and three-dimensional RVEs used in the analysis.
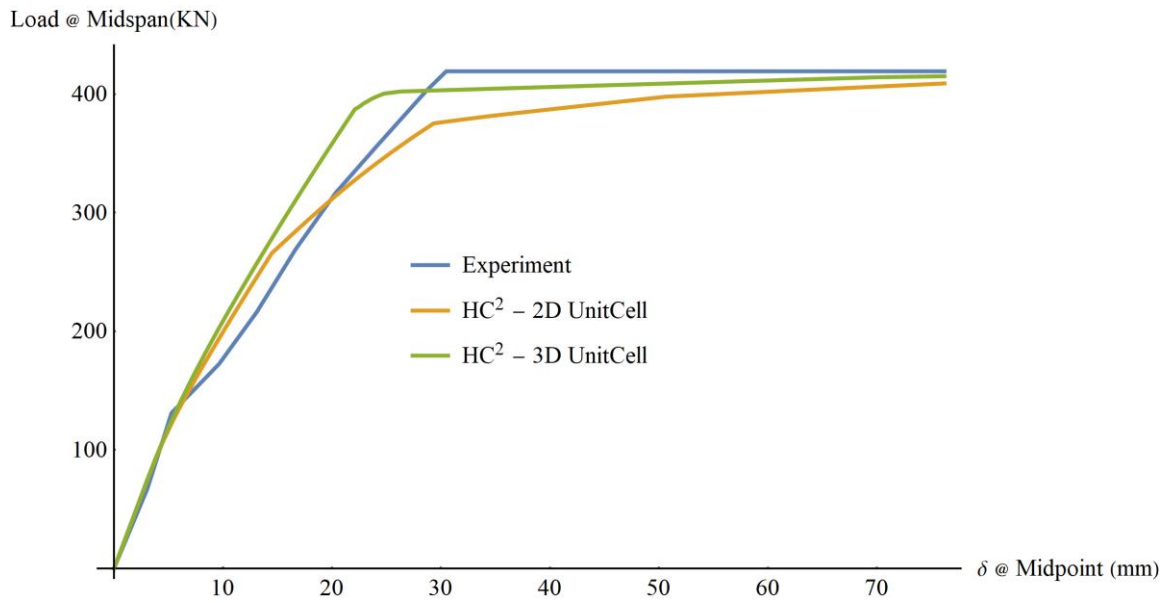
Fig. 18 Simply supported beam with stirrups: Deflection at the midspan. HC^2 simulations versus experiments [79].

As in the Leonhardt beam the cracking pattern is obtained and compared to the experimental solution as reported in [79].

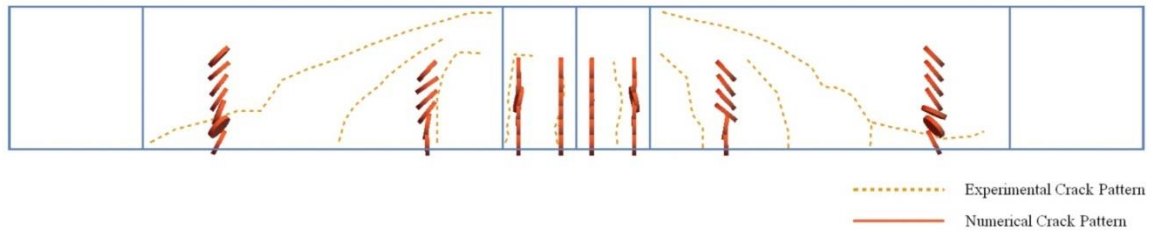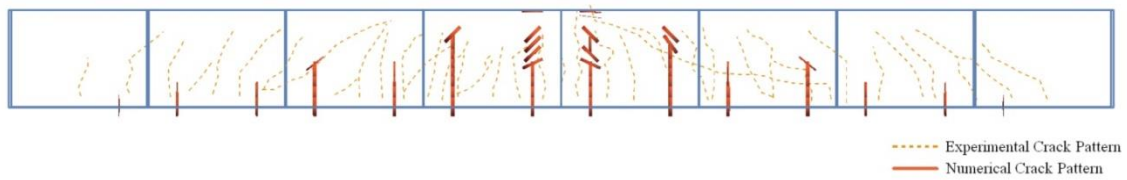

Fig. 19 Cracking pattern in the RVEs positioned at the coarse-scale Gauss quadrature points compared with the experimental cracks in example 4.4. [79].

68

5.5 Verification of Rescaling Approach.

We first study the rescaling approach introduced in equation (69) by considering the beam tested by Saqan and Frosch [80]. The beam is simply supported with a span of 4.06 m, a width of 356 mm and a depth of 711 mm as shown in Figure 20. The beam is reinforced with four 12.7 mm straight prestressing strands with an ultimate strength of 1862 MPa. The concrete has a compressive strength of 52.1 MPa. For the experimental beam in [80] the material parameters are listed in Table A.2.

P

2032   2032
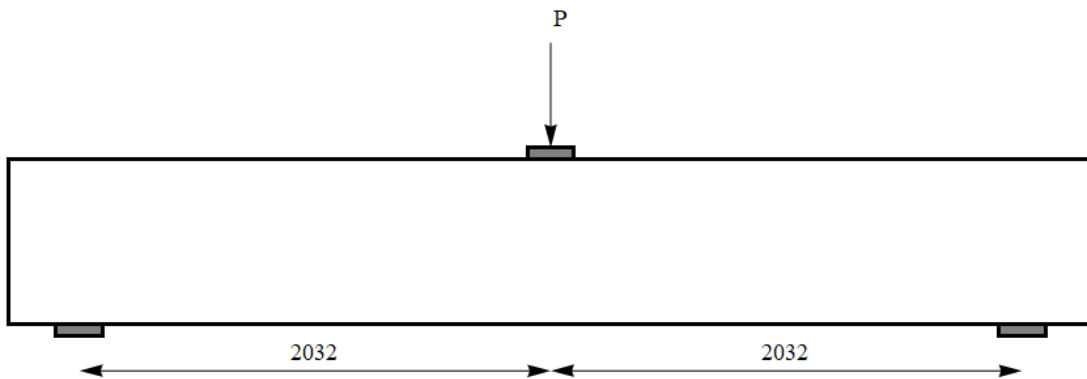
Fig. 20 Beam test setup for simply supported rectangular beam [80].

For the finite element model, we consider two, four and six beam elements, and the material model is rescaled by equation (69). The 30 mm displacement at a midspan is applied in 100 steps, and the results are shown in Figure 21. It can be seen that without rescaling or with the

classical rescaling proportional to the characteristic element size, the results are highly sensitive to the mesh size. On the hand, with the proposed rescaling, practically no mesh sensitivity is observed and the numerical simulations results (tagged as HC^2) are in good agreement with the experimental results. Figure 5 also depicts the failure load based on the ACI-318 code [2], which shows a reasonable agreement with the experimental results.
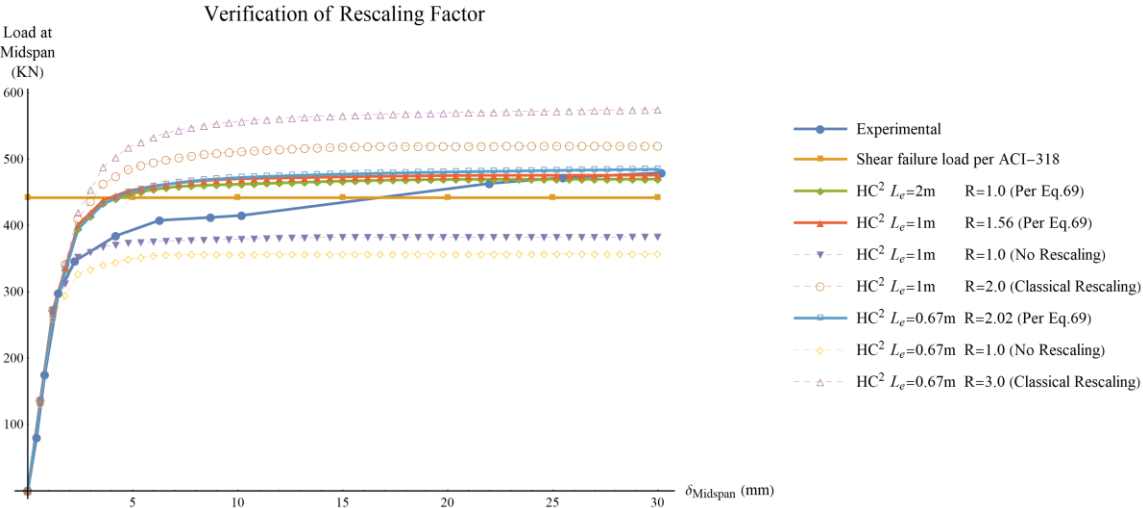
Fig. 21 Mesh sensitivity studies and comparison to ACI-318 code and experimental results [80].

5.6 Shear Test on TxDOT Type A Beam.

We consider a simply supported I beam, a cross section known as the Texas Department of Transportation (TxDOT) A beam, tested at the University of Houston by Laskar et. al. [81]. The beam is simply supported with a span of 7.32 m and a depth of 713 mm as shown in Figure 22. The beam is reinforced with twelve 12.7 mm straight prestressing strands with an ultimate strength of 1862 MPa. The beam is reinforced with four No. 5 rebars on the top and stirrups No. 2 at with 0.25 m spacing. The reinforcing steel has a yield strength of 410 MPa and the concrete has a strength of 71MPa. The concrete is modeled using isotropic damage model [10] with material parameters listed in Table A.2.
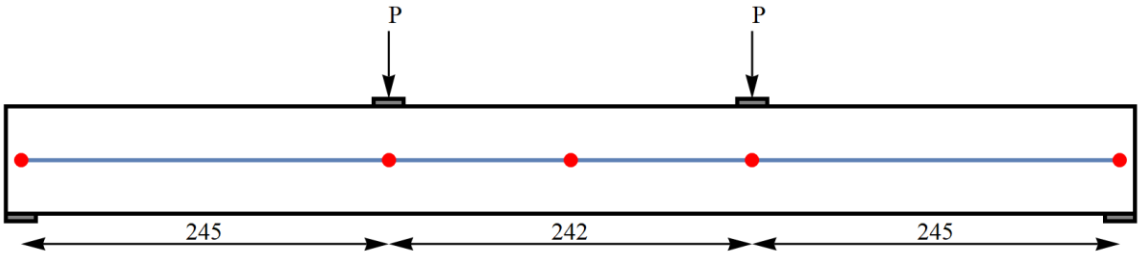
Fig. 22 Experimental setup and finite element model for the TxDOT A beam. Beam elements are shown in the center of the beam [81].

The analysis was performed using 4 coarse-scale elements with the interior nodes located under loads and at a midspan. The prescribed displacement of 35 mm was applied over 50

load increments at the points of load application. The multiscale (HC^2) simulation was compared in Figure 23 with the experimental results [81] and the ACI-318 code [2]. It can be seen that the multiscale beam accurately predicts the failure load and the overall behavior of the beam, whereas the ACI-318 underestimates the capacity by more than 25%.
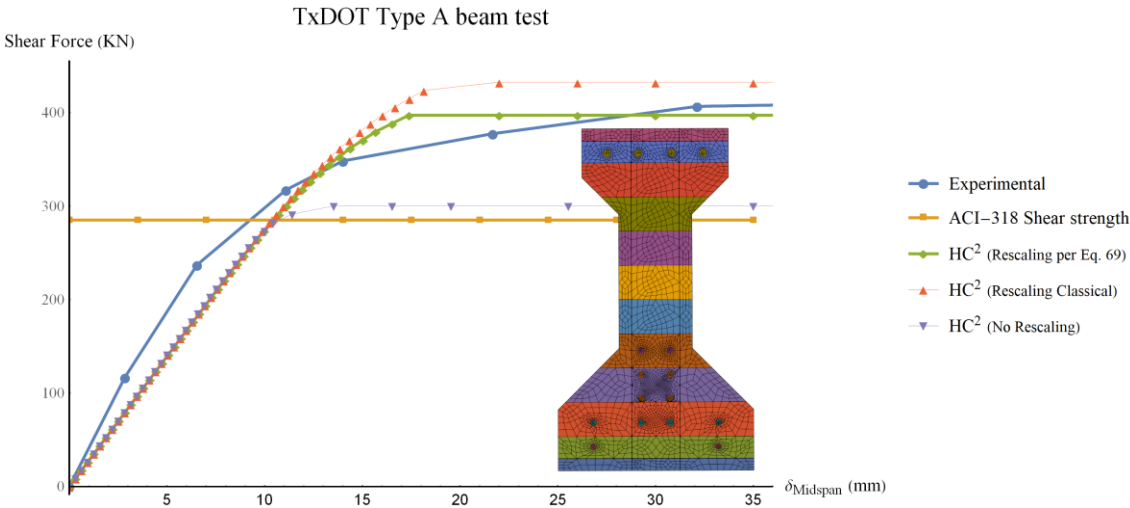
Fig. 23 TxDOT Type A beam. Comparison of RC2, ACI-318 code and experimental results. Also simulation results with no rescaling and with classical rescaling are show [81].

5.7 Continuous Posttensioned Beam.

A continuos posttensioned beam was tested at the RWTH Aachen University by Herbrand et. al [82]. The beam has a rectangular cross section of a depth of 800 mm and a width of 250

mm. The beam has two tendons with a parabolic profile as shown in Figure 24. Each prestressing tendon is made up of three 0.6" strands with an ultimate load of 1950 MPa. The beam is reinforced with six rebars 25 mm in diameter at the top and bottom; stirrups are 10 mm in diameter spaced at 0.25 m; the yield stress for the rebars is 557 MPa for the longitudinal rebars and 520 for the stirrups. The concrete constitutive material parameters are listed in Table A.2. The experimental setup is shown in Figure 8.
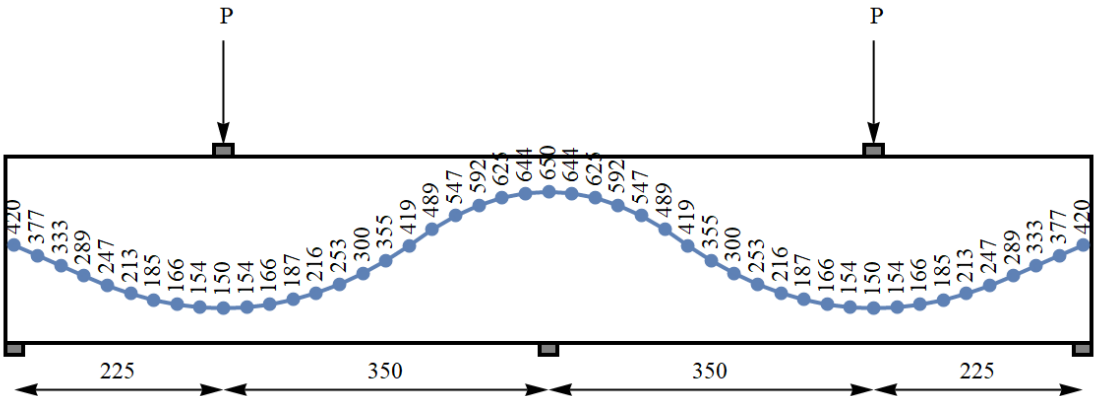
Fig. 24 Experimental setup for continuous posttensioned beam [82].

The analysis was performed using four coarse-scale elements, a displacement under the loads was applied in 100 steps. Figure 25 depicts the load-deflection curves obtained by the multiscale beam formulation and the ACI-318 code both of which are in good agreement with the experimental results.
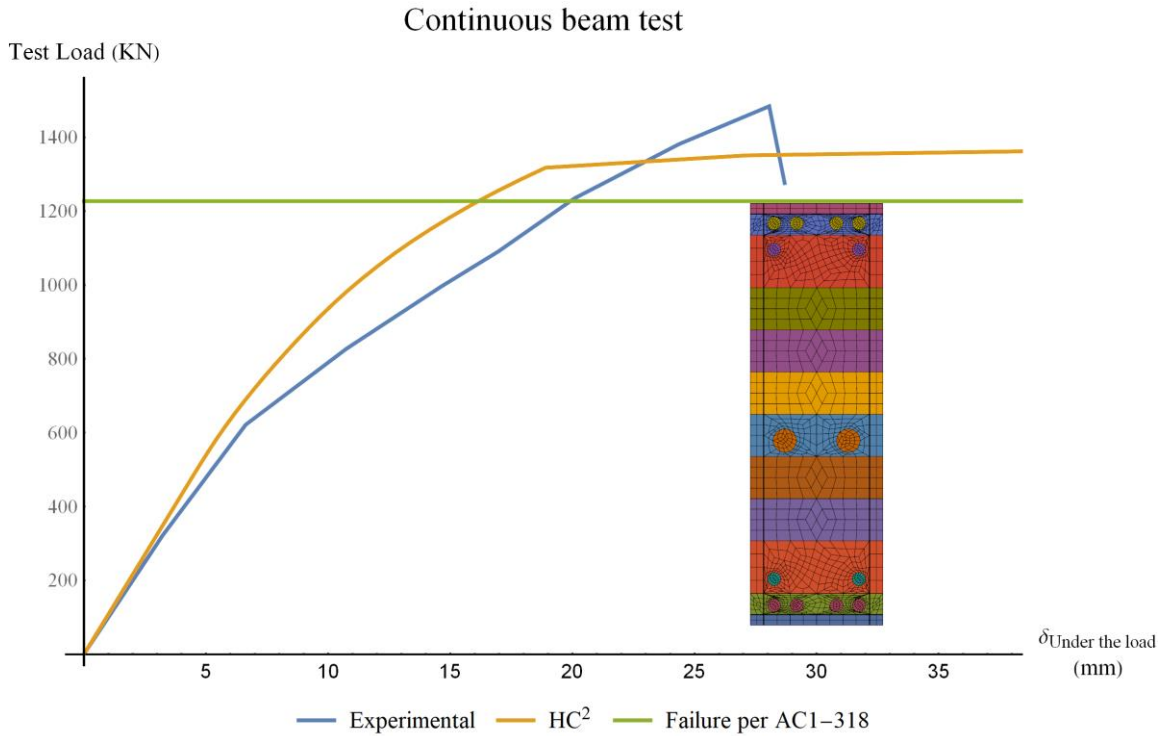
Fig. 25 Continuous posttensioned beam. Comparison of HC^2, ACI-318 code and experimental results [82].

5.8 Verification of Nonlocal Quadrature Scheme for Plates.

Herein, we investigate the nonlocal quadrature scheme for problems where the size of the RVE is comparable to the coarse-scale element size. As a test problem, we consider a 3.0 m by 3.0 m simply supported waffle slab subjected to a localized load at the center. The direct numerical simulation (DNS) consisting of 54,144 elements, as shown in Figure 26, is employed as a reference solution to estimate deflection error at the center of the plate. The

waffle slab has a rib spacing of 0.50 m., a web thickness of 0.10 m., a total depth of 0.10 m and a flange depth of 0.05 m. The RVE is shown in Figure 27. The deflection error predicted by O(1) homogenization and the higher order computational continua (HC^2) are shown in Figure 28 for different values of Θ', which is defined as the ratio of twice the RVE size to the coarse-scale element size. Plate models on the right of Figure 28, depict the waffle slab (in black), coarse-scale mesh (in blue), and finite element nodes (in red) for the 2 by 2, 4 by 4 and 6 by 6 meshes.
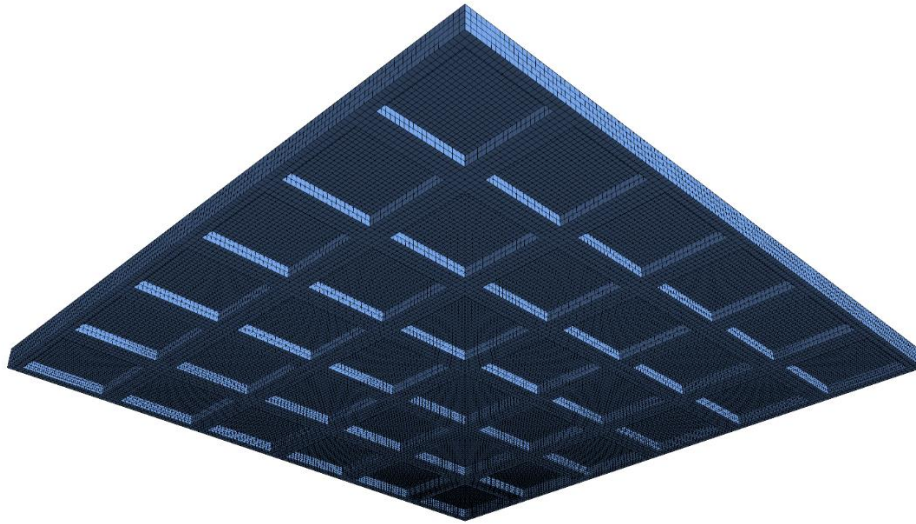
Fig. 26 Isometric view of the DNS model for the waffle slab consisting of 54,144 elements
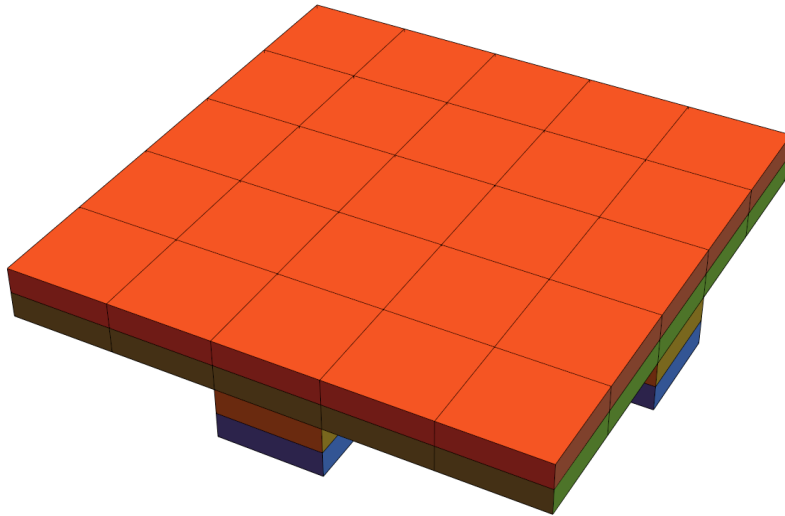
Fig. 27 The RVE of the waffle slab consisting of four concrete partitions

It can be seen from Figure 28 that as Θ' approaches zero, the nonlocal and Gauss quadrature points coincide giving rise to the same HC^2 solution, whereas when the RVE size approaches the coarse-scale element size, HC^2 with nonlocal quadrature points performs better than with Gauss quadrature points. Note that the O(1) formulation is essentially assumes a solid plate with a concrete and steel microstructure in Figure 3 being infinitesimal, which non-surprisingly produces very stiff response.
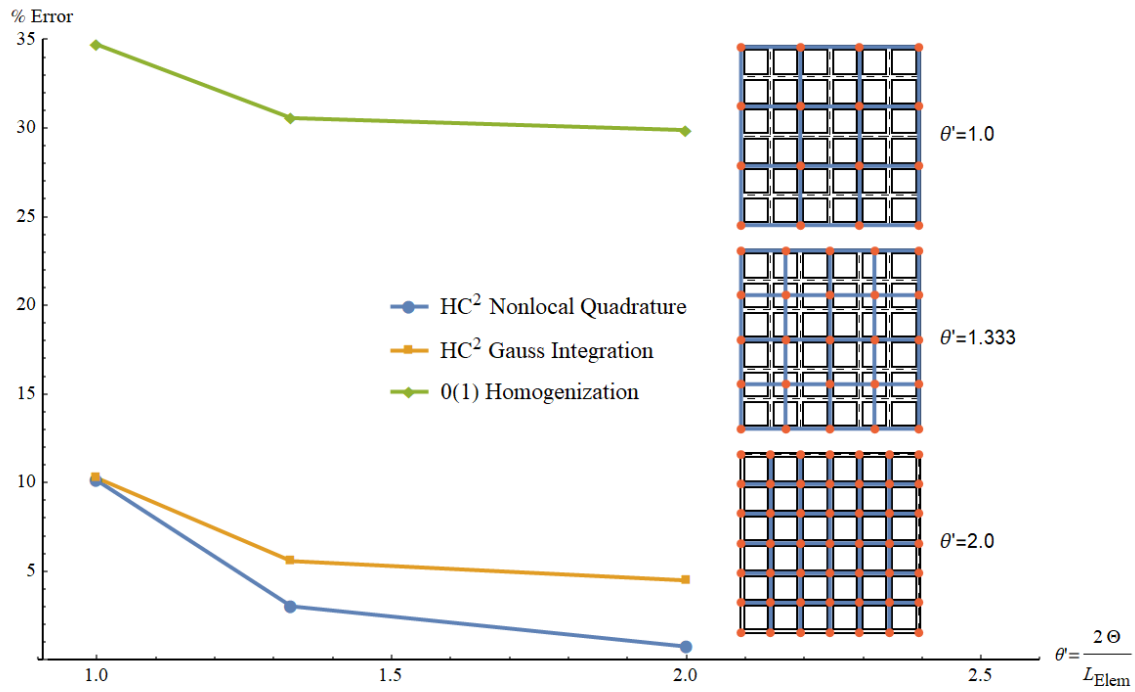
Fig. 28 Center deflection error (%) versus RVE size ratio as obtained using O(1)

homogenization and HC^2 formulation.

5.9 Validation of Rescaling Procedure for Solid Slab.

Consider a simply supported square solid slab with a concentrated load at the center, which

has been tested by Abdul-Wahab and Khalil [83]. The slab has in-plane dimensions of 1.5 m.

by 1.5 m. and depth of 0.075 m. It is reinforced with 8 mm bars spaced at 0.167 m in both

directions and placed at 0.08 mm from the bottom of the slab. The constitutive model parameters are listed in Table A.3.

The load is applied over one hundred increments. The deflection obtained for two different meshes at the center of the slab are compared to the test results in Figure 29. It can be seen that the simulation results of the load versus center deflection, are in good agreement with the experimental results for different mesh sizes and corresponding rescaling ratio.
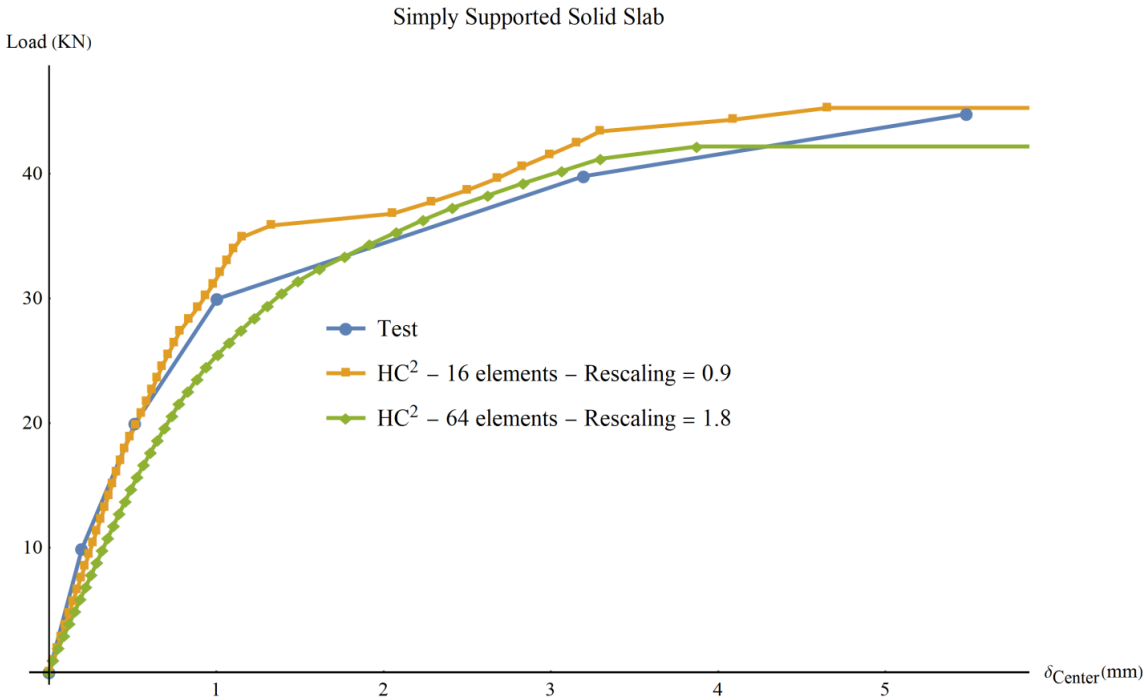
Fig. 29 Load versus deflection for a solid slab using different meshes and rescaling ratios.

5.10 Validation for a Hollowcore Prestressed Slab.

Consider a precast hollowcore slab fabricated using an extruder or slip former that creates a periodic hollow pattern. The hollowcore is a one-way slab system with prestressed reinforcement only in the direction of the bending span, other than that it has no transverse or vertical reinforcement. Since the reinforcement is in one direction only it has a brittle behavior in the transverse direction and its capacity is sensitive to the concentrated loads acting on the slab. Current design provisions use empirical methods for the distribution of the concentrated loads.

The slab tested by Buettner & Becker [84] has a span of 6.0 m, 9.0 m width, and 0.20 m depth; it is manufactured in panels of 1.20 m width. Each hollowcore slab is reinforced with 10 prestressing strands of 9 mm in diameter with an ultimate strand strength of 1,724 MPa, and initial prestressing force of 65% the ultimate strength, made of concrete with a compressive strength of 34.4 MPa. Figure 30 depicts the sketch of the test setup.
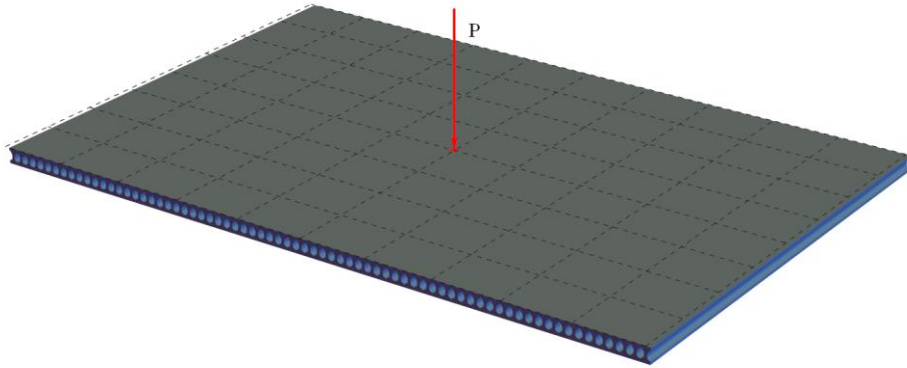
Fig. 30 Test setup for the hollowcore slab [84].

The constitutive model parameters are listed in Table A.3. The rescaling factor for the mesh shown in Figure 6 is 0.48. Figure 7 shows the results of the numerical simulation, which are in good agreement with experiments for both the center deflection and the ultimate load capacity. The RVE employed in the HC^2 simulations is also shown in Figure 31.
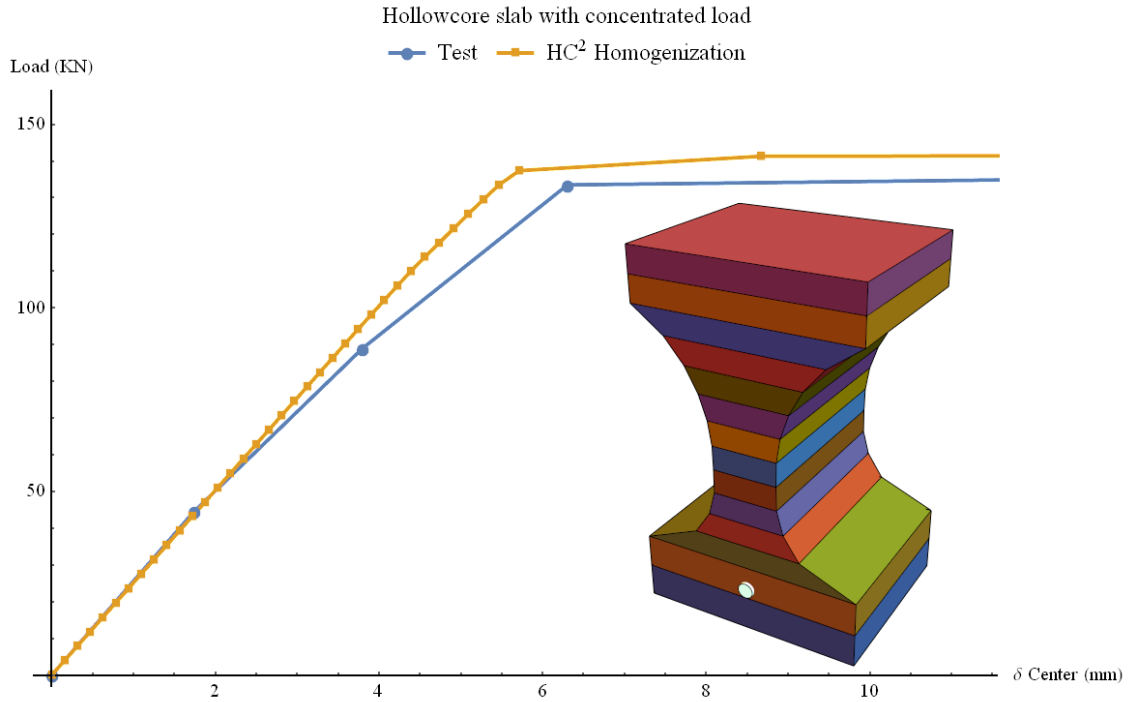
Fig. 31 Load versus deflection for a hollowcore prestressed slab [84].

5.11 Validation for a Waffle Slab.

Consider a simply supported 1.5m by 1.5m waffle slab tested by Abdul-Wahab and Khalil [83]. The load is applied at the center on a square steel plate with a side length of 0.3m. The slab is reinforced with steel rebars of 8 mm in diameter. The cross-section dimensions of the RVE for the waffle slab are shown in Figure 32. The constitutive model parameters are summarized in Table A.3.
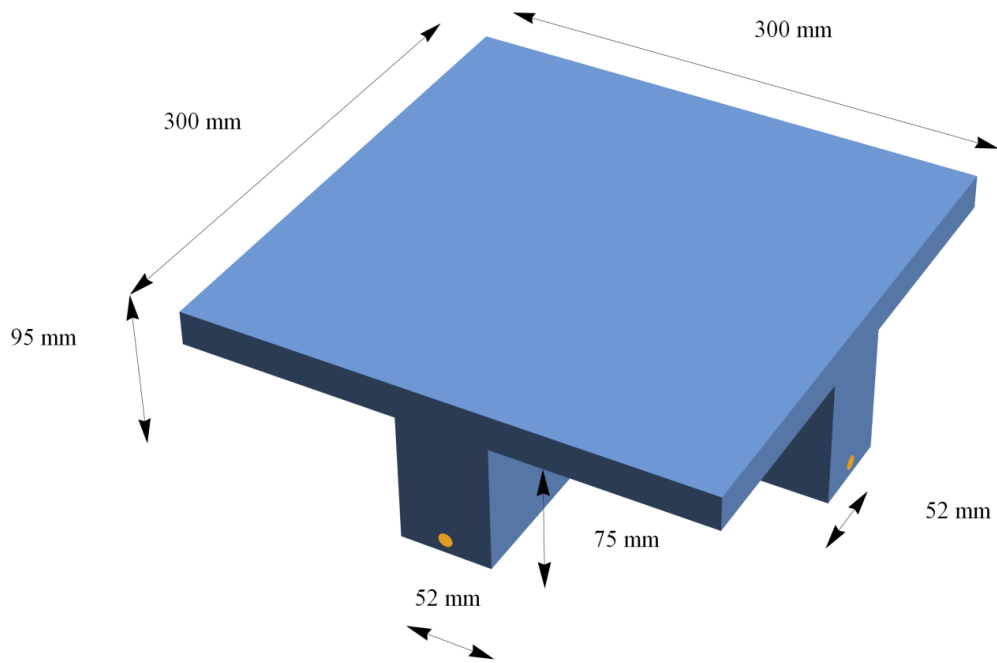
Fig. 32 Dimensions of the waffle slab [83].

The results of the center displacement versus load are shown in Figure 33. Good agreement can be observed between the HC^2 simulation and the experimental results.
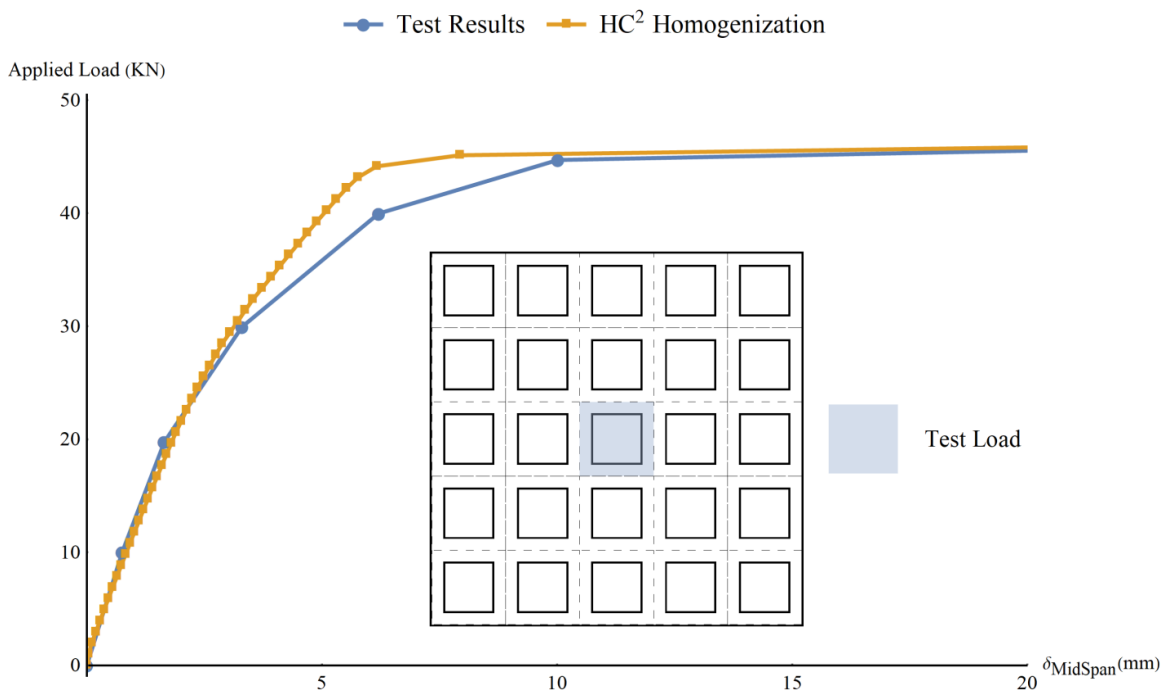
Fig. 33 Load versus deflection for a waffle slab [83].

This page intentionally left blank.

Chapter 6

Conclusions

A computationally efficient, accurate and versatile multiscale approach for the analysis of beams and concrete slabs has been developed. The accuracy stems from the higher order computational continua (HC^2) formulation that enables consideration of large representative volume elements (RVE) characteristic to beams, waffle and hollowcore slabs without significant deterioration in solution accuracy. The striking accuracy of the formulation for beams and plates of various geometries is truly remarkable.

The computational efficiency is a direct consequence of model reduction where certain fine-scale information (matrices $\bar{\mathbf{L}}, \bar{\mathbf{Z}}^{(\Phi)}$ and $\bar{\mathbf{A}}^{(\Phi)}$) is precomputed prior to nonlinear analysis. For the numerical examples considered herein, at each plate nonlocal quadrature point where damage evolves, it necessary to solve 24 to 30 nonlinear equations (with the same number of unknowns). While in comparison to the phenomenological reinforced concrete model there is an added cost in solving 24 or 30 nonlinear equations at each nonlocal quadrature point

where damage takes place, it is a small fraction of the computational cost of the three-dimensional finite element analysis.

The proposed HC^2 for the multiscale beam and plate elements is capable of capturing flexural, shear and torsion modes of failure. Prestressing tendons with variable eccentricity are accommodated by the formulation and consideration of effects due to creep and shrinkage are accounted for, combined with a well-established simple damage law rescaling that has been shown to yield nearly mesh-size independent simulation results.

Future research will focus on:

a) Validation of HC^2 multiscale beam and plate subjected to dynamic loadings, extension to shear walls and moment resisting frames for seismic applications;

b) Inclusion of bond-slippage effects in the concrete and rebar or strand; and

c) Consideration of the three-scale formalism accounting for concrete microstructure consisting of mortar and aggregate phases.

Bibliography

[1] Miller S.A., Horvarth A., Monteiro P.J.M. (2018) Impacts of booming concrete production on water resources worldwide, Nature Sustainability, 1(1):69-76.

[2] American Concrete Institute (2014) Building code requirements for structural concrete ACI-318.

[3] American Association of State Highway and Transportation Officials (2014), AASHTO LRFD bridge design specifications.

[4] Emery JM, Hochhalther JD, Ingraffea AR (2007) Computational fracture mechanics of concrete structures: A retrospective through multiple lenses, FraMCos-6 Catania (Italy).

[5] Bazant Z, Caner F, Carol I, Adley M, Akers S (2000) Microplane model M4 for concrete. I: Formulation with work-conjugate deviatoric stress, Journal of Engineering Mechanics ASCE, 126(9).

[6] Lilliu G, van Mier JGM (2003) 3D lattice type fracture model for concrete, Engineering Fracture Mechanics, 70:927-941.

[7] Fillipou FC, Spacone E, Taucer FF (1991), A fiber beam-column element for seismic response analysis of reinforced concrete structures, Report No. UCB/EERC-91/17, Earthquake Engineering Research Center, College of Engineering, University of California, Berkeley.

[8] Mohr S, Bairán J, Marí A (2010), A frame element model for the analysis of reinforced concrete structures under shear and bending, Engineering Structures 32: 3936-3954.

[9] Willam KJ, Warnke EP (1974), Constitutive model for the triaxial behavior of concrete, IABSE reports on the working commissions, http://dx.doi.org/10.5169/seals-17526.

[10] Pijaudier-Cabot G and Mazars J (2001) Damage Models for Concrete, in Handbook of Materials Behavior, J. LeMaitre, Ed., San Diego, CA: Academic Press, pp. 500-512.

[11] Lee J, Fenves GL (1998), Plastic-damage model for cyclic loading, Journal of Engineering Mechanics, 124: 892-900.

[12] Grassl, P., Xenos, D., Nystrom, U., Rempling, R. and Gylltoft, K. (2013), CDPM2: A damage-plasticity approach to modelling the failure of concrete, International Journal of Solids and Structures, 50(24):3805-3816.

[13] Cervenka J and Cervenka V (2008), Three dimensional combined fracture-plastic material model for concrete including creep and rate effect for dynamic loading, International Journal of Plasiticy, 24(12): 2192-2220.

[14] Moharrani M, Koutromanos I (2016) Triaxial constitutive model for concrete under cyclic loading. Journal of Structural Engineering 142 (7).

[15] Maekawa K, Ishida T, Kishi T (2003) Multi-scale modeling of concrete performance, Journal of Advanced Concrete Technology, 1(2): 91-126.

[16] Oliver J, Caicedo M, Roubin E, Hernández JA (2014) Multi-scale (FE^2) analysis of material failure in cement/aggregate-type composite structures, Computational Modelling of Concrete Structures, Taylor & Francis Group.

[17] Caballero A, López CM, Carol I (2006) 3D meso-structural analysis of concrete specimens under uniaxial tension, Comput. Methods Appl. Mech. Engrg. 195:7182-7195.

[18] Zhang JL, Liu X, Yuan Y, Mang HA (2014) A multiscale model for predicting the elasticity modulus and the strength of ultra-high performance fiber reinforced concrete, Computational Modeling of Concrete Structures, Taylor & Francis Group.

[19] Rumanus E., Meschke G. (2010) Homogenization-based model for reinforced concrete, Computational modeling of concrete structures, Taylor & Francis Group, London.

[20] Mori T, Tanaka K (1973) Average stress in matrix and average elastic energy of materials with misfitting inclusions, Acta Metallurgica 21.

[21] Wu W, Yuan Z, Fish J (2010) Eigendeformation-based homogenization of concrete, International Journal for Multiscale Computational Engineering 8(1):1-15.

[22] Zohdi TI, Wriggers P (2005) Introduction to computational micromechanics. Springer, Berlin.

[23] Fish J., Filonova V., Fafalis D. (2015) Computational continua revisited, International Journal for Numerical Methods in Engineering, 102:332-378.

[24] Fish J (2014) Practical multiscaling, John Wiley & Sons.

[25] Fish J, Filonova V, Yuan Z (2012) Reduced order computational continua, Comput. Methods Appl. Mech. Engrg. 221-222: 104-116.

[26] Fish J, Shek K, Pandheeradi, Shephard MS (1997) Computational plasticity for composite structures based on mathematical homogenization: theory and practice, Computer Methods in Applied Mechanics and Engineering 148 (1-2):53-73.

[27] Oskay C, Fish J (2007) Eigendeformation-based reduced order homogenization for failure analysis of heterogeneous materials, Computer Methods in Applied Mechanics and Engineering 196(7):1216-1243.

[28] Oskay C, Fish J (2008) On calibration and validation of eigendeformation-based multiscale models for failure analysis of heterogeneous systems, Computational Mechanics 42 (2):181-195.

[29] Sparks P, Oskay C (2016) The method of failure paths for reduced-order computational homogenization, International Journal for Multiscale Computational Engineering 14 (5).

[30] Zhang X, Oskay C (2015) Eigenstrain based reduced order homogenization for polycrystalline materials, Computer Methods in Applied Mechanics and Engineering 297: 408-436.

[31] Fish J, Kuznetzov S (2010) Computational Continua, International Journal for Numerical Methods in Engineering, 84:774-802.

[32] Fafalis D., Fish J. (2018) Computational continua for linear elastic heterogeneous solids on unstructured finite element meshes, International Journal for Numerical Methods in Engineering 115 (4): 501-530.

[33] Hughes TJR., Feijoo GR., Mazzei L., Quincy J.B. (1998) The variational multiscale method-a paradigm for computational mechanics. Computer Methods in Applied Mechanics and Engineering 166:3-24.

[34] Fish J (1992) The S-version of the finite element method, Computers & Structures, 43(3): 539-547.

[35] Cuellar JR, Gallegos S (2004) Un modelo de filamentos para vigas-columnas de concreto, III Congreso Internacional sobre Métodos Numéricos en Ingeniería y Ciencias Aplicadas, Barcelona.

[36] Aalami BO (2000) Structural modeling of posttensioned members. J. Struct. Eng. 126(2):157-162.

[37] Ayoub A, Filippou FC (2010) Finite-element model for pretensioned prestressed concrete girders. Journal of Structural Engineering. 136(4):401-409.

[38] Ayoub A, (2011) Nonlinear finite-element analysis of posttensioned concrete bridge girders. Journal of Bridge Engineering. 16(3):479-489.

[39] Bazant, ZP., Pijaudier-Cabot, G. (1989) Measurement of characteristic length of nonlocal continuum. Journal of Engineering Mechanics 115(4): 755-767.

[40] Oliver J (1989) A consistent characteristic length for smeared cracking models. International Journal for Numerical Methods in Engineering. 28:461-474.

[41] Liu Y., Filonova V., Hu, N., Yuan Z., Fish J., Yuan Z., Belytschko, T. (2014) A regularized phenomenological multiscale damage model, International Journal for Numerical Methods in Engineering, 99:867-887.

[42] Filonova V., Fish J. (2016) Computational continua for thick elastic layered structures, International Journal for Multiscale Computational Engineering, doi: 10.1615/Int.JMultCompEng.2016017568.

[43] Reddy JN (1990) A general non-linear third-order theory of plates with moderate thickness, Int. J. Non-Linear Mechanics, 25(6): 677-686.

[44] Reddy JN (1997) On locking-free shear deformable beam finite elements, Comput. Methods Apps. Mech. Engrg. 149:113-132.

[45] Lin TY (1963) Load-balancing methods for design and analysis of prestressed concrete. Journal of the American Concrete Institute. 60(6):719-742.

[46] Nilson AH (1987) Design of prestressed concrete. John Wiley & Sons, Inc. ISBN 987-0-471-83072-6.

[47] Zia P, Preston HK, Scott NL, Workman EB (1979) Estimating prestress losses. Concrete international 6:32-38.

[48] Bazant ZP, (1998) Mathematical modeling of creep and shrinkage of concrete. John Wiley & Sons Ltd.

[49] International Federation for Structural Concrete fib CEB-FIP (2010) fib Model Code for Concrete Structures, ISBN: 978-3-433-03061-5.

[50] Belytschko T, Fish J, Engelmann B (1988) Computer Methods in Applied Mechanics and Engineering 70:59-89.

[51] Cervera, M. (2008) A smeared-embedded mesh-corrected damage model for tensile cracking. International Journal for Numerical Methods in Engineering. 76:1930-1954.

[52] Hand F.R., Pecknold D.A., Schnobrich, W.C. (1972) A layered finite element nonlinear analysis of reinforced concrete plates and shells, Civil Engineering Studies, Structural research series No. 389, University of Illinois.

[53] Lackner R., Mang H. (2003) Scale transition in steel-concrete interaction. I: Model. Journal of engineering mechanics, 129 (4):393-402.

[54] Cervera M., Hinton E., Hassan O. (1987) Nonlinear analysis of reinforced concrete plate and shell structures using 20-noded isoparametric brick elements, Computers & Structures, 25(6):845-869.

[55] Hrynyk T.D., Vecchio F.J. (2015) Capturing out-of-plane shear failures in the analysis of reinforced concrete shells, Journal of Structural Engineering, 141(12):04015058.

[56] Luu C.H., Mo Y.L., Hsu T.T.C. (2017) Development of CSMM-based shell element for reinforced concrete structures, Engineering Structures, 132:778-790.

[57] Sherburn J.A., Roth M.J., Chen J.S., Hillman M. (2015) Meshfree modeling of concrete slab perforation using a reproducing kernel particle impact and penetration formulation. International Journal of Impact Engineering 86:96-110.

[58] Roth M.J., Chen J.S., Slawson T.R., Boone R.N., Ren X., Chi S.W., Lee C.H., Guan P.C. (2011) Multiscale RKPM formulation for modeling penetration of an ultra-high-strength concrete material. Proceeding, Third International Conference on Computational Methods in Structural Dynamics and Earthquake Engineering, COMPDYN 2011; Corfu; Greece.

[59] Williams T.O. (2008) A new theoretical framework for the formulation of general, nonlinear, multiscale plate theories, International Journal of Solids and Structures, 45:2534-2560.

[60] Framby J., Brouzoulis J., Fagerstrom M., Larsson R. (2014) A fully coupled multiscale shell formulation for the modelling of fibre reinforced laminates, ECCM-16th European Conference on Composite Materials, Seville, Spain.

[61] Wagner W., Gruttmann F. (2016), An adaptive strategy for the multi-scale analysis of plate and shell structures with elasto-plastic material behaviour, Technische Mechanik, 36(1-2):142-154.

[62] Wimmer J., Stier B., Simon J.W., Reese S. (2016) Computational Homogenization from a 3D finite element model of asphalt concrete—linear elastic computations. Finite Elements in Analysis and Design, 110:43-57.

[63] Gal E., Kryvoruk R. (2011) Fiber reinforced concrete properties - A multiscale approach, Computers and Concrete, 8(5):525-539.

[64] Sherzer G. L., Schlangen E., Ye G., Gal E. (2018). Multi-scale modelling of the mechanics of concrete based on the cement paste properties. Computational Modeling of Concrete Structures, Meschke, Pichler and Rods, eds, Taylor & Francis Group, London, ISBN 978-1-138-74117-1.

[65] Oskay C., Pal G. (2010) A multiscale failure model for analysis of thin heterogeneous plates, International Journal of Damage Mechanics, 19(5):575-610.

[66] Oskay, C. (2009) Two-level multiscale enrichment methodology for modeling of heterogeneous plates. International Journal for Numerical Methods in Engineering 80 (9):1143-1170.

[67] Fish J., Yuan Z. (2005) Multiscale enrichment based on partition of unity. International Journal for Numerical Methods in Engineering, 62(10):1341–1359.

[68] Hackl K., Kochmann D.M. (2011) An incremental strategy for modeling laminate microstructures in finite plasticity–energy reduction, laminate orientation and cyclic behavior. Multiscale Methods in Computational Mechanics, in R. de Borst and E. Ramm (eds.), Multiscale Methods in Computational Mechanics, Lecture Notes in Applied and Computational Mechanics 55, Springer Science-Business Media B.V. , DOI 10.1007/978-90-481-9809-2-7, pp.117-134.

[69] Klinge S., Hackl K. (2016) Application of the Multiscale FEM to the Determination of Macroscopic Deformations Caused by Dissolution Precipitation Creep. International Journal for Multiscale Computational Engineering, 14 (2):1-23.

[70] Radermacher A., Bednarcyk B.A., Stier B., Simon J., Zhou L., Reese S. (2016) Displacement-based multiscale modeling of fiber-reinforced composites by means of proper orthogonal decomposition. Advanced Modeling and Simulation in Engineering Sciences, 3:29.

[71] Simon J.W., Stier B., Reese S. (2013) Multiscale Modeling of Layered Fiber Composites Accounting for Delamination. 8th German-Greek-Polish Symposium on Recent Advances in Mechanics, Goslar, Germany, pp. 71-72.

[72] Moyeda, A., Fish, J. (2017) Towards practical multiscale approach for analysis of reinforced concrete structures, Computational Mechanics, https://doi.org/10.1007/s00466-017-1521-1.

[73] Moyeda, A., Fish, J. (2018) Multiscale analysis of prestressed concrete structures, International Journal for Multiscale Computational Engineering, 16(3):285-301.

[74] Bicanic N., Mang H., Meschke G., De Borst R. (2014) Computational modelling of concrete structures, CRC Press, ISBN 9781138001459 - CAT# K22688.

[75] Averill R.C. and Reddy JN (1992) An assessment of four-noded plate finite elements based on generalized third-order theory, International Journal for Numerical Methods in Engineering, 33: 1553-1572.

[76] Reddy JN (2002) Energy principles and variational methods in applied mechanics, 2nd Edition, John Wiley & Sons.

[77] Bazant ZP., Oh BH. (1983) Crack band theory for concrete, Materials and Structures, 16:155-177.

[78] Leonhardt F, Walther R (1962) Contribution to the treatment of shear in reinforced concrete, Technical Translation 1172, National Research Council of Canada.

[79] Bresler B, Scordelis AC (1963) Shear strength of reinforced concrete beams title no. 60-4, Journal of the American Concrete Institute, 60(1).

[80] Saqan E, Frosch R. (2009) Influence of flexural reinforcement on shear strength of prestressed concrete beams. ACI Structural Journal. 106(1):60-68.

[81] Laskar A, Hsu T, Mo YL (2010) Shear strengths of prestressed concrete beams part 1: Experiments and design. ACI Structural Jounal. 107(3).

[82] Herbrand M, Kueres D, Classen M, and Hegger J (2018), Experimental investigations on the shear capacity of prestressed concrete continuous beams with rectangular and i-shaped

cross-sections. Springer International Publishing, High Tech Concrete: Where Technology and Engineering Meet DOI 10.1007/978-3-3-319-59471-2_78.

[83] Abdul-Wahab H.M.S. and Khalil M.H. (2000) Rigidity and strength of orthotropic reinforced concrete waffle slabs, Journal of Structural Engineering 126(2):219-227.

[84] D.R. Buettner, Becker R.J. (1980) Concentrated loads on Spancrete assemblies, Final Report to the Spancrete Manufacturers Association.

[85] Fish J, Belytschko T. (2007) A first course in finite elements, John Wiley & Sons.

[86] Helyger P.R. , Reddy J.N. (1988) A higher order beam finite element for bending and vibration problems, Journal of Sound and Vibration 126(2):309-326.

Appendix A – Material Properties for Examples.

		Units	Leonhardt Shear Beam 5.3	Beam with Stirrups 5.4
Concrete Properties	Compressive Strength	MPa	28.5	35.0
	Modulus of Elasticity	MPa	25,200	27,600
	Tensile Strength	MPa	1.3	4.4
	At		1.2	1.0
	Bt		25,000	9,800
	Ac		1.5	1.4
	Bc		2,400	1,800
Steel Properties	Modulus of Elasticity	MPa	208,000	200,000
	Yield Stress Longitudinal Bars	MPa	560	552
	Yield Stress Stirrups	MPa	N.A.	325

Table A.1. Material parameters of concrete and steel used in numerical examples 5.3 and 5.4

		Units	Verification of Rescaling Approach 5.5	Shear Test on TxDOT Type A Beam 5.6	Continuous Posttensioned Beam 5.7
Concrete Properties	Compressive Strength	MPa	52.1	71.0	51.0
	Modulus of Elasticity	MPa	30,411	41,700	25,824
	Tensile Strength	MPa	3.0	5.8	5.4
	At		2.0	1.5	1.1
	Bt		21,000	21,000	15,000
	Ac		1.6	1.9	2.2
	Bc		1,600	1,500	1,500
Steel Properties	Modulus of Elasticity	MPa	200,000	200,000	200,000
	Yield Stress Longitudinal Bars	MPa	N.A.	410	557
	Yield Stress Stirrups	MPa	N.A.	410	520
	Yield Stress Prestress	MPa	1,676	1,676	1,729

Table A.2. Material parameters of concrete and steel used in numerical examples 5.5 thru 5.7

		Units	Validation of Rescaling for Solid slab 5.9	Validation for a Hollowcore Prestressed Slab 5.10	Validation for a Waffle Slab 5.11
Concrete Properties	Compressive Strength	MPa	36.0	34.4	28.9
	Modulus of Elasticity	MPa	28,400	27,700	25,500
	Tensile Strength	MPa	3.3	2.9	2.8
	Fracture Energy	N/mm	0.144	0.143	0.140
	Characteristic Size	mm	338	391	390
	At		1.0	1.0	1.0
	Bt		20,000	20,000	20,000
	Ac		1.1	1.1	1.1
	Bc		1,300	1,400	1,400
Steel Properties	Modulus of Elasticity	MPa	200,000	200,000	200,000
	Yield Stress Longitudinal Bars	MPa	398	N.A.	398
	Yield Stress Prestress	MPa	N.A.	1,552	N.A.

Table A.3. Material parameters of concrete and steel used in numerical examples 5.9 thru 5.11

This page intentionally left blank.

Appendix B – Derivation of Beam Stiffness Matrix using the Constitutive Tensor.

The stiffness matrix for three different types of beam will be obtained for a homogeneous isotropic beam, using the shape functions that accurate describe the 2D or 3D displacement field and the constitutive material tensor. The results are shown to be identical to those obtained from the classical solutions derived using the beam cross sectional properties (i.e. area and inertia).

B.1 Two Node Euler-Bernoulli 2D Beam

The displacement of the Euler-Bernoulli beam is given as:

$$u = -z \frac{\partial w}{\partial x} \tag{117}$$

$$w = w_0 \tag{118}$$

Using a 2 node beam with degrees of freedom w^i and $\dfrac{\partial w^i}{\partial x}$ on each node, the matrix form of

the discretized displacements is expressed as:

$$\begin{Bmatrix} u \\ v \end{Bmatrix} = \mathbf{N} \begin{Bmatrix} w^1 & \dfrac{\partial w^1}{\partial x} & w^2 & \dfrac{\partial w^2}{\partial x} \end{Bmatrix}^T \tag{119}$$
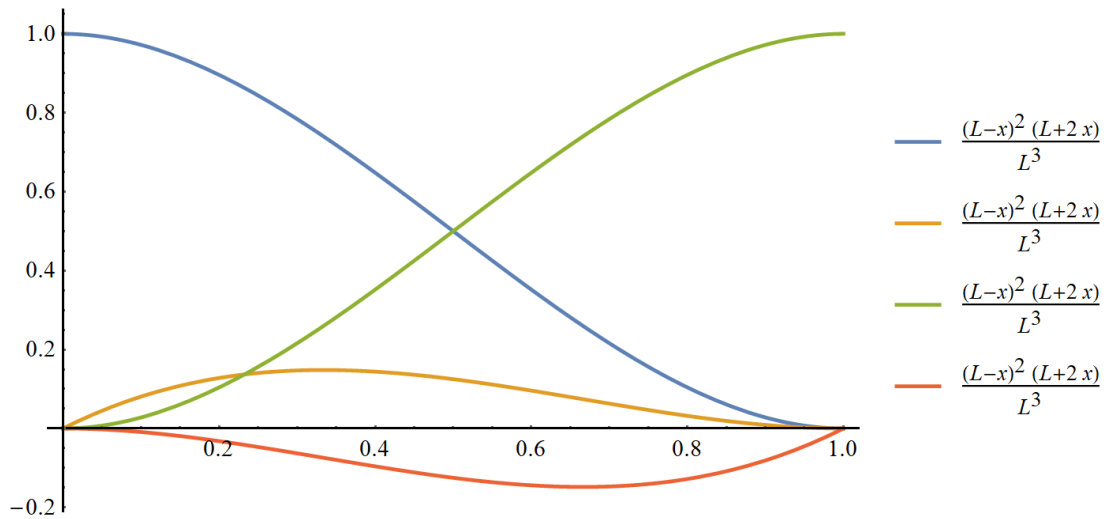
Fig. 34 Hermitian shape functions for beams.

Using the Hermitian interpolation functions, and the displacement field in (117) and (118) the full field shape functions are:

$$\mathbf{N} = \left\{ \begin{matrix} \dfrac{6(L-x)xz}{L^3} & -\dfrac{(L-3x)(L-x)z}{L^2} & \dfrac{6x(-L+x)z}{L^3} & \dfrac{(2L-3x)xz}{L^2} \\ \dfrac{(L-x)^2(L+2x)}{L^3} & \dfrac{(L-x)^2 x}{L^2} & \dfrac{(3L-2x)x^2}{L^3} & \dfrac{x^2(-L+x)}{L^2} \end{matrix} \right\} \qquad (120)$$

The strain displacement matrix for a 2D beam is given by:

$$\mathbf{B} = \nabla \mathbf{N} = \begin{bmatrix} \dfrac{\partial \mathbf{N}_x}{\partial x} \\ \dfrac{\partial \mathbf{N}_x}{\partial z} + \dfrac{\partial \mathbf{N}_z}{\partial x} \end{bmatrix} \qquad (121)$$

Inserting the expression in (120) into (121) the strain displacement matrix is expressed as:

$$\mathbf{B} = \left\{ \begin{matrix} \dfrac{6(L-2x)z}{L^3} & \dfrac{4Lz-6xz}{L^2} & -\dfrac{6(L-2x)z}{L^3} & \dfrac{2(L-3x)z}{L^2} \\ 0 & 0 & 0 & 0 \end{matrix} \right\} \qquad (122)$$

The stiffness matrix **K** is evaluated as:

$$\mathbf{K} = \int_\Omega \mathbf{B}^T \mathbf{L} \mathbf{B} d\Omega \qquad (123)$$

Where L is the 3D plane stress constitutive material tensor, which for a 2D beam is expressed as:

$$L = \left\{ \begin{array}{cc} E & 0 \\ 0 & \dfrac{E}{2(1+v)} \end{array} \right\} \tag{124}$$

Substituting equations (122) and (124) into (123) **K** is expressed as:

$$\mathbf{K} = \int_0^L \int_{-\frac{B}{2}}^{\frac{B}{2}} \int_{-\frac{H}{2}}^{\frac{H}{2}} \left\{ \begin{array}{cccc} \dfrac{36(L-2x)^2 z^2 E}{L^6} & \dfrac{12(2L-3x)(L-2x)z^2 E}{L^5} & -\dfrac{36(L-2x)^2 z^2 E}{L^6} & \dfrac{12(L-3x)(L-2x)z^2 E}{L^5} \\[4mm] \dfrac{12(2L-3x)(L-2x)z^2 E}{L^5} & \dfrac{4(2L-3x)^2 z^2 E}{L^4} & -\dfrac{12(2L-3x)(L-2x)z^2 E}{L^5} & \dfrac{4(L-3x)(2L-3x)z^2 E}{L^4} \\[4mm] -\dfrac{36(L-2x)^2 z^2 E}{L^6} & -\dfrac{12(2L-3x)(L-2x)z^2 E}{L^5} & \dfrac{36(L-2x)^2 z^2 E}{L^6} & -\dfrac{12(L-3x)(L-2x)z^2 E}{L^5} \\[4mm] \dfrac{12(L-3x)(L-2x)z^2 E}{L^5} & \dfrac{4(L-3x)(2L-3x)z^2 E}{L^4} & -\dfrac{12(L-3x)(L-2x)z^2 E}{L^5} & \dfrac{4(L-3x)^2 z^2 E}{L^4} \end{array} \right\} dz\,dy\,dx$$

$$(125)$$

Evaluating the integral in (125) yields the expression for the stiffness matrix:

$$\mathbf{K} = \left\{ \begin{array}{cccc} \dfrac{BH^3 E}{L^3} & \dfrac{BH^3 E}{2L^2} & -\dfrac{BH^3 E}{L^3} & \dfrac{BH^3 E}{2L^2} \\[4mm] \dfrac{BH^3 E}{2L^2} & \dfrac{BH^3 E}{3L} & -\dfrac{BH^3 E}{2L^2} & \dfrac{BH^3 E}{6L} \\[4mm] -\dfrac{BH^3 E}{L^3} & -\dfrac{BH^3 E}{2L^2} & \dfrac{BH^3 E}{L^3} & -\dfrac{BH^3 E}{2L^2} \\[4mm] \dfrac{BH^3 E}{2L^2} & \dfrac{BH^3 E}{6L} & -\dfrac{BH^3 E}{2L^2} & \dfrac{BH^3 E}{3L} \end{array} \right\} \tag{126}$$

Substituting the moment of inertia I for $\dfrac{BH^3}{12}$ the expression in (126) can be written as:

$$\mathbf{K} = \begin{Bmatrix} \dfrac{12\mathrm{E}I}{L^3} & \dfrac{6\mathrm{E}I}{L^2} & -\dfrac{12\mathrm{E}I}{L^3} & \dfrac{6\mathrm{E}I}{L^2} \\[2mm] \dfrac{6\mathrm{E}I}{L^2} & \dfrac{4\mathrm{E}I}{L} & -\dfrac{6\mathrm{E}I}{L^2} & \dfrac{2\mathrm{E}I}{L} \\[2mm] -\dfrac{12\mathrm{E}I}{L^3} & -\dfrac{6\mathrm{E}I}{L^2} & \dfrac{12\mathrm{E}I}{L^3} & -\dfrac{6\mathrm{E}I}{L^2} \\[2mm] \dfrac{6\mathrm{E}I}{L^2} & \dfrac{2\mathrm{E}I}{L} & -\dfrac{6\mathrm{E}I}{L^2} & \dfrac{4\mathrm{E}I}{L} \end{Bmatrix} \tag{127}$$

Equation (127) is identical to the stiffness matrix for a 2D Euler-Bernoulli beam [85].

B.2 Two Node Reddy 2D Beam

The displacement of the Reddy beam as presented in [86] is given as:

$$u = z\left[\psi - \frac{4}{3}\left(\frac{z}{h}\right)^2 \left(\psi + \frac{\partial w}{\partial x}\right) \right] \tag{128}$$

$$w = w_0 \tag{129}$$

Note that with the change of variable $\gamma = \dfrac{\partial w}{\partial x} + \psi$ the displacement field in (128) yields the same results as (61)

Using a 2 node beam with degrees of freedom w^i, $\dfrac{\partial w^i}{\partial x}$ and ψ^i on each node, the matrix form of the discretized displacements is expressed as:

$$\left\{ \begin{array}{c} u \\ v \end{array} \right\} = \mathbf{N} \left\{ w^1 \quad \dfrac{\partial w^1}{\partial x} \quad \psi^1 \quad w^2 \quad \dfrac{\partial w^2}{\partial x} \quad \psi^2 \right\}^T \tag{130}$$

Using the Hermitian interpolation functions for w^i, $\dfrac{\partial w^i}{\partial x}$, linear Lagrange interpolants for ψ^i, and the displacement field in (128) and (129) the full field shape functions are:

$$\mathbf{N} = \left\{ \begin{array}{cc} \dfrac{8(L-x)xz^3}{H^2L^3} & \dfrac{(L-x)^2(L+2x)}{L^3} \\[3ex] \dfrac{4(L-3x)(L-x)z^3}{3H^2L^2} & -\dfrac{(L-x)^2 x}{L^2} \\[3ex] \dfrac{(L-x)z(3H^2-4z^2)}{3H^2L} & 0 \\[3ex] \dfrac{8x(-L+x)z^3}{H^2L^3} & \dfrac{(3L-2x)x^2}{L^3} \\[3ex] \dfrac{4x(-2L+3x)z^3}{3H^2L^2} & \dfrac{(L-x)x^2}{L^2} \\[3ex] \dfrac{xz\left(3-\dfrac{4z^2}{H^2}\right)}{3L} & 0 \end{array} \right\}^T \tag{131}$$

Inserting the expression in (131) into (121) the strain displacement matrix is expressed as:

$$\mathbf{B} = \left\{ \begin{array}{cc} \dfrac{8(L-2x)z^3}{H^2L^3} & -\dfrac{6(L-x)x(H^2-4z^2)}{H^2L^3} \\[3ex] \dfrac{8(-2L+3x)z^3}{3H^2L^2} & -\dfrac{(L-3x)(L-x)(H^2-4z^2)}{H^2L^2} \\[3ex] \dfrac{z\left(-3+\dfrac{4z^2}{H^2}\right)}{3L} & \dfrac{(L-x)(H^2-4z^2)}{H^2L} \\[3ex] -\dfrac{8(L-2x)z^3}{H^2L^3} & \dfrac{6(L-x)x(H^2-4z^2)}{H^2L^3} \\[3ex] -\dfrac{8(L-3x)z^3}{3H^2L^2} & \dfrac{(2L-3x)x(H^2-4z^2)}{H^2L^2} \\[3ex] \dfrac{z\left(3-\dfrac{4z^2}{H^2}\right)}{3L} & \dfrac{x(H^2-4z^2)}{H^2L} \end{array} \right\}^T \tag{132}$$

Substituting equations (132) and (124) into (123) and integrating over the domain, the stiffness matrix **K** is expressed as:

$$\mathbf{K} = \begin{Bmatrix} B\left(\dfrac{H^3\mathrm{E}}{21L^3}+\dfrac{8H\mathrm{E}}{25L(1+\nu)}\right) & B\left(-\dfrac{H^3\mathrm{E}}{42L^2}-\dfrac{2H\mathrm{E}}{75(1+\nu)}\right) & -\dfrac{2BH\mathrm{E}}{15(1+\nu)} & B\left(-\dfrac{H^3\mathrm{E}}{21L^3}-\dfrac{8H\mathrm{E}}{25L(1+\nu)}\right) & B\left(-\dfrac{H^3\mathrm{E}}{42L^2}-\dfrac{2H\mathrm{E}}{75(1+\nu)}\right) & -\dfrac{2BH\mathrm{E}}{15(1+\nu)} \\[2ex]
B\left(-\dfrac{H^3\mathrm{E}}{42L^2}-\dfrac{2H\mathrm{E}}{75(1+\nu)}\right) & B\left(\dfrac{H^3\mathrm{E}}{63L}+\dfrac{8HL\mathrm{E}}{225(1+\nu)}\right) & \dfrac{BH\mathrm{E}\left(4H^2-\dfrac{7L^2}{1+\nu}\right)}{315L} & B\left(\dfrac{H^3\mathrm{E}}{42L^2}+\dfrac{2H\mathrm{E}}{75(1+\nu)}\right) & B\left(\dfrac{H^3\mathrm{E}}{126L}-\dfrac{2HL\mathrm{E}}{225(1+\nu)}\right) & \dfrac{BH\mathrm{E}\left(-4H^2+\dfrac{7L^2}{1+\nu}\right)}{315L} \\[2ex]
-\dfrac{2BH\mathrm{E}}{15(1+\nu)} & \dfrac{BH\mathrm{E}\left(4H^2-\dfrac{7L^2}{1+\nu}\right)}{315L} & B\left(\dfrac{17H^3\mathrm{E}}{315L}+\dfrac{4HL\mathrm{E}}{45(1+\nu)}\right) & \dfrac{2BH\mathrm{E}}{15(1+\nu)} & \dfrac{BH\mathrm{E}\left(-4H^2+\dfrac{7L^2}{1+\nu}\right)}{315L} & B\left(-\dfrac{17H^3\mathrm{E}}{315L}+\dfrac{2HL\mathrm{E}}{45(1+\nu)}\right) \\[2ex]
B\left(-\dfrac{H^3\mathrm{E}}{21L^3}-\dfrac{8H\mathrm{E}}{25L(1+\nu)}\right) & B\left(\dfrac{H^3\mathrm{E}}{42L^2}+\dfrac{2H\mathrm{E}}{75(1+\nu)}\right) & \dfrac{2BH\mathrm{E}}{15(1+\nu)} & B\left(\dfrac{H^3\mathrm{E}}{21L^3}+\dfrac{8H\mathrm{E}}{25L(1+\nu)}\right) & B\left(\dfrac{H^3\mathrm{E}}{42L^2}+\dfrac{2H\mathrm{E}}{75(1+\nu)}\right) & \dfrac{2BH\mathrm{E}}{15(1+\nu)} \\[2ex]
B\left(-\dfrac{H^3\mathrm{E}}{42L^2}-\dfrac{2H\mathrm{E}}{75(1+\nu)}\right) & B\left(\dfrac{H^3\mathrm{E}}{126L}-\dfrac{2HL\mathrm{E}}{225(1+\nu)}\right) & \dfrac{BH\mathrm{E}\left(-4H^2+\dfrac{7L^2}{1+\nu}\right)}{315L} & B\left(\dfrac{H^3\mathrm{E}}{42L^2}+\dfrac{2H\mathrm{E}}{75(1+\nu)}\right) & B\left(\dfrac{H^3\mathrm{E}}{63L}+\dfrac{8HL\mathrm{E}}{225(1+\nu)}\right) & \dfrac{BH\mathrm{E}\left(4H^2-\dfrac{7L^2}{1+\nu}\right)}{315L} \\[2ex]
-\dfrac{2BH\mathrm{E}}{15(1+\nu)} & \dfrac{BH\mathrm{E}\left(-4H^2+\dfrac{7L^2}{1+\nu}\right)}{315L} & B\left(-\dfrac{17H^3\mathrm{E}}{315L}+\dfrac{2HL\mathrm{E}}{45(1+\nu)}\right) & \dfrac{2BH\mathrm{E}}{15(1+\nu)} & \dfrac{BH\mathrm{E}\left(4H^2-\dfrac{7L^2}{1+\nu}\right)}{315L} & B\left(\dfrac{17H^3\mathrm{E}}{315L}+\dfrac{4HL\mathrm{E}}{45(1+\nu)}\right) \end{Bmatrix}$$

(133)

Substituting the moment of inertia I for $\dfrac{BH^3}{12}$, the area A for BH and $G=\dfrac{E}{2(1+\nu)}$ the expressions in (133)can be written as:

$$K = \begin{Bmatrix}
\frac{4EI}{7L^3}+\frac{16GA}{25L} & -\frac{2EI}{7L^2}-\frac{4GA}{75} & -\frac{4GA}{15} & -\frac{4EI}{7L^3}-\frac{16GA}{25L} & -\frac{2EI}{7L^2}-\frac{4GA}{75} & -\frac{4GA}{15} \\[2mm]
-\frac{2EI}{7L^2}-\frac{4GA}{75} & \frac{4EI}{21L}+\frac{16GAL}{225} & \frac{16EI}{105L}-\frac{2GAL}{45} & \frac{2EI}{7L^2}+\frac{4GA}{75} & \frac{2EI}{21L}-\frac{4GAL}{225} & -\frac{16EI}{105L}+\frac{2GAL}{45} \\[2mm]
-\frac{4GA}{15} & \frac{16EI}{105L}-\frac{2GAL}{45} & \frac{68EI}{105L}+\frac{8GAL}{45} & \frac{4GA}{15} & -\frac{16EI}{105L}+\frac{2GAL}{45} & -\frac{68EI}{105L}+\frac{4GAL}{45} \\[2mm]
-\frac{4EI}{7L^3}-\frac{16GA}{25L} & \frac{2EI}{7L^2}+\frac{4GA}{75} & \frac{4GA}{15} & \frac{4EI}{7L^3}+\frac{16GA}{25L} & \frac{2EI}{7L^2}+\frac{4GA}{75} & \frac{4GA}{15} \\[2mm]
-\frac{2EI}{7L^2}-\frac{4GA}{75} & \frac{2EI}{21L}-\frac{4GAL}{225} & -\frac{16EI}{105L}+\frac{2GAL}{45} & \frac{2EI}{7L^2}+\frac{4GA}{75} & \frac{4EI}{21L}+\frac{16GAL}{225} & \frac{16EI}{105L}-\frac{2GAL}{45} \\[2mm]
-\frac{4GA}{15} & -\frac{16EI}{105L}+\frac{2GAL}{45} & -\frac{68EI}{105L}+\frac{4GAL}{45} & \frac{4GA}{15} & \frac{16EI}{105L}-\frac{2GAL}{45} & \frac{68EI}{105L}+\frac{8GAL}{45}
\end{Bmatrix}$$

$$(134)$$

Equation (134) is identical to the stiffness matrix for the 2D Reddy beam [86].

B.3 Three Node Reddy 3D Beam

The displacement for the 3D Reddy beam is given in equations (61) thru (63), the corresponding shape functions are given in (70). The finite element discretization is listed in equation (64).

The strain displacement matrix is obtained by evaluating equation (65) :

$$\mathbf{B} = \left\{
\begin{array}{ccc}
-\dfrac{1}{L} & 0 & 0 \\[2mm]
\dfrac{6(L-2x)\,y}{L^3} & 0 & 0 \\[2mm]
\dfrac{6(L-2x)\,z}{L^3} & 0 & 0 \\[2mm]
0 & \dfrac{z}{L} & -\dfrac{y}{L} \\[2mm]
\dfrac{-4Lz+6xz}{L^2} & 0 & 0 \\[2mm]
\dfrac{4Ly-6xy}{L^2} & 0 & 0 \\[2mm]
\dfrac{(3L-4x)\,z\left(-3H^2+4z^2\right)}{3H^2L^2} & 0 & \dfrac{(L-2x)(L-x)\left(H^2-4z^2\right)}{H^2L^2} \\[2mm]
\dfrac{(3L-4x)\,y\left(-3B^2+4y^2\right)}{3B^2L^2} & \dfrac{(L-2x)(L-x)\left(B^2-4y^2\right)}{B^2L^2} & 0 \\[2mm]
\dfrac{1}{L} & 0 & 0 \\[2mm]
-\dfrac{6(L-2x)\,y}{L^3} & 0 & 0 \\[2mm]
-\dfrac{6(L-2x)\,z}{L^3} & 0 & 0 \\[2mm]
0 & -\dfrac{z}{L} & \dfrac{y}{L} \\[2mm]
-\dfrac{2(L-3x)\,z}{L^2} & 0 & 0 \\[2mm]
\dfrac{2(L-3x)\,y}{L^2} & 0 & 0 \\[2mm]
\dfrac{(L-4x)\,z\left(-3H^2+4z^2\right)}{3H^2L^2} & 0 & 0 \quad -\dfrac{(L-2x)\,x\left(H^2-4z^2\right)}{H^2L^2} \\[2mm]
\dfrac{(L-4x)\,y\left(-3B^2+4y^2\right)}{3B^2L^2} & -\dfrac{(L-2x)\,x\left(B^2-4y^2\right)}{B^2L^2} & 0 \\[2mm]
\dfrac{4(L-2x)\,z\left(3H^2-4z^2\right)}{3H^2L^2} & 0 & \dfrac{4(L-x)\,x\left(H^2-4z^2\right)}{H^2L^2} \\[2mm]
\dfrac{4(L-2x)\,y\left(3B^2-4y^2\right)}{3B^2L^2} & \dfrac{4(L-x)\,x\left(B^2-4y^2\right)}{B^2L^2} & 0
\end{array}
\right\}^{T}$$

(135)

116

The stiffness matrix is obtained by:

$$\int_0^L \int_{-\frac{B}{2}}^{\frac{B}{2}} \int_{-\frac{H}{2}}^{\frac{H}{2}} \mathbf{B}^T . \begin{Bmatrix} E & 0 & 0 \\ 0 & \dfrac{E}{2(1+\nu)} & 0 \\ 0 & 0 & \dfrac{E}{2(1+\nu)} \end{Bmatrix} \mathbf{B} \quad dzdydx \qquad (136)$$

Integrating equation (136) results in the stiffness matrix for the 3D beam described in section 3.2 as follows:

$$\mathbf{K}[1:3] = \left\{ \begin{array}{ccc}
\dfrac{BH\mathrm{E}}{L} & 0 & 0 \\[2mm]
0 & \dfrac{B^3H\mathrm{E}}{L^3} & 0 \\[2mm]
0 & 0 & \dfrac{BH^3\mathrm{E}}{L^3} \\[2mm]
0 & 0 & 0 \\[2mm]
0 & 0 & -\dfrac{BH^3\mathrm{E}}{2L^2} \\[2mm]
0 & \dfrac{B^3H\mathrm{E}}{2L^2} & 0 \\[2mm]
0 & 0 & -\dfrac{4BH^3\mathrm{E}}{15L^2} \\[2mm]
0 & -\dfrac{4B^3H\mathrm{E}}{15L^2} & 0 \\[2mm]
-\dfrac{BH\mathrm{E}}{L} & 0 & 0 \\[2mm]
0 & -\dfrac{B^3H\mathrm{E}}{L^3} & 0 \\[2mm]
0 & 0 & -\dfrac{BH^3\mathrm{E}}{L^3} \\[2mm]
0 & 0 & 0 \\[2mm]
0 & 0 & -\dfrac{BH^3\mathrm{E}}{2L^2} \\[2mm]
0 & \dfrac{B^3H\mathrm{E}}{2L^2} & 0 \\[2mm]
0 & 0 & -\dfrac{4BH^3\mathrm{E}}{15L^2} \\[2mm]
0 & -\dfrac{4B^3H\mathrm{E}}{15L^2} & 0 \\[2mm]
0 & 0 & \dfrac{8BH^3\mathrm{E}}{15L^2} \\[2mm]
0 & \dfrac{8B^3H\mathrm{E}}{15L^2} & 0
\end{array} \right\}^{T} \tag{137}$$

$$
\mathbf{K}[4:6] = \left\{
\begin{array}{ccc}
0 & 0 & 0 \\[6pt]
0 & 0 & \dfrac{B^3 H \mathrm{E}}{2L^2} \\[10pt]
0 & -\dfrac{BH^3 \mathrm{E}}{2L^2} & 0 \\[10pt]
\dfrac{BH\left(B^2+H^2\right)\mathrm{E}}{24L(1+\nu)} & 0 & 0 \\[12pt]
0 & \dfrac{BH^3 \mathrm{E}}{3L} & 0 \\[10pt]
0 & 0 & \dfrac{B^3 H \mathrm{E}}{3L} \\[10pt]
0 & \dfrac{BH^3 \mathrm{E}}{5L} & 0 \\[10pt]
0 & 0 & -\dfrac{B^3 H \mathrm{E}}{5L} \\[10pt]
0 & 0 & 0 \\[6pt]
0 & 0 & -\dfrac{B^3 H \mathrm{E}}{2L^2} \\[10pt]
0 & \dfrac{BH^3 \mathrm{E}}{2L^2} & 0 \\[10pt]
-\dfrac{BH\left(B^2+H^2\right)\mathrm{E}}{24L(1+\nu)} & 0 & 0 \\[12pt]
0 & \dfrac{BH^3 \mathrm{E}}{6L} & 0 \\[10pt]
0 & 0 & \dfrac{B^3 H \mathrm{E}}{6L} \\[10pt]
0 & \dfrac{BH^3 \mathrm{E}}{15L} & 0 \\[10pt]
0 & 0 & -\dfrac{B^3 H \mathrm{E}}{15L} \\[10pt]
0 & -\dfrac{4BH^3 \mathrm{E}}{15L} & 0 \\[10pt]
0 & 0 & \dfrac{4B^3 H \mathrm{E}}{15L}
\end{array}
\right\}^{T}
\qquad (138)
$$

119

$$\mathbf{K}[7:9] = \left\{ \begin{array}{ccc}
0 & 0 & -\dfrac{BH\mathrm{E}}{L} \\[2mm]
0 & -\dfrac{4B^3H\mathrm{E}}{15L^2} & 0 \\[2mm]
-\dfrac{4BH^3\mathrm{E}}{15L^2} & 0 & 0 \\[2mm]
0 & 0 & 0 \\[2mm]
\dfrac{BH^3\mathrm{E}}{5L} & 0 & 0 \\[2mm]
0 & -\dfrac{B^3H\mathrm{E}}{5L} & 0 \\[2mm]
\dfrac{BH\mathrm{E}\left(85H^2+\dfrac{24L^2}{1+\nu}\right)}{675L} & 0 & 0 \\[4mm]
0 & \dfrac{BH\mathrm{E}\left(85B^2+\dfrac{24L^2}{1+\nu}\right)}{675L} & 0 \\[4mm]
0 & 0 & \dfrac{BH\mathrm{E}}{L} \\[2mm]
0 & \dfrac{4B^3H\mathrm{E}}{15L^2} & 0 \\[2mm]
\dfrac{4BH^3\mathrm{E}}{15L^2} & 0 & 0 \\[2mm]
0 & 0 & 0 \\[2mm]
\dfrac{BH^3\mathrm{E}}{15L} & 0 & 0 \\[2mm]
0 & -\dfrac{B^3H\mathrm{E}}{15L} & 0 \\[2mm]
B\left(\dfrac{17H^3\mathrm{E}}{945L}-\dfrac{2HL\mathrm{E}}{225(1+\nu)}\right) & 0 & 0 \\[3mm]
0 & \dfrac{17B^3H\mathrm{E}}{945L}-\dfrac{2BHL\mathrm{E}}{225(1+\nu)} & 0 \\[3mm]
B\left(-\dfrac{136H^3\mathrm{E}}{945L}+\dfrac{4HL\mathrm{E}}{225(1+\nu)}\right) & 0 & 0 \\[3mm]
0 & -\dfrac{136B^3H\mathrm{E}}{945L}+\dfrac{4BHL\mathrm{E}}{225(1+\nu)} & 0
\end{array} \right\}^{T} \tag{139}$$

$$\mathbf{K}[10:12] = \left\{ \begin{array}{ccc}
0 & 0 & 0 \\[6pt]
-\dfrac{B^3 H \mathrm{E}}{L^3} & 0 & 0 \\[10pt]
0 & -\dfrac{B H^3 \mathrm{E}}{L^3} & 0 \\[10pt]
0 & 0 & -\dfrac{B H \left(B^2 + H^2\right)\mathrm{E}}{24 L (1+\nu)} \\[12pt]
0 & \dfrac{B H^3 \mathrm{E}}{2 L^2} & 0 \\[10pt]
-\dfrac{B^3 H \mathrm{E}}{2 L^2} & 0 & 0 \\[10pt]
0 & \dfrac{4 B H^3 \mathrm{E}}{15 L^2} & 0 \\[10pt]
\dfrac{4 B^3 H \mathrm{E}}{15 L^2} & 0 & 0 \\[8pt]
0 & 0 & 0 \\[6pt]
\dfrac{B^3 H \mathrm{E}}{L^3} & 0 & 0 \\[10pt]
0 & \dfrac{B H^3 \mathrm{E}}{L^3} & 0 \\[10pt]
0 & 0 & \dfrac{B H \left(B^2 + H^2\right)\mathrm{E}}{24 L (1+\nu)} \\[12pt]
0 & \dfrac{B H^3 \mathrm{E}}{2 L^2} & 0 \\[10pt]
-\dfrac{B^3 H \mathrm{E}}{2 L^2} & 0 & 0 \\[10pt]
0 & \dfrac{4 B H^3 \mathrm{E}}{15 L^2} & 0 \\[10pt]
\dfrac{4 B^3 H \mathrm{E}}{15 L^2} & 0 & 0 \\[10pt]
0 & -\dfrac{8 B H^3 \mathrm{E}}{15 L^2} & 0 \\[10pt]
-\dfrac{8 B^3 H \mathrm{E}}{15 L^2} & 0 & 0
\end{array} \right\}^{T} \tag{140}$$

$$\mathbf{K}[13:15] = \left\{ \begin{array}{ccc}
0 & 0 & 0 \\[6pt]
0 & \dfrac{B^3 H \mathrm{E}}{2L^2} & 0 \\[10pt]
-\dfrac{BH^3\mathrm{E}}{2L^2} & 0 & -\dfrac{4BH^3\mathrm{E}}{15L^2} \\[10pt]
0 & 0 & 0 \\[6pt]
\dfrac{BH^3\mathrm{E}}{6L} & 0 & \dfrac{BH^3\mathrm{E}}{15L} \\[10pt]
0 & \dfrac{B^3 H\mathrm{E}}{6L} & 0 \\[10pt]
\dfrac{BH^3\mathrm{E}}{15L} & 0 & B\left(\dfrac{17H^3\mathrm{E}}{945L} - \dfrac{2HL\mathrm{E}}{225(1+v)}\right) \\[12pt]
0 & -\dfrac{B^3 H\mathrm{E}}{15L} & 0 \\[10pt]
0 & 0 & 0 \\[6pt]
0 & -\dfrac{B^3 H\mathrm{E}}{2L^2} & 0 \\[10pt]
\dfrac{BH^3\mathrm{E}}{2L^2} & 0 & \dfrac{4BH^3\mathrm{E}}{15L^2} \\[10pt]
0 & 0 & 0 \\[6pt]
\dfrac{BH^3\mathrm{E}}{3L} & 0 & \dfrac{BH^3\mathrm{E}}{5L} \\[10pt]
0 & \dfrac{B^3 H\mathrm{E}}{3L} & 0 \\[10pt]
\dfrac{BH^3\mathrm{E}}{5L} & 0 & \dfrac{BH\mathrm{E}\left(85H^2 + \dfrac{24L^2}{1+v}\right)}{675L} \\[14pt]
0 & -\dfrac{B^3 H\mathrm{E}}{5L} & 0 \\[10pt]
-\dfrac{4BH^3\mathrm{E}}{15L} & 0 & B\left(-\dfrac{136H^3\mathrm{E}}{945L} + \dfrac{4HL\mathrm{E}}{225(1+v)}\right) \\[12pt]
0 & \dfrac{4B^3 H\mathrm{E}}{15L} & 0
\end{array} \right\}^{T} \tag{141}$$

$$\mathbf{K}[16:18] = \left\{\begin{matrix}
0 & 0 & 0 \\[2mm]
-\dfrac{4B^3H\mathrm{E}}{15L^2} & 0 & \dfrac{8B^3H\mathrm{E}}{15L^2} \\[4mm]
0 & \dfrac{8BH^3\mathrm{E}}{15L^2} & 0 \\[4mm]
0 & 0 & 0 \\[2mm]
0 & -\dfrac{4BH^3\mathrm{E}}{15L} & 0 \\[4mm]
-\dfrac{B^3H\mathrm{E}}{15L} & 0 & \dfrac{4B^3H\mathrm{E}}{15L} \\[4mm]
0 & B\left(-\dfrac{136H^3\mathrm{E}}{945L}+\dfrac{4HL\mathrm{E}}{225(1+v)}\right) & 0 \\[4mm]
\dfrac{17B^3H\mathrm{E}}{945L}-\dfrac{2BHL\mathrm{E}}{225(1+v)} & 0 & -\dfrac{136B^3H\mathrm{E}}{945L}+\dfrac{4BHL\mathrm{E}}{225(1+v)} \\[4mm]
0 & 0 & 0 \\[2mm]
\dfrac{4B^3H\mathrm{E}}{15L^2} & 0 & -\dfrac{8B^3H\mathrm{E}}{15L^2} \\[4mm]
0 & -\dfrac{8BH^3\mathrm{E}}{15L^2} & 0 \\[4mm]
0 & 0 & 0 \\[2mm]
0 & -\dfrac{4BH^3\mathrm{E}}{15L} & 0 \\[4mm]
-\dfrac{B^3H\mathrm{E}}{5L} & 0 & \dfrac{4B^3H\mathrm{E}}{15L} \\[4mm]
0 & B\left(-\dfrac{136H^3\mathrm{E}}{945L}+\dfrac{4HL\mathrm{E}}{225(1+v)}\right) & 0 \\[4mm]
\dfrac{BH\mathrm{E}\left(85B^2+\dfrac{24L^2}{1+v}\right)}{675L} & 0 & -\dfrac{136B^3H\mathrm{E}}{945L}+\dfrac{4BHL\mathrm{E}}{225(1+v)} \\[6mm]
0 & \dfrac{16BH\mathrm{E}\left(85H^2+\dfrac{42L^2}{1+v}\right)}{4725L} & 0 \\[6mm]
-\dfrac{136B^3H\mathrm{E}}{945L}+\dfrac{4BHL\mathrm{E}}{225(1+v)} & 0 & \dfrac{16BH\mathrm{E}\left(85B^2+\dfrac{42L^2}{1+v}\right)}{4725L}
\end{matrix}\right\}^{T}$$

(142)

This page intentionally left blank.